



**University of
Zurich**^{UZH}

Mapping Saxaul (*Haloxylon ammodendron*) in the Great Gobi B Strictly Protected Area system using Sentinel-1 and Sentinel-2 data

GEO 511 Master's Thesis

Author

Jan Schweizer
14-715-106

Supervised by

Dr. Christian Rossi (christian.rossi@nationalpark.ch)
Dr. Petra Kaczensky (petra.kaczensky@inn.no)
Dr. Mathias Kneubühler
Marius Rüeetschi (marius.rueetschi@wsl.ch)

Faculty representative

Prof. Dr. Alexander Damm

24.06.2022

Department of Geography, University of Zurich

Abstract

Saxaul (*Haloxylon ammodendron*) is an important component of the ecosystems in the Dzungarian Gobi and provides various ecosystem services including counteracting desertification, habitat provision, and source of food for both livestock and wildlife. However, with the ongoing decrease in spatial extent and density of the saxaul forests in the Mongolian Gobi, exhaustive monitoring of saxaul forests is urgently needed.

Remote sensing data are characterised by repeated observations and high spatial coverage, making them a potential data source for monitoring saxaul forests. In this methodologically exploratory thesis, I attempt to map density and distribution of saxaul forests in the Great Gobi B Strictly Protected Area (GGB SPA) using Sentinel-1 and Sentinel-2 data. Furthermore, the added value of combining optical and SAR data and the importance of variables for mapping saxaul should be determined. The Google Earth Engine (GEE) was used for processing and analysing satellite data over several years for the study area of 18'000 km².

First, several methods were compared to determine the saxaul density near the Khonin us ranger station, including Random Forest regression and linear spectral mixture analysis (LSMA) with algorithm-extracted and RTM-simulated endmembers. Close-range camera images and a high-resolution SkySat-4 image were used for validation. The density estimation was carried out for August 2021. It was attempted to distinguish plant species from each other using the estimated density and additional variables in two oasis complexes, Takhi us and Khonin us. Second, a classification of the dominant vegetation communities in the GGB SPA took place to determine the potential spatial distribution of saxaul forests using a Random Forest classifier. To assess the influence of variable types on model performance, groups of variables were formed from Sentinel-1 and Sentinel-2 bands, various indices, temporal, and textural variables. For training and validation, vegetation plots from a previous mapping were used, which are spatially distributed over large parts of the GGB SPA. The vegetation community mapping was conducted for 2019 and 2020.

The most spatially consistent estimation of saxaul forest density was achieved with LSMA of Sentinel-2 data, for which a combination of algorithm-extracted soil and RTM-simulated vegetation endmembers was used ($R^2 = 0.29$ and 0.25 , $RMSE = 10$ and 4% for two validation plots, respectively). However, the distinction of plant species in two oasis complexes was not possible. The most important variables for mapping the possible spatial distribution of saxaul

forests (PA = 0.74 and UA = 0.64, average values over both years) included elevation and temporal variables, followed by textural and SAR variables. The spatial extent of saxaul forests in the GGB SPA was estimated at 8'141 and 8'323 km² for 2019 and 2020, respectively.

The results show that the density estimation of the saxaul forests in the Dzungarian Gobi is feasible using freely available medium-resolution satellite data and that the possible spatial distribution of saxaul forests in the GGB SPA can be roughly delineated.

Table of Contents

1 Introduction.....	1
2 Materials	5
2.1 Study area.....	5
2.2 Saxaul (<i>Haloxylon ammodendron</i>).....	6
2.3 Software and processing environments.....	8
2.4 Field data and reference map	8
2.5 Remote sensing data.....	12
3 Methods.....	19
3.1 Saxaul density estimation.....	19
3.2 Land cover and vegetation community mapping	31
4 Results.....	35
4.1 Saxaul density estimation.....	35
4.2 Land cover and vegetation community mapping	46
5 Discussion.....	54
5.1 Field data and satellite data	54
5.2 Saxaul density estimation.....	58
5.3 Land cover and vegetation community mapping	65
5.4 Future possibilities	67
6 Conclusion	70
Supplementary materials A.....	72
Supplementary materials B	75
Supplementary materials C.....	76
Supplementary materials D.....	78
Supplementary materials E	80
Supplementary materials F	82
Supplementary materials G.....	83
Acknowledgments.....	86
References.....	87
Personal declaration	105

List of Figures

Figure 1: A relatively large saxaul tree in front of a Great Gobi B Strictly Protected Area ranger.....	7
Figure 2: Spatial distribution of the plots of the forest inventory 2020.....	9
Figure 3: Spatial distribution of the vegetation plots provided by Oyundari Chuluunkhuyag.....	10
Figure 4: Histograms of key attributes of the vegetation plots provided by Oyundari Chuluunkhuyag.....	10
Figure 5: Spatial distribution of the Great Gobi B Strictly Protected Area ranger records....	11
Figure 6: Histogram of tree heights of the Great Gobi B Strictly Protected Area ranger records.....	11
Figure 7: Spatial extent of the reference map by von Wehrden and Gungalag (2003).	12
Figure 8: Pre-processing steps of Sentinel-1 data.....	13
Figure 9: Monthly image availability of Sentinel-1 data.....	14
Figure 10: Sentinel-2A MultiSpectral Instrument spectral response functions.....	15
Figure 11: Pre-processing steps of Sentinel-2 data.....	16
Figure 12: Monthly availability of Sentinel-2 data.....	16
Figure 13: SkySat-4 spectral response functions.....	18
Figure 14: SkySat-4 Normalised Difference Vegetation Index.....	18
Figure 15: Processing workflow of saxaul density estimation.	19
Figure 16: Histograms of key attributes of the vegetation plots provided by Oyundari Chuluunkhuyag containing saxaul trees.	20
Figure 17: Overview of monitoring, training, and validation plots.....	30
Figure 18: Location of Takhi us and Khonin us oases.	31
Figure 19: Processing workflow of land cover and vegetation community mapping.	32
Figure 20: Relationship between vegetation indices and fractional vegetation cover of forest inventory plots.	35
Figure 21: Fractional vegetation cover of forest inventory plots and model estimates.....	35
Figure 22: Usability assessment of Great Gobi B Strictly Protected Area ranger plots.....	36
Figure 23: Linear spectral mixture analysis of the SkySat-4 image.....	37
Figure 24: Saxaul density maps generated with the SkySat-4 image.....	38
Figure 25: RF-RF and RF-LSMA model performances with different training set size.....	40

Figure 26: Estimated saxaul density of machine learning models.....	41
Figure 27: Spectral signatures of simulated endmembers and combined endmember set.	42
Figure 28: Linear spectral mixture analysis of Sentinel-2 image with combined endmember set.	43
Figure 29: Variable importance of all variable combinations for land cover mapping.....	49
Figure 30: Land cover maps of the Great Gobi B Strictly Protected Area.	50
Figure 31: Variable importance of all variable combinations for vegetation community mapping.....	52
Figure 32: Vegetation community maps of the Great Gobi B Strictly Protected Area.	53
Figure 33: Time series of Sentinel-1 backscatter coefficients of saxaul and non-saxaul areas in VV and VH polarisation.	56
Figure 34: Comparison of aggregated SkySat-4 and Sentinel-2 data.	58
Figure 35: Relative proportions of the three simulated endmembers in the total detected saxaul fraction.....	63
Figure 36: Variable importance of Random Forest model of Chuluunkhuyag et al. (2021).....	66
Figure 37: Adapted land cover and vegetation community map of Chuluunkhuyag et al. (2021).....	66
Figure 38: Algorithm-extracted endmember signatures.	77
Figure 39: Correlation matrix of input variables for land cover and community mapping 2019.....	82
Figure 40: Correlation matrix of input variables for land cover and community mapping 2019 after removing selected correlated variables.....	82
Figure 41: RF-RF and RF-LSMA model performances with different training subsets and training set size.....	84

List of Tables

Table 1: Overview of calculated vegetation indices for the usability assessment of field data.....	21
Table 2: Predictor variables of machine learning models used for saxaul density estimation.....	25
Table 3: Overview of PROSPECT-4 parametrisation.	28
Table 4: Classification of the vegetation plots used for land cover and vegetation community mapping.	33
Table 5: Overview of composition and naming of variable combinations for machine learning models.....	39
Table 6: Variables included in R13 and R7 combinations of the RF-RF and RF-LSMA models.....	40
Table 7: Validation results of the compared saxaul density estimates.	44
Table 8: Assignment of vegetation community IDs.	45
Table 9: Confusion matrix of Takhi us 2021.	45
Table 10: Confusion matrix of Khonin us 2021.	46
Table 11: Variable combinations used for the land cover and vegetation community mapping.....	46
Table 12: Accuracy metrics of land cover mapping.	47
Table 13: Accuracy metrics of vegetation community mapping.	51
Table 14: Traits of the simulated endmembers used for saxaul density estimation.	63
Table 15: Determination of s2cloudless threshold.....	73
Table 16: Overview of the performances of Sen2Cor and s2cloudless.	74
Table 17: Parametrisation of the Random Forest model used for forest inventory usability assessment.	75
Table 18: Architecture of the 1-D Convolutional Neural Network model used for forest inventory usability assessment.....	75
Table 19: Confusion matrix of Takhi us 2019.	78
Table 20: Confusion matrix of Takhi us 2020.	78
Table 21: Confusion matrix of Khonin us 2019.	79
Table 22: Confusion matrix of Khonin us 2020.	79
Table 23: Feature importance of all variable combinations for land cover mapping.	80

Table 24: Feature importance of all variable combinations for vegetation community mapping.....	81
Table 25: Presence of spatial autocorrelation in training sets for machine learning models.	83
Table 26: Presence of spatial autocorrelation in the larger validation plot.....	85
Table 27: Validation results of the compared saxaul density estimates with different validation sets.....	85

List of Abbreviations

1D-CNN	One-Dimensional Convolutional Neural Network
ANC	Abundance Nonnegativity Constraint
ANN	Artificial Neural Network
ARD	Analysis-Ready Data
ARTMO	Automated Radiative Transfer Models Operator
ASC	Abundance Sum-to-One Constraint
BOA	Bottom-of-Atmosphere
BRDF	Bidirectional Reflectance Distribution Function
CCD	Coherence Change Detection
CDI	Sentinel-2 Cloud Displacement Index
CEOS	Committee on Earth Observation Satellites
CNN	Convolutional Neural Network
CR	Cross Ratio
DEM	Digital Elevation Model
DVI	Difference Vegetation Index
e.g.	for example (<i>exempli gratia</i>)
ESA	European Space Agency
EVI	Enhanced Vegetation Index
FRDC	Forest Research and Development Center
FVC	Fractional Vegetation Cover
GCP	Google Cloud Platform
GEE	Google Earth Engine
GGB SPA	Great Gobi B Strictly Protected Area
GIS	Geographic Information System
GLCM	Gray Level Co-Occurrence Matrix
GNDVI	Green Normalised Difference Vegetation Index
GPM DPR	Global Precipitation Mission Dual-Frequency Precipitation Radar
GPR	Gaussian Processes Regression
GPS	Global Positioning System
GRD	Ground Range Detected
GRVI	Green Ratio Vegetation Index

i.e.	in other words (<i>id est</i>)
L-7	Landsat-7
L-8	Landsat-8
LHS	Latin Hypercube Sampling
LightGBM	Light Gradient Boosting Machine
LSMA	Linear Spectral Mixture Analysis
MDA	Mean Decrease Accuracy
MDG	Mean Decrease Gini
MESMA	Multiple Endmember Spectral Mixture Analysis
MLRA	Machine Learning Regression Algorithm
MSAVI	Modified Soil Adjusted Vegetation Index
MSI	MultiSpectral Instrument
MVC-NMF	Minimum Volume Constrained Non-Negative Matrix Factorisation
NASA	National Aeronautics and Space Administration
NDII	Normalised Difference 819/1600
NDVI	Normalised Difference Vegetation Index
N-FINDER	N-Finder
NGBDI	Normalised Green-Blue Difference Index
NIR	Near Infrared
NWHFC	Noise-Whitened Harsanyi-Farrand-Chang
PA	Producer's Accuracy
PPI	Pixel Purity Index
R²	Coefficient of Determination
RE	Red Edge
ReNDVI	Red Edge Normalised Difference Vegetation Index
RF	Random Forest
RF-C	Random Forest Classifier
RF-R	Random Forest Regressor
RGRI	Red Green Ratio Index
RLF	Refined Lee Filter
RMSE	Root Mean Square Error
RTM	Radiative Transfer Model
RVI	Ratio Vegetation Index
S-1	Sentinel-1

S-2	Sentinel-2
SAC	Spatial Autocorrelation
SAR	Synthetic Aperture Radar
SCL	Scene Classification Band
Sen2Cor	Sentinel 2 (Atmospheric) Correction
SLC	Single-Look Complex
SRTM	Shuttle Radar Topography Mission
SVM	Support Vector Machine
SWIR	Shortwave Infrared
TCT	Tasseled Cap Transformation
UA	User's Accuracy
VCA	Vertex Component Analysis
VH	Vertical Transmit, Horizontal Receive
VI	Vegetation Index
VV	Vertical Transmit, Vertical Receive

1 Introduction

Motivation

Saxaul (*Haloxylon ammodendron*) is an important component of the ecosystems in the Dzungarian Gobi and one of the dominant woody plant species in Asian deserts (Huang et al., 2003), where it is sometimes the only forest component (Enkhchimeg et al., 2020). The saxaul trees provide a wide range of ecosystem services, such as slowing down wind speed and fixating sand, counteracting soil erosion and desertification (Huang et al., 2003; Khaulenbek et al., 2018). The trees provide a habitat for insect species and facilitate the settlement of other plants (Batchuluun et al., 2020; Enkhchimeg et al., 2020). Saxaul is an important source of food for both livestock and wildlife, e.g., the focal species Khulan (*Equus hemionus*) (Burnik Šturm et al., 2017). Furthermore, the local human population uses saxaul forests to extract firewood (Khaulenbek et al., 2018).

Biodiversity is often difficult to restore in arid ecosystems once degradation has occurred (Zheng and Wang, 2014). Therefore, monitoring changes in ecosystems is important to assess their general condition (Lee et al., 2021). Mapping of saxaul forests and its changes can help to understand the state of the Mongolian Gobi and the effects of climatic and anthropogenic pressures on the ecosystem (Kazantseva et al., 2012). Suvdantsetseg et al. (2008) reported a 50% decrease in saxaul forest extent in the Mongolian Gobi between 1969 and 1994. Khaulenbek et al. (2018) observed a trend from dense to sparse forest since the 1970s. In light of these developments, several calls for further research have been made.

For some time now, there has been the suggestion to monitor saxaul more closely, especially in protected areas (von Wehrden et al., 2009). Khaulenbek et al. (2018) criticised that basic research on the spatial distribution of saxaul is still insufficient. Correspondingly, saxaul forests are a research priority of the Great Gobi B Strictly Protected Area (GGB SPA) as a key habitat (Ganbaatar et al., 2019).

Previous work

Remote sensing data are characterised by repeated observations and high spatial coverage and are therefore ideally suited for mapping large areas (Joshi et al., 2016). Hence, remote sensing can be a potential data source for mapping saxaul forests (Batsaikhan et al., 2020). Many of the medium-resolution satellite data are freely available. Sentinel-1 (S-1) and Sentinel-2 (S-2),

1 Introduction

part of the European Space Agency's (ESA) Copernicus program, provide synthetic aperture radar (SAR) and optical data with up to 10 m resolution and revisit times of up to 5 days (Aschbacher, 2017; Gascon et al., 2017; Torres et al., 2012). The combination of spectral, spatial, and temporal information allows for a detailed investigation of the spectral reflectance properties and texture of the earth's surface, as well as the phenology of plants (Cheng and Wang, 2019).

In the past, satellite remote sensing data were used for several mappings covering the Dzungarian Gobi. A vegetation map for the former extent of the GGB SPA using Landsat-7 (L-7) data was prepared almost 20 years ago, showing the distribution of saxaul (von Wehrden and Gungalag, 2003). From today's perspective, the map is no longer particularly up-to-date, and in 2019 the area of the GGB SPA was doubled (Ganbaatar et al., 2019). The global forest cover change map based on Landsat-8 (L-8) data by Hansen et al. (2013) has attracted a lot of attention from the remote sensing community. However, the product is limited to forest areas with a minimum height of 5 m and a minimum density of 25% canopy closure per pixel (Hansen et al., 2010) - requirements that sparse saxaul forests do not often meet. Heiner et al. (2015) created a freely accessible web-based geographic information system (GIS) for the Mongolian Gobi by combining various data sources. It provides information on biogeographic regions, ecosystem types, and landforms with a resolution of about 80 m. In particular, one ecosystem type explicitly refers to saxauls, but isolating single saxaul communities is impossible from the dataset. Nyamsuren et al. (2019) used space-born Global Precipitation Mission dual-frequency precipitation radar (GPM DPR) data for vegetation monitoring in Mongolia. However, the spatial resolution of 5 km is too low to provide information about saxaul forests on a local scale. The ESA WorldCover product provides a global land cover classification based on S-1 and S-2 data (Zanaga et al., 2021). Despite remarkable preciseness for certain areas, the vast majority of the Dzungarian Gobi is classified as barren or sparsely vegetated. Recently, Chuluunkhuyag et al. (2021) published a classification of the Dzungarian Gobi based on the dominant vegetation communities. However, the classification is based on L-8 data from 2015, and saxaul cannot be isolated as a separate species. Meng et al. (2021) used Landsat time series to quantify desertification processes in Mongolia for the period from 1990 to 2020. However, no explicit conclusions can be drawn about the distribution of saxaul. Despite these numerous approaches, there is still a lack of an up-to-date and explicit saxaul mapping that covers the entire current area of the GGB SPA with moderate spatial resolution.

1 Introduction

Also, it remains unclear to date which methods are most appropriate for S-1 and S-2 data to address this open issue and what is the added value of combining optical and SAR data.

Aims and objectives

The purpose of this thesis is to explore the potential of combining S-1 and S-2 data for mapping saxaul from 2019 to 2021 with a specific focus on applying different remote sensing approaches. The thesis is divided into two parts. First, it is to be investigated which methods are most suitable to estimate the density of saxaul on the pixel level. Due to data availability, the saxaul density estimation is carried out for August 2021. Second, I repeated the mapping of vegetation communities by Chuluunkhuyag et al. (2021) with S-1 and S-2 data with a higher spatial resolution to assess the importance of individual predictor variables and the added value resulting from the inclusion of additional variable types and SAR data. This mapping is carried out with the data of 2019 and 2020.

The methodological focus lies on machine learning classification and regression as well as linear spectral mixture analysis (LSMA). The Google Earth Engine (GEE) allows for large-scale and fast processing of remote sensing data and provides access to complete archives of various sensors without the need for downloading (Amani et al., 2019; Gorelick et al., 2017) and is frequently used for vegetation mapping applications (Campos-Taberner et al., 2018; Jin et al., 2019).

Research questions

Two main challenges in mapping saxaul were identified. First, the saxaul trees mostly grow in sparse communities, therefore, the target is often smaller than the resolution of the satellite data. Second, distinguishing between different shrub species is difficult, especially if no extensive field data is available. For me, this results in two research questions:

- 1) How can the saxaul density be estimated most accurately on the pixel level?
- 2) How accurately can the vegetation community distribution be mapped using moderate-resolution satellite remote sensing data?

To answer the first research question, a test area near the Khonin us ranger station is investigated. This spatial limitation is due to the availability of field data. The mapping of vegetation communities takes place for the whole area of the GGB SPA.

1 Introduction

Outline

This thesis is structured as follows: in materials, the study area and the saxaul are introduced in more detail followed by an overview of the available data and their respective pre-processing. In methods, the saxaul density estimation and the vegetation community mapping are explained step by step. In results, the outcomes of the analyses are presented. The discussion consists of four parts, focusing on data issues, the two practical parts, and future possibilities for improving saxaul mapping approaches. The conclusion summarises the most important findings.

2 Materials

2.1 Study area

Dzungarian Gobi

The Dzungarian Gobi is a semi-desert basin located in south-western Mongolia and lies at an altitude of 1'100 to 3'400 m.a.s.l. (Shukherdorj et al., 2021). Strong seasonal variations in temperature and precipitation characterise the temperate continental climate (Kaczensky et al., 2008). The average temperature is -0.5°C with minimum and maximum temperatures of -40 and 40°C and annual precipitation is approximately 100 mm/a (ibid.). The climatic conditions are strongly influenced by the basin's topography (Chuluunkhuyag et al., 2021). The lack of screening mountains towards precipitation from the West represents unique topographical conditions in Southern Mongolia and leads, for example, to a relatively large amount of snow in winter (von Wehrden et al., 2006).

Biodiversity in both plant and animal species is high due to a topographically determined multitude of land cover types, including wetlands, saline sites, steppes, and meadows (Chuluunkhuyag et al., 2021; Shukherdorj et al., 2021). The Dzungarian Gobi represents a specific phytogeographical region of Mongolia (Shukherdorj et al., 2021) and is home to a unique composition of species (von Wehrden et al., 2006). A longitudinal gradient dominates plant species distribution in altitude (Chuluunkhuyag et al., 2021) with low local heterogeneity of most vegetation types (von Wehrden et al., 2006). At lower elevation, vegetation is mainly limited to drainage lines and other water-storing areas, such as sand dunes (von Wehrden et al., 2009), since surface waters are rare (Kaczensky et al., 2011). Common ungulate species include black-tailed gazelles (*Gazella subgutturosa*), Asiatic wild ass (*Equus hemionus*), argali (*Ovis ammon*) and ibex (*Capra sibirica*). The large predator community consists of grey wolves (*Canis lupus*) which are common and lynx (*Lynx lynx*) and snow leopard (*Uncia uncia*) which are much rarer (Kaczensky et al., 2008).

Great Gobi B Strictly Protected Area

The GGB SPA, founded in 1975 to conserve the Dzungarian Gobi ecosystem and ensure its sustainable development, covers about 18'000 km² (Ganbaatar et al., 2019). It is also known for a successful reintroduction project of Przewalski horses (*Equus ferus przewalskii*) that started in the 1990s (Kaczensky et al., 2017).

Despite its protection status, the GGB SPA is not uninhabited. Local herder families and their livestock use the protected area primarily in winter and during spring and fall migration, and border patrol personnel is stationed at three stations along the Chinese-Mongolian border (Michler et al., 2022).

Regional ecosystem threats

Arid ecosystems are vulnerable and their restoration is complex, often leading to a decrease in biodiversity once disturbance has occurred (Zheng and Wang, 2014). Human and non-human factors threaten Mongolian drylands, such as road construction, mining, the absence of long-term land management planning, the lack of financial resources for reforestation, and the grazing pressure of an increasing livestock population (Khaulenbek et al., 2018).

In the GGB SPA, illegal mining, poaching, and the illegal use of woody plants like saxaul for heating are threatening the fragile ecosystem (Ganbaatar et al., 2019). In addition, the combined grazing by wild animals and rapidly increasing livestock can negatively impact the sparse vegetation, although grazing pressure is not as severe in the GGB SPA as in other protected areas in Southern Mongolia (Michler et al., 2022).

2.2 Saxaul (*Haloxylon ammodendron*)

Distribution

Saxaul belongs to the dominant plants in Asian deserts at an altitude between 1'030 and 1'710 m.a.s.l. (Huang et al., 2003; Shukherdorj et al., 2021). Saxaul trees are the largest carbon stock in Southern Mongolia and Central Asia (Batsaikhan et al., 2020). In Mongolia, the area covered by saxaul forests is estimated at approximately 20'000 km² (FAO, 2020, 2014; Government of Mongolia, 2018). However, there is no unique definition of the term *saxaul forest*. On the one hand, it can be defined as an area of at least 1 ha with trees higher than 1 m and with a total canopy cover of at least 4% (FAO, 2020). On the other hand, it is common practice to consider all sparse communities of saxaul trees as *forests* (Khaulenbek et al., 2018).

Several studies have documented changes in saxaul distribution over the past decades. Since the 1970s, a large-scale increase in sparse and a decrease in dense saxaul forests has been observed (Khaulenbek et al., 2018). Other researchers reported a decrease in saxaul forest extent of 50% between 1969 and 1994 (Suvdantsetseg et al., 2008). It is assumed that the

2 Materials

combined effects of climate change and human impact are the main drivers of these developments (Kazantseva et al., 2012).



Figure 1: A relatively large saxaul tree in front of a Great Gobi B Strictly Protected Area ranger. Image credits: Great Gobi B Strictly Protected Area rangers.

Physiology and resistance

Saxaul trees are stem-succulent shrubs (Nyongesah et al., 2015) with a typical height of 40-70 cm (Chuluunkhuyag et al., 2021). Tree heights above 2 m are rare (von Wehrden et al., 2009). The leaves are usually degenerated, and photosynthesis occurs in young twigs, so-called assimilating branches (Nyongesah et al., 2015). Correspondingly, the chlorophyll concentration in saxaul branches is low compared to other species (Li and Wang, 2013). The phenology, e.g., the moment of green-up, is in close relationship with the amount of precipitation (Ganbaatar, 2021, personal communication).

Most of the water demand of saxaul trees is met by accessing the near-groundwater layer (Wu et al., 2019). Subsequently, groundwater availability is closely associated with saxaul distribution and height (Batsaikhan et al., 2020; von Wehrden et al., 2006). Saxaul trees favour coarse-textured soils with a high fraction of sand, as they allow for the growth of deep root systems up to 10 m improving access to groundwater (Zou et al., 2010).

In the Dzungarian Gobi and elsewhere, saxaul trees grow and survive under harsh conditions including droughts and saline soils (Khaulenbek et al., 2018; Wu et al., 2019). Even during long-lasting droughts or after high precipitation events, the photosynthetic activity of saxaul remains relatively stable through morphological adjustment (Xu and Li, 2006). The processes of morphological adjustment allow the plant to react to changes in water availability by shoot

defoliation or root system adjustment (Zou et al., 2010). Additionally, saxaul is a xero-halophyte, which means the plant can resist high salinity (Huang et al., 2003). Adapting to high salinity includes salt avoidance, tolerance, and evasion (Ramadan, 1998).

2.3 Software and processing environments

In this thesis, the GEE JavaScript API (<https://code.earthengine.google.com/>) was used for the (pre-)processing and analysis of large amounts of satellite data. QGIS 3.20.3 Odense (QGIS Development Team, 2021) was used for smaller image analysis and visualisation tasks. Most of the machine and deep learning model optimisation and data visualisation tasks were done locally in a Python environment. The most important packages included the following: Scikit-learn 0.22.2 (Pedregosa et al., 2011) for machine learning, Keras API 2.4.3 (Chollet, 2015) running on top of TensorFlow 2.3.0 (TensorFlow Developers, 2022) for deep learning, and Rasterio 1.2.10 (Gillies, 2019), GeoPandas 0.10.2 (Jordahl et al., 2014), and seaborn 0.11.2 (Waskom, 2021) for visualisation. I used MATLAB 2021a (MathWorks, 2021) for the extraction of endmembers and running the Automated Radiative Transfer Models Operator (ARTMO) toolbox (Verrelst et al., 2012) to simulate vegetation spectra. ArcGIS Pro 2.8.3 (ESRI Inc., 2021) was used to determine spatial autocorrelation (SAC).

2.4 Field data and reference map

2.4.1 Forest inventory 2020

Three different institutions conducted forest inventories on behalf of the Forest Research and Development Center (FRDC) for the Altai, Bulgan, and Üyench sums of the Khovd aimag in 2020 (Khatant Forest LLC, 2020; Munkh Nagoon Joodoo LLC, 2020; Zaluu Tugul LLC, 2020). The non-public database contains the location, height, crown area, and species information of trees recorded in groups of four circular sampling plots with a radius of 14.5 m each 50 m apart (Figure 2).

The total number of trees, the number of saxaul trees, and the total crown area for each plot inside the GGB SPA boundaries were calculated. Only trees not lacking necessary properties for these calculations, e.g., plot assignment, species, and crown radius information, were considered. The resulting dataset consists of 47'220 trees and 5'924 plots. Over 95% of the trees are labeled as saxaul and over 90% of the plots only contain saxaul trees.

2 Materials

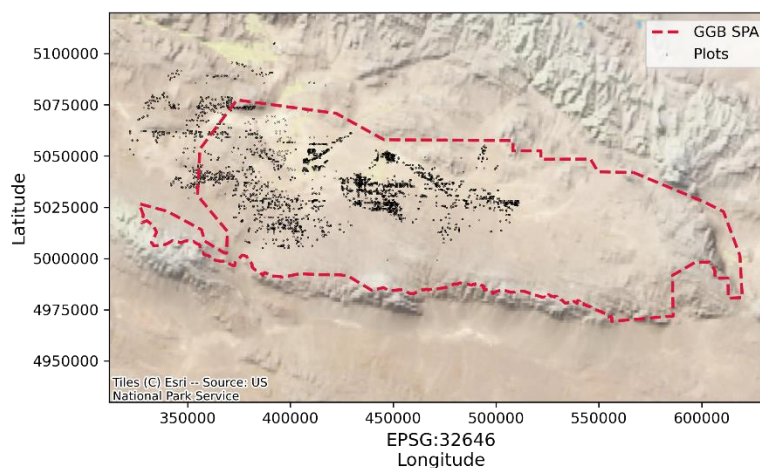


Figure 2: Spatial distribution of the plots of the forest inventory 2020. The locations of the plots in the Altai, Bulgan, and Üyenich sums of the Khovd aimag, Dzungarian Gobi, are indicated by black dots. The dashed red line represents the boundaries of the Great Gobi B Strictly Protected Area.

2.4.2 Vegetation plots across the Dzungarian Gobi

Chuluunkhuyag et al. (2021) used a collection of plots located in the GGB SPA and the northern surroundings to create a landcover and vegetation community map of the Dzungarian Gobi (Figure 3). Oyundari Chuluunkhuyag provided access to the plot collection.

The collection consists of 644 plots of a size of 10 x 10 m. For each plot, information about land cover, dominant vegetation community, species richness, and fractional vegetation cover (FVC) is available. 151 plots contain saxaul trees, of which 6 plots are exclusively populated by saxaul.

Figure 4 provides an overview of some of the plot's key attributes. Most plots are only sparsely vegetated. Usually, the vegetation is not homogeneous but consists of several plant species. Most plots are located at an altitude between 1'000 and 2'000 m.a.s.l. and in a steppe or desert environment.

2 Materials

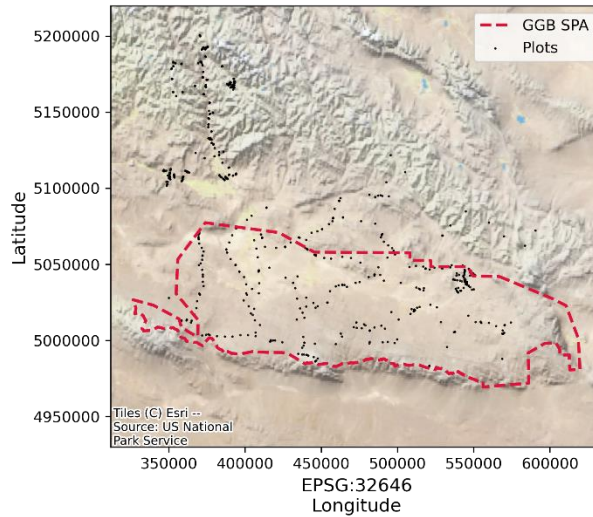


Figure 3: Spatial distribution of the vegetation plots provided by Oyundari Chuluunkhuyag. The black dots represent the 644 plots. The dashed red line represents the boundaries of the Great Gobi B Strictly Protected Area.

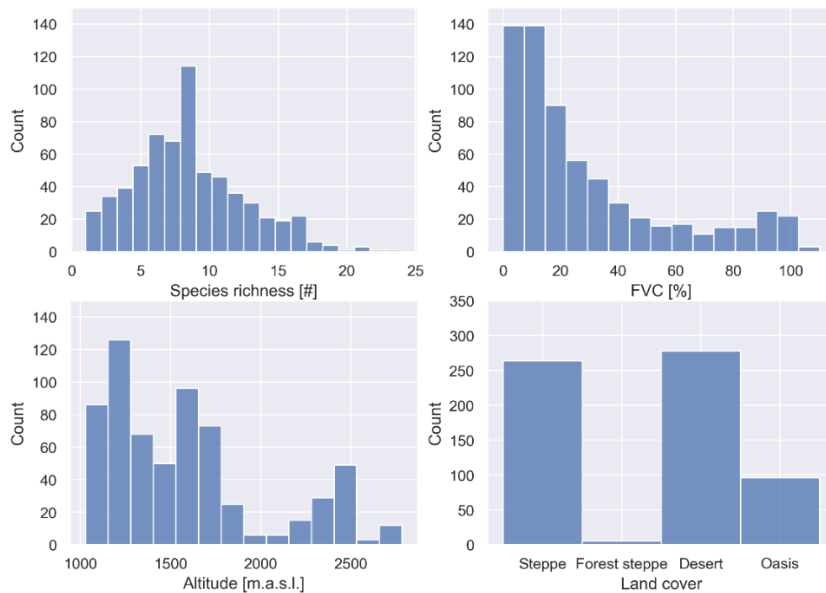


Figure 4: Histograms of key attributes of the vegetation plots provided by Oyundari Chuluunkhuyag. For most plots, the vegetation consists of several species and the fractional vegetation cover is lower than 50%. Most plots are located at an altitude between 1'000 and 2'000 m.a.s.l. and in a steppe or desert environment.

2.4.3 Monitoring plot near Khonin us ranger station

In consultation with co-supervisor Petra Kaczensky, a monitoring plot of a size of 5 x 5 km² was set up within the GGB SPA, close to the Khonin us ranger station. In a field survey taking place from June 24th to July 1st. 2021, GGB SPA rangers recorded all vegetation exceeding 20 cm in height along pre-defined transects with a width of 1 m to the left and right (Figure 5). For each record, the rangers determined plant species and height and used Garmin GPSMAP and/or eTrex Global Positioning System (GPS) devices to assign coordinates. Pictures were taken regularly with Xiaomi Redmi Note 8 and Samsung Galaxy A10s phones.

2 Materials

The results of the field survey consist of 10'327 records and 314 pictures. Of all entries, only 29 were assigned to a species other than saxaul, of which 28 were tamarisk (*Tamarix ramosissima*) and 1 was salsola (exact species not known). The vegetation is usually smaller than 1 m (Figure 6).

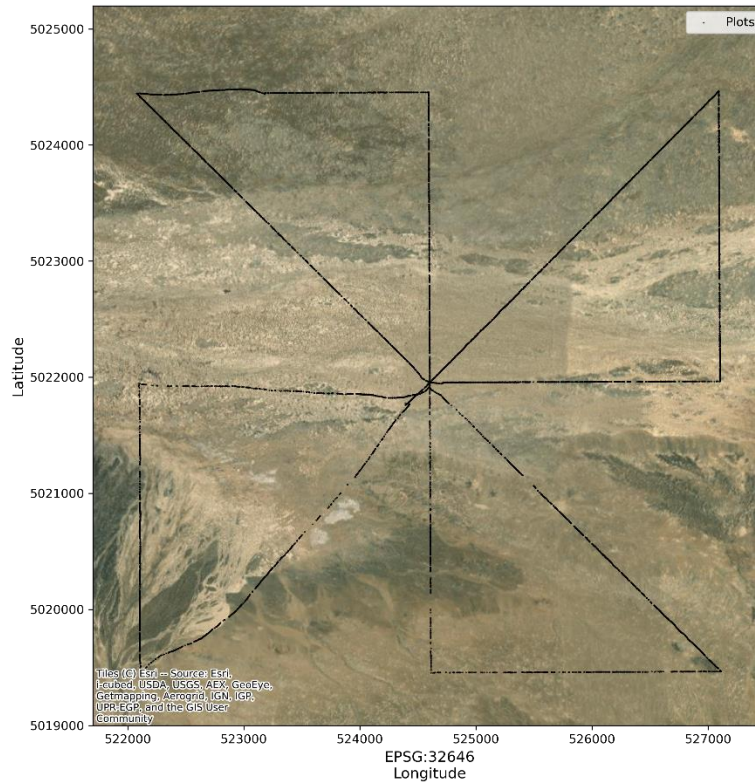


Figure 5: Spatial distribution of the Great Gobi B Strictly Protected Area ranger records. The black dots represent the locations of shrub vegetation recorded in a field survey along pre-defined transects with a width of 1 m to the left and right in the eastern part of the Great Gobi B Strictly Protected Area.

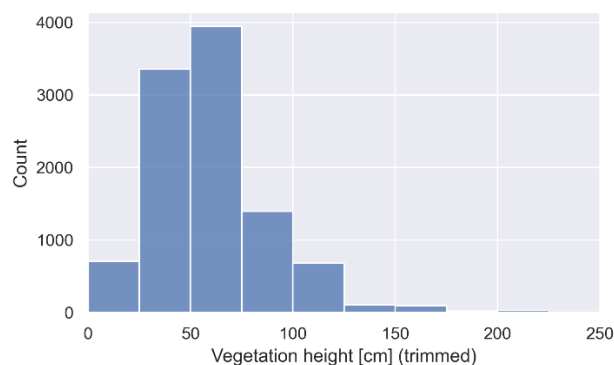


Figure 6: Histogram of tree heights of the Great Gobi B Strictly Protected Area ranger records. Most shrubs recorded in a field survey are smaller than 1m. Outliers with a height of more than 250 cm are not shown.

2.4.4 Phytosociological vegetation map

Von Wehrden and Gungalag (2003) classified the extent of the GGB SPA (before the 2019 expansion) according to a phytosociological system. They have used numerous vegetation plots

2 Materials

and L-7 data to train a maximum likelihood algorithm. The georeferenced data with a spatial resolution of approximately 15 m was available (Figure 7).

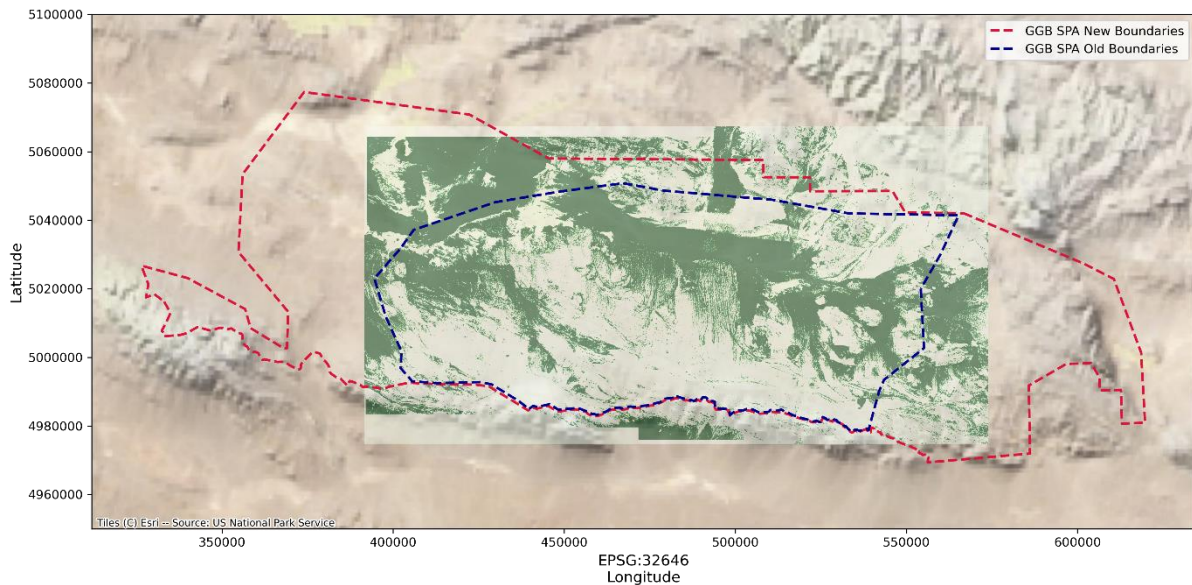


Figure 7: Spatial extent of the reference map by von Wehrden and Gungalag (2003). The old and new boundaries of the Great Gobi B Strictly Protected Area are included for orientation. Saxaul forests according to the reference map are shown in dark green color.

2.5 Remote sensing data

2.5.1 Sentinel-1

Data characteristics

The Copernicus Sentinel-1 (S-1) mission consists of two identical polar-orbiting satellites carrying Synthetic Aperture Radar (SAR) sensors launched in 2014 and 2016, respectively (Potin et al., 2019). The sensors operate at 5.405 GHz, providing VV/VH dual-polarisation imagery with a revisit time of six days and a pixel spacing of 10 m (Rüetschi et al., 2021; Torres et al., 2012). SAR sensors are active systems that emit radiation for illumination, which makes them independent from solar illumination (Filipponi, 2019). The ability of the emitted radiation to penetrate through clouds heavily reduces the effect of weather conditions on data availability (ibid.). The signal recorded by the sensor is the result of the interaction between the emitted signal and the target on the ground, providing information about its backscattering properties (Mandal et al., 2020). Vegetation backscatter is mainly caused by volume scattering (Vreugdenhil et al., 2018). S-1 data are frequently used for vegetation applications, including forest research (Soudani et al., 2021; Weber et al., 2020), biomass estimation (Periasamy,

2018), crop growth monitoring (Mandal et al., 2020), and land cover mapping (Carrasco et al., 2019).

Pre-processing

Several pre-processing steps are required to obtain an S-1 Analysis Ready Data (ARD) product from the S-1 Ground Range Detected (GRD) product (Truckenbrodt et al., 2019) (Figure 8). A framework implemented in the GEE allows the user to select the data of interest and define both the pre-processing steps to be included and the parameter values to be used (Mullissa et al., 2021).

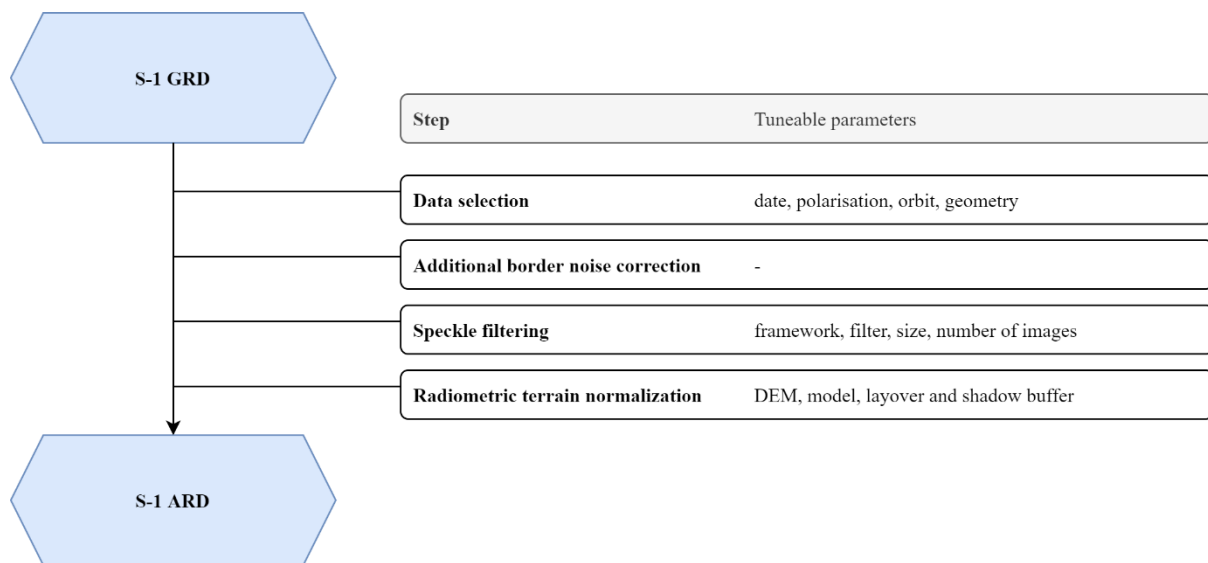


Figure 8: Pre-processing steps of Sentinel-1 data. Blue boxes represent data, and white boxes represent steps and list the tuneable parameters of each step.

For the study period from April to October 2019 and 2020, I selected all S-1 GRD images that overlap the GGB SPA for each month individually. Figure 9 shows the number of available images. Due to the observation scenario, parts of the GGB SPA are almost never covered by images acquired from an ascending orbit. Therefore, only images acquired from a descending orbit were used to ensure consistency in the data and exhaustive spatial coverage.

2 Materials

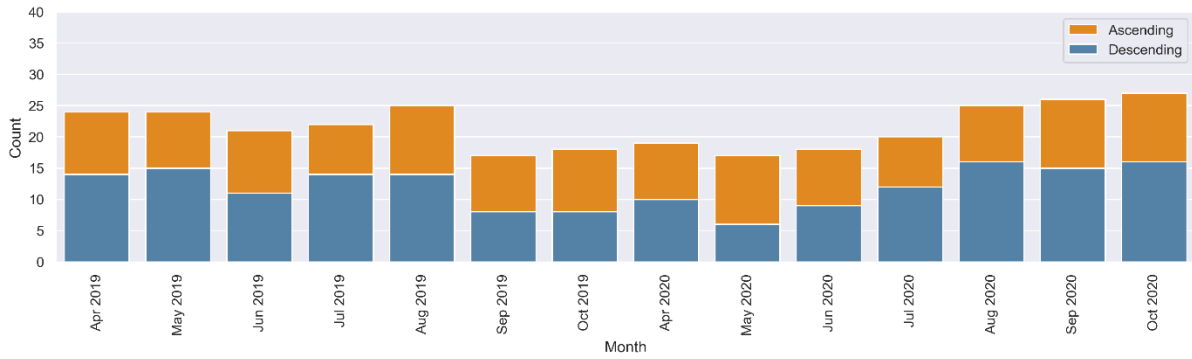


Figure 9: Monthly image availability of Sentinel-1 data. All images overlapping the Great Gobi B Strictly Protected Area during the period from April to October 2019 and 2020 were aggregated per month. The colors refer to the orbit from which the images were taken.

Not all artefacts in the images get fully corrected by the border noise correction which is applied by default to all images acquired after March 2018 (Mullissa et al., 2021). Hence, the additional border noise correction of the GEE framework was applied.

Speckle filtering is a standard pre-processing step, as speckle occurs in all SAR images (Mullissa et al., 2021). The choice of an adequate filter is crucial, otherwise, structures and details in the images can be lost (Chierchia et al., 2017). I used a 15-image multi-temporal 7 x 7 Refined Lee Filter (RLF) (Lee, 1999), as multi-temporal speckle filtering is recommended (Quegan and Yu, 2001) and the type and/or size of the applied filter were also used in previous studies (Carrasco et al., 2019; Yommy et al., 2015; You and Dong, 2020).

Terrain flattening is used to reduce the influence of terrain on the quality of the signal (Loew and Mauser, 2007). The present framework applies an angular-based slope correction (Vollrath et al., 2020) because the use of the terrain-flattened gamma nought (γ^0) backscatter (Small, 2011) is not possible in the GEE. For the radiometric terrain normalisation, I used the volume terrain flattening model and the National Aeronautics and Space Administration (NASA) Shuttle Radar Topography Mission (SRTM) digital elevation model (DEM) with a spatial resolution of 30 m (Farr et al., 2007).

2.5.2 Sentinel-2

Data characteristics

The Copernicus Sentinel-2 (S-2) mission consists of two identical satellites carrying multispectral optical sensors (MultiSpectral Instrument, MSI) launched in 2015 and 2017 (Claverie et al., 2018). The S-2 mission provides imagery with a spatial resolution between 10 and 60 m and a revisit time of five days ranging from the ultra-blue to the short-wave infrared part of the electromagnetic spectrum (ibid.) (Figure 10). In contrast to active SAR sensors,

2 Materials

optical sensors are passive systems (Lillesand et al., 2015). In other words, the signal recorded by the sensor is the result of the interaction of incident solar radiation with particles in the earth's atmosphere on the downwelling path, partial reflectance at the surface, and subsequent interaction with the atmosphere on the upwelling path (Richter and Schläpfer, 2017). Two implications follow from the dependence on solar radiation: first, imaging is possible during the day only, and second, data availability might be limited due to cloud cover. The 10:30 AM overpass time at the descending node of the S-2 satellites is a compromise between high solar altitude and low cloud cover (ESA, 2015).

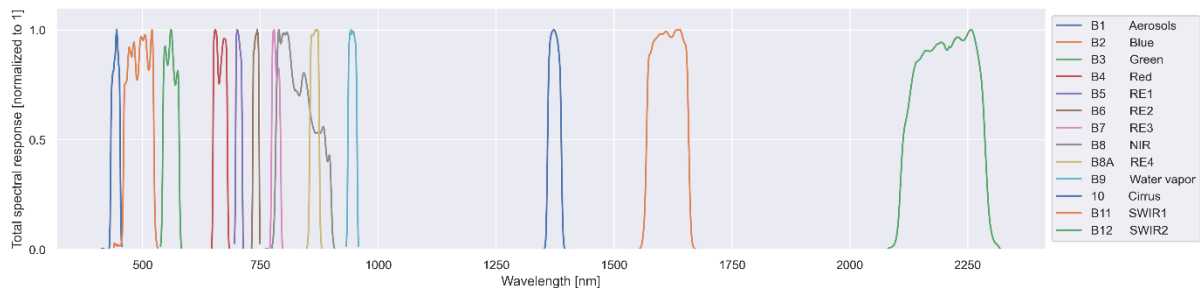


Figure 10: Sentinel-2A MultiSpectral Instrument spectral response functions. The twelve bands are in the range between 400 and 2'500 nm. The colors are for visualisation purposes only and are not related to the human perception of color.

Pre-processing

I used the S-2 MSI Level-2A data available in the GEE. The Level-2A data was generated from Level-1C using the Sentinel 2 (atmospheric) Correction (Sen2Cor) algorithm, which performs an atmospheric and topographic correction and produces a scene classification band (SCL) (Louis et al., 2016; Müller-Wilm, 2017). The further pre-processing included the steps shown in Figure 11.

2 Materials

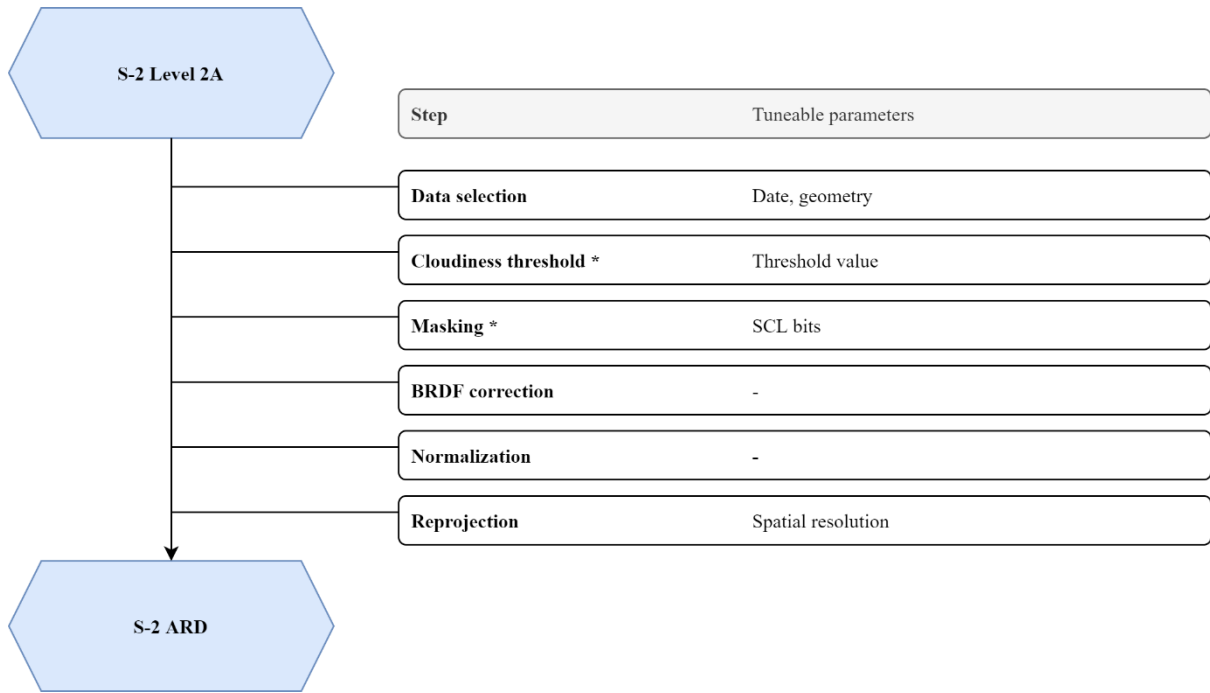


Figure 11: Pre-processing steps of Sentinel-2 data. Blue boxes represent data, and white boxes represent steps and list the tuneable parameters of each step. Steps marked with * were not applied to all data products.

All images overlapping the GGB SPA during the study period were selected. The first two steps after the data selection, cloudiness threshold and masking, were not applied in all workflows to avoid data gaps. Whether the two steps were applied is declared in each case when the data is used. The monthly data availability including the mean cloudy pixel percentage is shown in Figure 12.



Figure 12: Monthly availability of Sentinel-2 data. All images overlapping the Great Gobi B Strictly Protected Area during the period from April to October 2019 and 2020 were aggregated per month. The orange line represents the mean cloud cover of all images per month.

Cloud removal is one of the most basic pre-processing steps for optical remote sensing data (Mateo-García et al., 2018). Accordingly, there are several approaches. Available methods for S-2 data include a recent version of Fmask, Sen2Cor, s2cloudless, and the Sentinel-2 Cloud Displacement Index (CDI) (Frantz et al., 2018; Sanchez et al., 2020). These methods differ in complexity and use of ancillary data. I compared the performances of the Sen2Cor and

2 Materials

s2cloudless approaches to determine a robust cloud correction algorithm for our study area that does not require additional ancillary data and has a reasonable level of complexity. Based on our comparison, I chose Sen2Cor because the performance was better for the dominant type of cloud cover. Further details about the comparison of Sen2Cor and s2cloudless in Supplementary Materials A.

For some data products, I discarded images with a very high cloudy pixel percentage (>90%) by applying a cloudiness threshold. In the masking step, individual image pixels were discarded using the SCL bit mask. Only vegetation, bare soil, and water were kept.

The Bidirectional Reflectance Distribution Function (BRDF) correction is used to eliminate the effects of the viewing geometry on the measured reflectance (Franch et al., 2019). By applying the BRDF correction, the view angle is set to nadir and the solar zenith angle to the respective latitude of the image (Claverie et al., 2018). Poortinga et al. (2019) implemented the BRDF correction in the GEE.

Subsequently, the possible range of values was restricted to the physically meaningful inclusive interval of 0 to 1 (Schaepman-Strub et al., 2006) and all bands were resampled to a spatial resolution of 10 m using the GEE default nearest-neighbor interpolation.

2.5.3 SkySat-4

A high-resolution optical image taken by the SkySat-4 satellite covering the extent of the monitoring plot near the Khonin us ranger station was available. The image was taken on August 10th, 2021 at 11:21 local time (UTC+7) and delivered orthorectified, radiometrically calibrated, and atmospherically corrected to bottom-of-atmosphere (BOA) reflectance (Planet Labs Inc., 2018a). SkySat-4 images contain four bands in the visible and near-infrared spectrum (Planet Labs Inc., 2018b) (Figure 13). The image is composed of three strips with overlapping scenes. Spectral differences between the individual scenes hinder the comparability of different image regions (Figure 14).

2 Materials

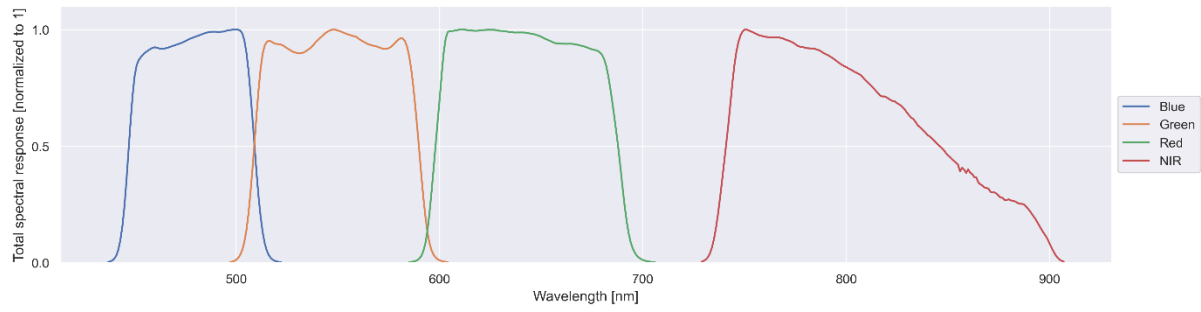


Figure 13: SkySat-4 spectral response functions. The four bands are in the range between 400 and 1'000 nm. The colors are for visualisation purposes only and are not related to the human perception of color.

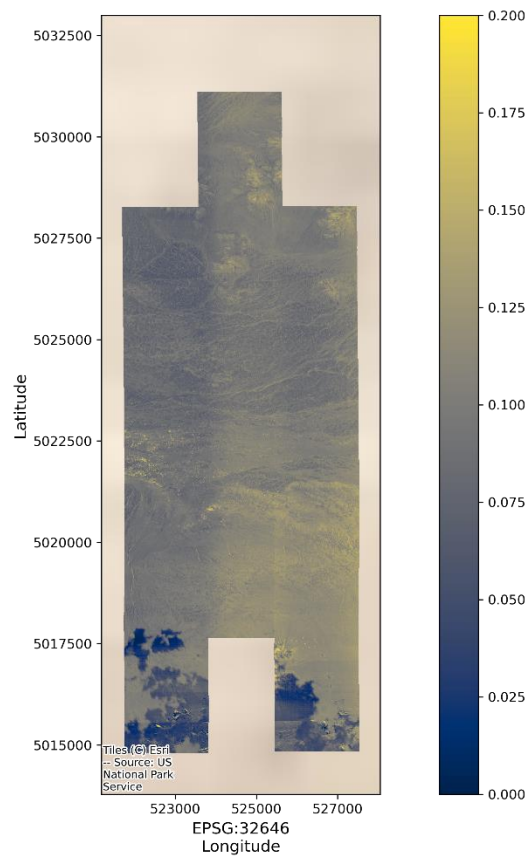


Figure 14: SkySat-4 Normalised Difference Vegetation Index. The value range is trimmed to highlight the systematic differences between the three vertical strips. Visible cloud cover in the south.

3 Methods

3.1 Saxaul density estimation

The focus of the first practical part of the thesis was on the estimation of saxaul density on the pixel level and was spatially limited to a test area near the Khonin us ranger station. The applied methods could be divided into two groups (Figure 15). The methods of the first group relied on saxaul density determined with field data and the SkySat-4 image to serve as training inputs for machine learning models. Subsequently, these models were used to predict saxaul density with S-2 data. The methods of the second group estimated the saxaul density directly from the S-2 data.

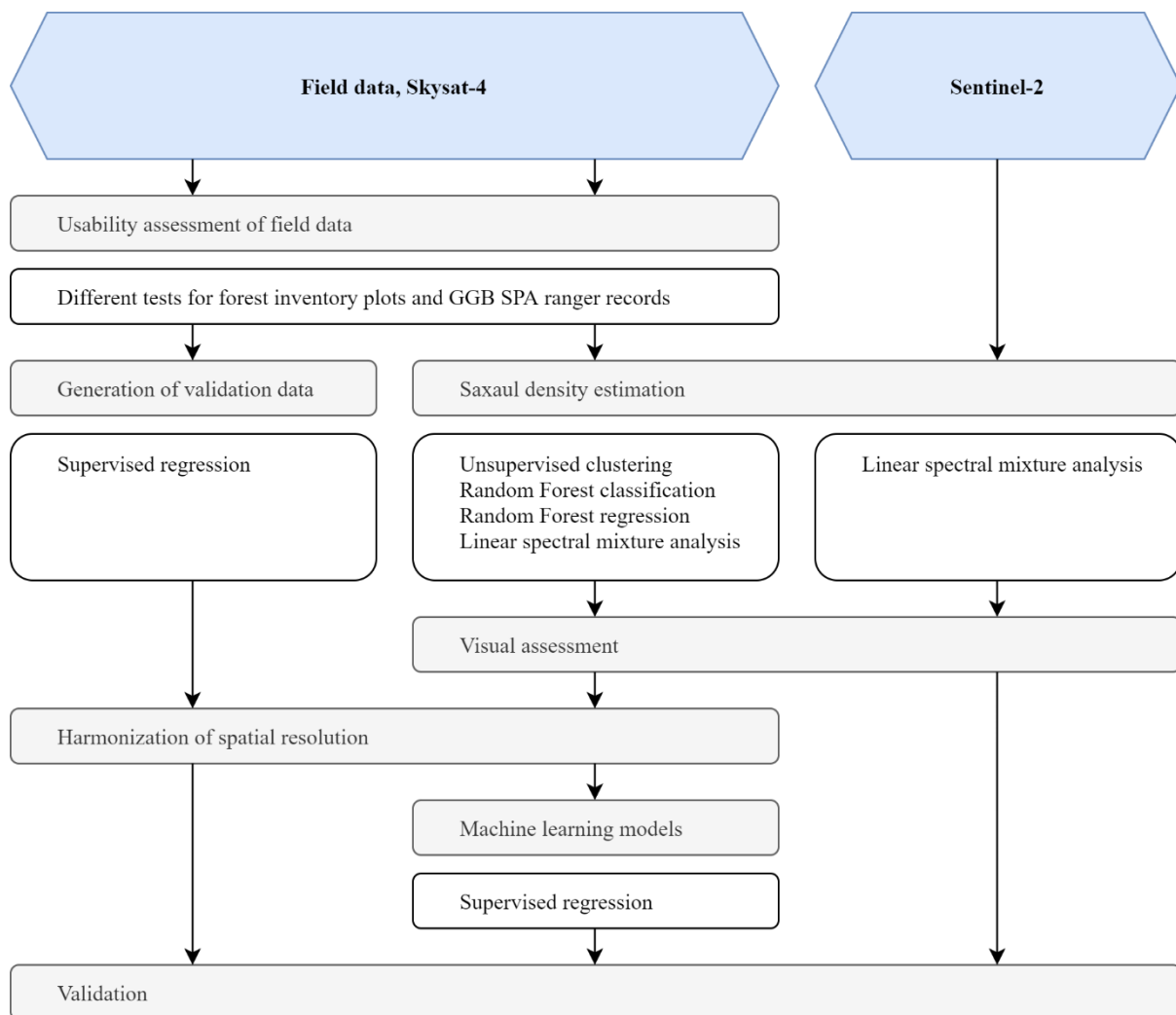


Figure 15: Processing workflow of saxaul density estimation. Blue boxes represent data, and grey boxes represent steps with optional comments in white boxes.

3.1.1 Machine learning models

Usability assessment of field data

I assessed the usability of the forest inventory 2020 and the records by the GGB SPA rangers for serving as input labels for machine learning models. The vegetation plots provided by Oyundari Chuluunkhuyag were not considered because saxaul trees are only present in 151 of the 644 plots and only six of the plots are exclusively covered by saxaul. The mean FVC is about 4.5%, with most values being lower (Figure 16). Therefore, I considered the prospects of obtaining a robust model with this small number of plots to be too low.

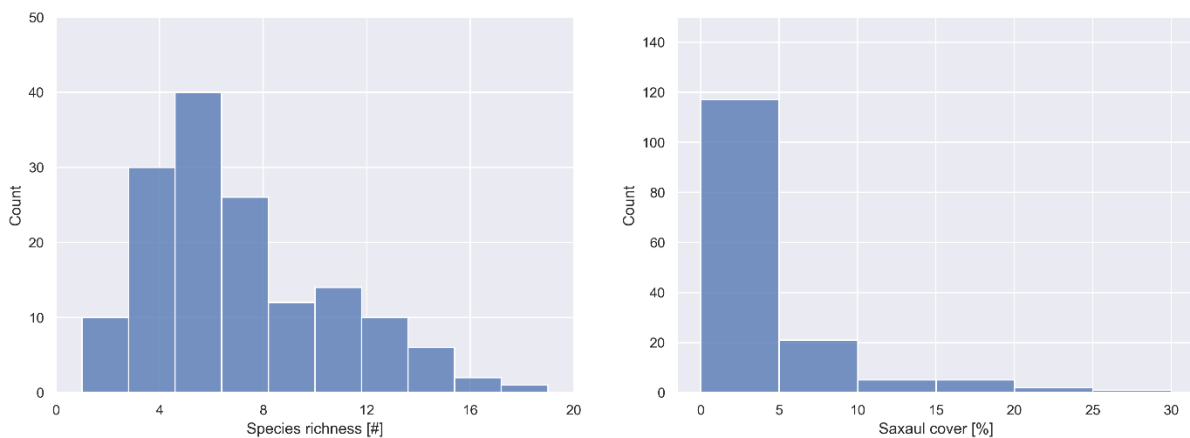


Figure 16: Histograms of key attributes of the vegetation plots provided by Oyundari Chuluunkhuyag containing saxaul trees. Few plots contain only saxaul trees and the area of the plots covered by saxaul trees is usually less than 5%.

Forest inventory 2020

The usability of the forest inventory for this thesis was assessed in two ways. On the one hand, a relationship between FVC expressed through the crown cover of each plot and vegetation indices (VIs), such as the Normalised Difference Vegetation Index (NDVI), should be present. Tang et al. (2020) have shown a positive correlation between FVC and NDVI in desert ecosystems. On the other hand, the dataset could be split into training and testing sets to determine the predictability of FVC based on spectral information.

Regarding the relationship between FVC and VIs, I calculated the S-2 yearly median composite for 2020. Cloudiness threshold and masking were not applied to avoid data gaps. Several VIs (Table 1) were added to the S-2 spectral bands (B2-B8A, B11-B12). A circular area with a radius of 14.5 m was sampled for each of the 5'924 plot centers.

3 Methods

Table 1: Overview of calculated vegetation indices for the usability assessment of field data. These indices can all be calculated with bands of the visual spectrum and a near infrared band.

Index	Formula	Source
NDVI	$\frac{NIR-Red}{NIR+Red}$	Zafari et al. (2019)
MSAVI	$\frac{2 * NIR + 1 - \sqrt{(2 * NIR + 1)^2 - 8 * (NIR - Red)}}{2}$	Zafari et al. (2019)
EVI	$2.5 * \frac{NIR - Red}{NIR + 6 * Red - 7.5 * Blue + 1}$	Zafari et al. (2019)
NGBDI	$\frac{Green-Blue}{Green+Blue}$	Hunt et al. (2005)
RGRI	$\frac{Red}{Green}$	Verrelst et al. (2008)
DVI	$NIR - Red$	Xue and Su (2017)

Two regression models were used to test for the predictability of FVC. The first model was a Random Forest regressor (RF-R). A Random Forest consists of decision trees that are built from randomly selected variables (Breiman, 2001). The final output of a RF-R is the average of the outputs of the decision trees (Pedregosa et al., 2011). The second model was a one-dimensional convolutional neural network (1D-CNN) that uses convolution operations to detect features in the input data (LeCun and Bengio, 1995). This type of CNN has already been proven effective in biophysical variable retrieval (Annala et al., 2020; Pullanagari et al., 2021). The parameter settings and model architectures are listed in Supplementary Materials B. The dataset was randomly split into 80% training and 20% testing data. Both models were trained with the same training data and predicted the same testing data. FVC and the S-2 spectral bands served as input labels and features, respectively. For each model, I calculated the coefficient of determination (R^2) and the root mean square error (RMSE).

An existing positive correlation between FVC and VIs and a certain degree of predictability of FVC were set as conditions for further use of the data.

3 Methods

GGB SPA ranger records

The usability assessment of the GPS locations of the GGB SPA ranger records was based on the assumptions that the VI values of the SkySat-4 pixels at the records' locations indicated a higher presence of vegetation compared to random points. I expected a left-skewed distribution of the sampled VI values in the case of the records' locations and a normal distribution in the case of random points.

First, I extracted all pixel values of the ranger records and random pixels ($n = 10'327$) in the high-resolution SkySat-4 image. Second, the records' point density was calculated for each S-2 image cell overlapping the transects. These cells ($n = 4'817$) were sampled in both the SkySat-4 and the S-2 image of August 12th, 2021 (optional pre-processing steps applied), which has the greatest temporal proximity to the SkySat-4 image. For this, the spatial resolution of the SkySat-4 image was reduced to 10 m by calculating the zonal mean per S-2 grid cell. I calculated the same VIs as for the forest inventory 2020 for all extracted spectra.

A noticeable difference in the distributions of the ranger records' locations and random locations and/or an at least moderate relationship between aggregated point density and index value of the (aggregated) overlapping S-2 cells were set as conditions for further use of the data.

Generation of training data

As previously outlined, the first group of methods to estimate saxaul density relied on training data for machine learning models. The results of the usability assessment showed that the forest inventory 2020 and the locations of the ranger records were not suitable for this purpose (cf. chapter 4.1.1). Therefore, I used the close-range camera pictures of the GGB SPA ranger for the generation of training data. They allowed the detection of vegetation in the SkySat-4 image because its spatial resolution of 50 cm is high enough to visually link features in the close-range camera pictures with the satellite image.

A subset of the SkySat-4 image in the northwest of the monitoring plot was selected as a training area, where the saxaul trees were visually distinguishable from the background. At this point, I equated saxaul with vegetation since the ranger records consist almost entirely of saxaul trees. I used four methods to generate different saxaul density maps for the training area.

Unsupervised clustering

Unsupervised clustering and classification methods do not require labeled training data because they work exclusively with the pixel values of the input image (Lillesand et al., 2015). Thus, the image is first decomposed into different clusters or classes. Only afterward, the individual *informational utility* (ibid.) of the clusters or classes is determined.

I used the K-means clustering algorithm implemented in the GEE (Arthur and Vassilvitskii, 2007) to decompose the training area into 20 clusters. The algorithm calculated the class centroids from 5'000 randomly sampled pixels before classifying the remaining image pixels. Subsequently, I manually classified the output classes as vegetated or not vegetated, generating a binary mask.

Random Forest classification and regression

In the case of the Random Forest methods, classes of interest are defined a priori. The classifier or regressor learns the relationship between input and class using training data associated with each class (Lillesand et al., 2015).

I used a Random Forest model with 500 trees for both output modes, classification (RF-C) and regression (RF-R). All other parameters were set to default (for detailed information see: <https://developers.google.com/earth-engine/apidocs/ee-classifier-smilerandomforest>). I defined three classes: vegetation, bright soil, and gravel. For these classes, training polygons were created, 50 each for vegetation and bright soil and 10 for gravel. The training sets were created from the mean spectra of these polygons. In classification mode, the training sets were used unchanged for the training, i.e., the pixels were classified as vegetation, bright soil, or gravel. In regression mode, vegetation was coded as 1 and the other classes as 0 to approximate FVC. Input properties in both modes were the SkySat-4 spectral bands and the previously used VIs.

Linear spectral mixture analysis

Linear spectral mixture analysis (LSMA) is one of the most widely used methods to determine the sub-pixel fraction of image components, so-called endmembers (Somers et al., 2011). In theory, the image should be explainable by the linear combination of the selected endmembers. In other words, the fractions of the respective pure endmembers summed always add up to 1 (Lillesand et al., 2015). This assumption is not satisfied in many cases, but it can be enforced with a constraint (Small, 2001). Conversely, if not set, the proportion of pixels whose fraction

3 Methods

sums close to 1 can be an indicator of whether this assumption was satisfied (Raksuntorn and Du, 2010). An additional constraint can ensure that the proportions are nonnegative (Nascimento and Dias, 2005). Following Ji et al. (2005), the constraints are hereafter referred to as the abundance sum-to-one constraint (ASC) and abundance nonnegativity constraint (ANC). To obtain a unique solution to the inversion, the number of endmembers must be smaller than the number of spectral bands (Somers et al., 2011). Consequently, the maximum number of endmembers in the SkySat-4 image is three.

I defined the endmembers according to the previously used classes: vegetation, bright soil, and gravel. The most extreme pixels should be selected to generate the purest possible endmember spectra from the SkySat-4 image. I selected three pixels per endmember at our subjective discretion, of which the mean value was calculated in each case.

I used the unmixing function implemented in the GEE and applied it twice, once with and once without active ASC. The ANC was active in both cases.

Evaluation and reduction of spatial resolution

The saxaul density maps were visually assessed by comparing them with the close-range camera pictures and the SkySat-4 image. I reduced the spatial resolution of the two most suitable maps to 10 m by calculating the zonal mean per S-2 grid cell to harmonise the spatial resolution of the density maps and the S-2 data.

Determination of predictor variables

The saxaul density maps created with RF-R and LSMA were found to be the most suitable for further use (cf. chapter 4.1.3). After reducing the spatial resolution, the maps could be used to create training labels for machine learning models. Our goal was to train Random Forest regression models with S-1 and S-2 data to predict saxaul density outside the training area and without further use of the commercial SkySat-4 image.

For a well-performing model, the appropriate predictor variables must be defined. I trained two Random Forest regression models, one for each selected saxaul density map, with various combinations of predictor variables. I checked for the respective feature importance of the variables and assessed the effect of a reduced number of variables on the model performance, as the reduction of data dimensionality can minimise the processing load and lead to more accurate results (Chen et al., 2020).

3 Methods

I created two Random Forest regressor models with 500 trees, all other parameters were set to default. The labels were taken from the saxaul density maps, I called the models RF-RF and RF-LSMA. Table 2 provides an overview of all used variables.

Table 2: Predictor variables of machine learning models used for saxaul density estimation. All variables were calculated from the bands of Sentinel-1 and Sentinel-2. The temporal variables corresponded to the standard deviation of the time series of various indices. The textural variables were derived from the blue band.

Variable group	Elements
S-1 bands	VV, VH
S-1 indices	Cross ratio (CR)
S-2 bands	Blue, Green, Red, RE1, RE2, RE3, NIR, RE4, SWIR1, SWIR2
S-2 indices	NDVI, MSAVI, EVI, NGBDI, RGRI, DVI, RVI, ReNDVI, GRVI, GNDVI, NDII, Brightness, Greenness, Wetness
Temporal variables	NDVI Std., MSAVI Std., Brightness Std., Greenness Std., Wetness Std.
Textural variables	Angular Second Moment, Contrast, Correlation, Dissimilarity, Entropy, Inverse Difference Moment, Sum Average, Variance

S-1 bands and indices

I used the VV and VH bands of the S-1 image from August 14th, 2021, because it has the closest temporal proximity to the SkySat-4 image. In addition, I calculated the cross ratio (CR), which is often used in vegetation studies with SAR data (Soudani et al., 2021; Vreugdenhil et al., 2018).

S-2 bands and indices

I used the spectral bands of the S-2 image of August 12th, 2021, calculated different VIs from the spectral bands, and applied the Tasseled Cap Transformation (TCT). The TCT performs a transformation of the input bands into three vegetation components: brightness, greenness, and wetness being indicative of soil reflectance, green vegetation, and canopy and soil moisture (Lillesand et al., 2015). I used the 6-band TCT coefficients calculated for S-2 Level-1C (Shi and Xu, 2019).

3 Methods

Temporal variables

Vegetation phenology describes the recurring temporal development of leaf characteristics (Gao et al., 2021; Morisette et al., 2009) and can be derived from VIs (Soudani et al., 2021). I assumed that the VI values for vegetation change more over the year than for soil and calculated the standard deviation of the monthly composites for several VIs and the TCT variables for 2021 to quantify this temporal change.

Textural variables

Remote sensing data contains a lot of contextual information (Moser et al., 2013). The gray level co-occurrence matrix (GLCM) metrics are based on the spatial patterns between pixel values in a specific image band (Haralick et al., 1973). I calculated several of these metrics using a 7 x 7 window and the yearly median of the blue band (optional pre-processing steps not applied) (Huang et al., 2017; Pandit et al., 2020; Verde et al., 2020).

With these variables, I formed different combinations and tested different train/test splits. I started with the S-2 spectral bands, which were augmented by further groups of variables until all variables were used. The mean decrease in impurity (also called mean decrease Gini, MDG) was used as a measure of feature importance to reduce the number of variables. The size of the variable combination including the S-2 spectral bands and the S-1 variables serves as benchmark (13 variables). This number was halved again to check for further improvement. The train/test splits were 50/50 and 80/20. For each combination, a 3-fold random subsampling was performed to mitigate the influence of the training sample selection on model performance (Berrar, 2018). Averaged R^2 and RMSE were calculated for each combination and split. The most suitable combination of variables and the most suitable split per model (RF-RF and RF-LSMA) were determined based on the model performance and the number of features required. Subsequently, the two models were used to predict saxaul density for the spatial extent of the SkySat-4 image.

3.1.2 Linear spectral mixture analysis of Sentinel-2 data

The methods of the second group were all LSMA applications with different endmember sets. The endmembers were exclusively algorithm-extracted or simulated, i.e., not defined via the SkySat-4 image or field data. I used the S-2 image from August 12, 2021 (optional pre-processing steps applied) for all LSMA applications.

Algorithm-extracted endmember sets

I applied four endmember extraction methods that generate endmember signatures from the image data: the pixel purity index (PPI), N-finder (N-FINDR), vertex component analysis (VCA), and minimum volume constrained non-negative matrix factorisation (MVC-NMF).

The number of endmembers to be extracted (the only user-defined input parameter) was determined a priori using the noise-whitened Harsanyi-Farrand-Chang (NWHFC) method (Chang and Du, 2004).

I used the four endmember sets as inputs for the unmixing function implemented in the GEE and applied it twice, once with and once without active ASC. The ANC was active in both cases.

Combination of algorithm-extracted and simulated endmembers

I considered the probability of saxaul being identified as an endmember in the S-2 image by the applied extraction methods to be low. Therefore, I created an additional endmember set in which simulated vegetation spectra were integrated.

Radiative transfer models (RTM) are a common tool to simulate vegetation reflectance (Lu et al., 2021). PROSPECT-4 is a simple RTM for simulating directional reflectance and transmittance from 400 to 2'500 nm that requires only four parameters: a leaf structure parameter (N), equivalent water thickness (C_w), dry matter content (C_m), and chlorophyll content (C_{ab}) (Verrelst et al., 2016).

I set N according to the literature (Pyankov et al., 1999; Su et al., 2005) and calculated the remaining parameters based on records in the TRY Plant Trait Database (www.try-db.org). The mean values of three available entries for leaf water content per leaf dry mass (Sheremetev, unpublished) and leaf area per leaf dry mass (with petiole excluded) (Wang et al., 2017) were used for C_w and C_m , respectively. C_{ab} was already included in the database (Sheremetev, unpublished). To ensure some variability in the simulated reflectance, value ranges were defined for each parameter (Table 3).

3 Methods

Table 3: Overview of PROSPECT-4 parametrisation. The reference values for the simulation of saxaul spectra correspond to values from the literature or were calculated from entries in the TRY Plant Trait Database. The applied value ranges correspond to the minimum and maximum possible values of the parameters for the simulations.

Parameter	Reference value	Applied value range	Unit
N	3	2 - 4	-
C_w	0.066	0.055 - 0.075	$\text{cm}^3 \text{cm}^{-2}$
C_m	0.0235	0.0015 - 0.0035	g cm^{-2}
C_{ab}	15.4	10 - 20	$\mu\text{g cm}^{-2}$

A subset of five combinations was simulated, which was determined by Latin hypercube sampling (LHS) to cover most of the multidimensional input space (Verrelst et al., 2017). LHS is a frequently applied technique to reduce the number of RTM simulations (de Sá et al., 2021; Verrelst et al., 2019). The values used for the simulations were drawn from uniform distributions.

LSMA with only the simulated vegetation spectra is not possible, since the condition that all pixels can be represented by a linear combination of the endmembers is not fulfilled. Hence, I integrated MVC-NMF-derived endmembers to represent the soil background. I chose MVC-NMF because of the four applied algorithms it is the only one that does not assume pure spectra to be present in the image.

As previously mentioned, the number of endmembers must be smaller than the number of bands. In the present case, the ten S-2 spectral bands allowed for nine endmembers. I removed three of the nine MVC-NMF-derived endmembers because they seemed untypical for soil. Subsequently, I added three randomly selected simulated endmembers.

I scaled the spectra of the endmembers as well as the S-2 image pixels, as systematic differences between extracted and simulated endmember were to be expected. Each spectrum was divided by the total energy in the spectrum to convert it to a unit vector with length = 1 (Randolph, 2006).

Again, I used the endmember set as input for the unmixing function implemented in the GEE and applied it twice, once with and once without active ASC. The ANC was active in both cases. I summed up the resulting fractions of the saxaul and soil endmembers to get the total fractions of saxaul and soil per pixel.

3.1.3 Validation

Two validation plots were created within the footprint of the SkySat-4 image: the larger one in the south of the training area, the smaller one about 5 km southeast (Figure 17). Their different positions should allow for investigating the influence of the spatial proximity between the training and validation area.

As mentioned in chapter 2.5.3, the comparison of different SkySat-4 image regions is difficult due to the visible spectral differences between the image scenes. Therefore, I estimated saxaul density individually for both validation plots. I trained a Random Forest regressor with 500 trees (all other parameters were set to default) with 20 vegetated and 20 non-vegetated point samples, which were selected by using the close-range camera images and visual interpretation of the SkySat-4 image. Subsequently, the spatial resolution of the density estimates was reduced in the manner previously outlined.

The saxaul density estimates of the following methods were validated: the two Random Forest regressor models (cf. chapter 3.1.1) and the unmixed saxaul fraction of the S-2 image with the set of algorithm-extracted and simulated endmembers (cf. chapter 3.1.2). For the comparison of model performances, I sampled all pixels of the validation plots in the respective density maps and calculated R^2 and RMSE.

3 Methods

median composites. The optional pre-processing steps were not applied to avoid data gaps that make clustering impossible, since a single missing value in the time series causes a missing output. The spectra were scaled as described in chapter 3.1.2. Only the pixels for which the estimated FVC was > 0 were considered any further. Second, MSAVI was calculated for each monthly median composite from April-October. Third, the yearly maximum, mean, and standard deviation were calculated for MSAVI.

A separate clustering model was created for each of the two oasis complexes. The number of output classes corresponded to the number of distinct vegetation communities present in the oasis complexes according to von Wehrden and Gungalag (2003) (8 and 10 for Takhi us and Khonin us, respectively). For both Takhi us and Khonin us, the algorithm calculated the class centroids from 5'000 randomly sampled pixels separately before classifying the remaining image pixels of each region.

For each of the six comparisons (two areas and three years), a confusion matrix was calculated based on a stratified sample with 1000 samples for each vegetation community present in the oasis complex. I defined a best-fit indicator since it was unclear which cluster belonged to which vegetation class. The best-fit indicator corresponds to the maximum percent of pixels in a cluster that belongs to the same class and therefore provides information on how closely a pixel cluster belongs to a vegetation class.

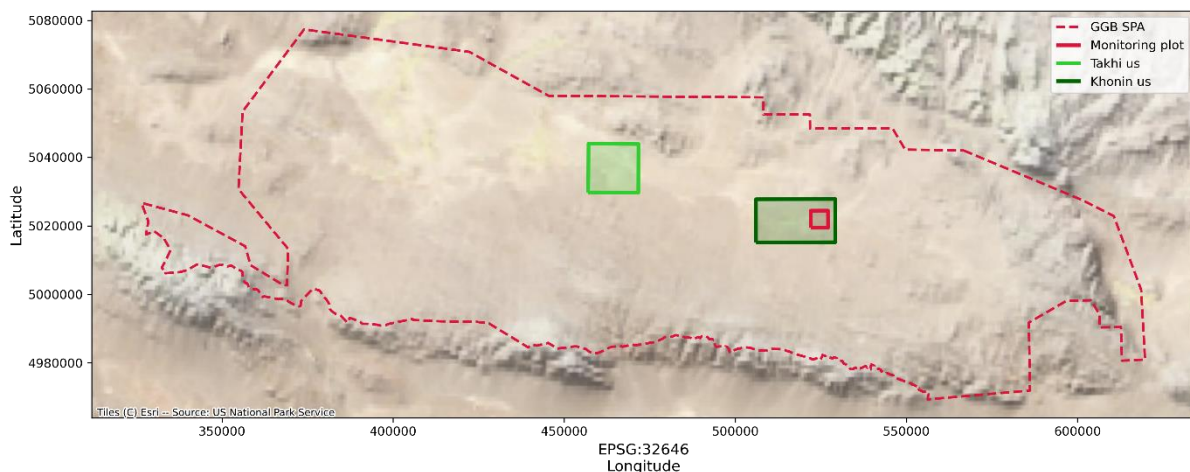


Figure 18: Location of Takhi us and Khonin us oases. The dashed red line represents the boundaries of the Great Gobi B Strictly Protected Area. The monitoring plot (red line) is included for orientation.

3.2 Land cover and vegetation community mapping

In this second practical part, vegetation community mapping for the whole area of the GGB SPA was conducted similarly to Chuluunkhuyag et al. (2021) for 2019 and 2020, but with S-1

3 Methods

and S-2 data (Figure 19). The objectives were to determine the importance of the individual variables and the influence of additional predictor variables on the performance of a Random Forest model.

In the first practical part, the vegetation density from S-2 could be determined with LSMA. However, no vegetation communities could be distinguished from each other by unsupervised clustering (cf. chapter 4.1.4). These findings increased the importance of such a vegetation community mapping.

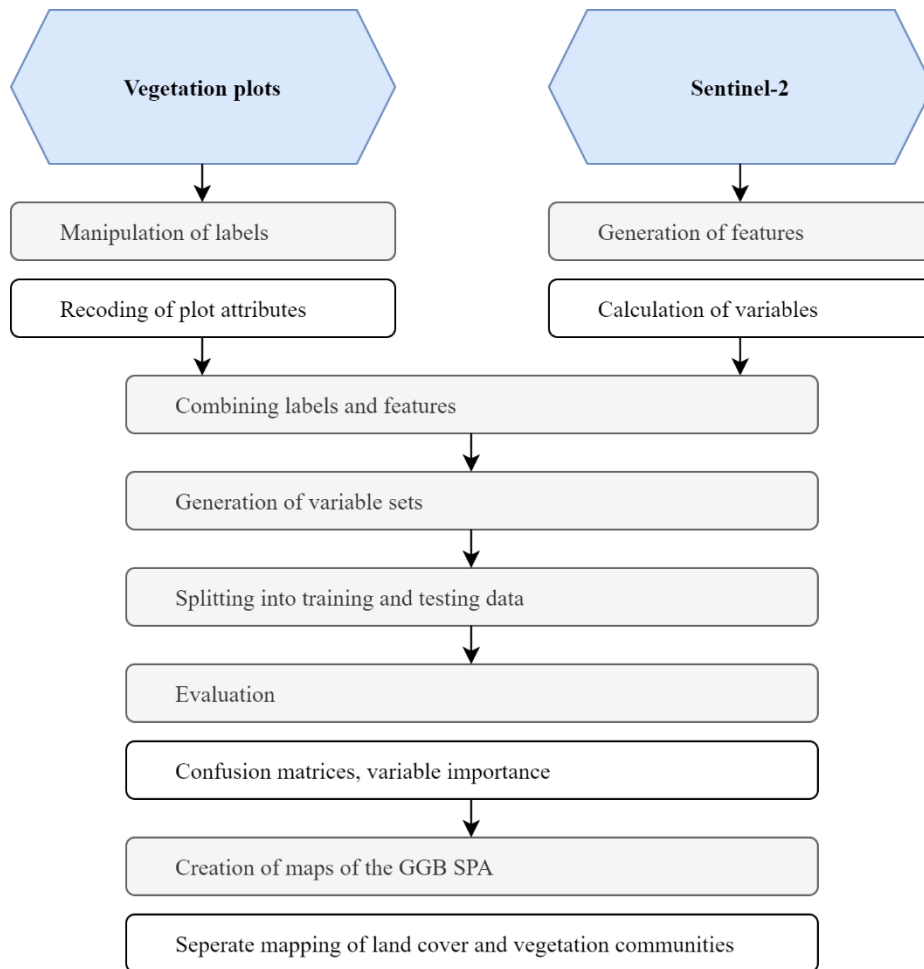


Figure 19: Processing workflow of land cover and vegetation community mapping. Blue boxes represent data, and grey boxes represent steps with optional comments in white boxes

3.2.1 Input labels

The training data was the same as used by Chuluunkhuyag et al. (2021) (n = 629). Each sample had two labels: land cover and vegetation community (Table 4).

In the case of land cover, it was checked whether the extraction of the desert areas was possible as a first approximation to the habitat area of saxaul. A distinction was made between desert

3 Methods

and non-desert. All samples classified as desert in the dataset of Chuluunkhuyag et al. (2021) were considered as such.

In the case of the vegetation communities, it was examined whether these desert areas could be divided into classes dominated by two separate vegetation communities, desert 1 and desert 2. The division of the desert samples into the two classes was based on Table 4. Saxaul was included in desert 2.

The recoding of labels was necessary because some communities had too few samples to split them appropriately into training and testing sets.

Table 4: Classification of the vegetation plots (here: relevés) used for land cover and vegetation community mapping. Copied from Chuluunkhuyag et al. (2021). The area percentages refer to the map created by Chuluunkhuyag et al. (2021). Most of the Dzungarian Gobi is covered by steppe and desert.

Name of vegetation unit	km ²	%	no. of relevés
Forest communities	731	1	6
Forest steppe (Geranio pseudosibirici-Laricetum sibiricae; <i>Juniperus sabina</i> comm.)	731	1	6
Steppe	36469	56	264
Mountain (moist) pasture (Blysmetum rufi)	5995	9	41
Mountain steppe (Thalictrum petaloidei-Helictotrichetum schelliani phlomidetosum tuberosi)	427	1	8
Mountain steppe (Hedysaro pumili-Stipetum krylovii festucetum valesiacaе, Hedysaro pumili-Stipetum krylovii typicum)	16267	25	91
Desert steppe (Oxytropidi aciphyllae-Caraganetum leucophloae iridetosum tenuifoliae)	6706	10	58
Desert steppe (Allio polyrrhizi-Stipetum glareosae eurotietosum ceratoidis sub.ass)	7073	11	66
Desert	25911	40	278
Desert (Reaumurio soongoricea-Nanophytetum erinacei)	5585	9	90
Desert (Calligono mongolici-Haloxyletum ammodendri reamurietosum songaricae; Stipo glareosae-Anabasetum brevifoliae typicum)	20326	31	188
Oasis	1871	3	96
Saline site (Glycyrrhizo uralensis-Achnatheretum splendidis)	427	1	29
Saline site (Nitrario sibiricae-Kalidietum gracilis, <i>Phragmites communis</i> variant)	414	1	16
Saline site (<i>Salix turanica</i> comm.; <i>Caragana spinosa</i> comm.; <i>Populus laurifolia</i> community)	549	1	23
Saline site (<i>Tamarix ramosissima</i> comm.; Glycyrrhizo uralensis-Populetum euphraticae)	12	<0.1	8
Saline site (<i>Halimodendron halodendron</i> comm.; Halerpesto-Hordeetum brevisubulati)	470	1	20
In total	64982	100	644

3.2.2 Input features

Initially, the variables of the reference mapping were used. Subsequently, these were supplemented with SAR bands as well as temporal and textural variables. Furthermore, variable combinations without SAR and/or without correlated variables were created. Groups of correlated variables were determined using the correlation matrix for 2019, with one variable from each correlated group retained at subjective discretion. For 2020, the same variables were removed. S-1 and S-2 bands, which were included in groups of correlated variables, were not removed.

3 Methods

For the optical data, the annual S-2 median images were used without the optimal pre-processing steps. Temporal variables were calculated from the monthly composites and textural variables from the annual median blue band. For the SAR data I used the annual S-1 median images and for the DEM-derived variables the NASA SRTM DEM.

3.2.3 Model architecture

The same model architecture was used as in the reference mapping; a Random Forest classifier with 500 trees. I assumed that the square root of the number of input variables was used for the number of variables per split. All other parameters were set to default.

Approximately 70% of the samples were used for the training of the model, corresponding to 256 and 183 for non-desert and desert and 256, 50, and 128 for non-desert, desert 1, and desert 2. A 5-fold random subsampling was performed to minimize the influence of the training sample selection.

3.2.4 Validation and mapping

The following accuracy metrics were calculated for each run: overall accuracy, producer's accuracy (PA), user's accuracy (UA), and Kappa value. The mean decrease in impurity (also called mean decrease Gini, MDG) was used as a measure of feature importance.

For both labels, the averaged metrics over the two years were used to determine the best performing combination of variables. These combinations were used to create the land cover and vegetation community maps of the GGB SPA for 2019 and 2020.

4 Results

4.1 Saxaul density estimation

4.1.1 Machine learning models

Usability assessment of field data

Forest inventory 2020

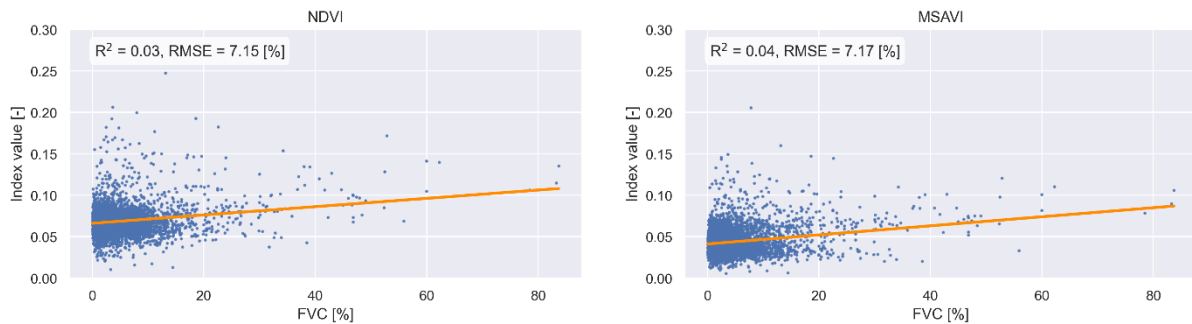


Figure 20: Relationship between vegetation indices and fractional vegetation cover of forest inventory plots. The orange lines represent the linear regression model fit. There is no discernible correlation between vegetation indices and fractional vegetation cover.

No strong correlation between VIs and FVC observable for the 5'924 plots included in the dataset could be observed. Figure 20 shows the relationship between FVC and VIs, using NDVI and the Modified Soil Adjusted Vegetation Index (MSAVI) as examples.

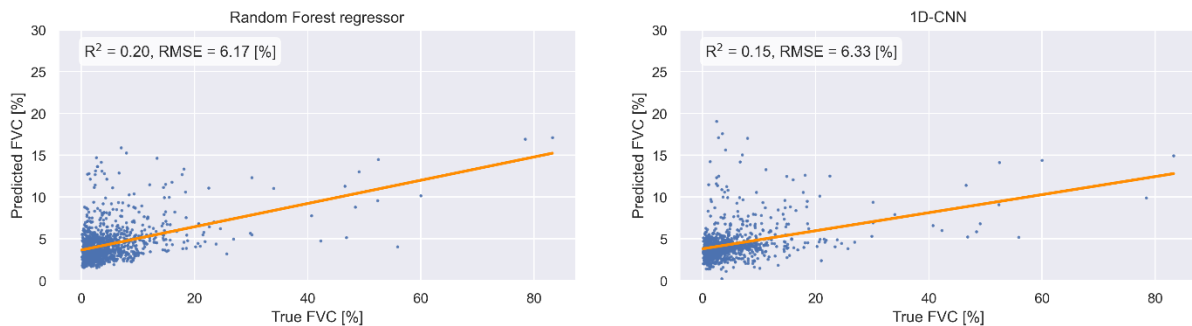


Figure 21: Fractional vegetation cover of forest inventory plots and model estimates. The range lines represent the linear regression model fit. There is no strong correlation between the fractional vegetation cover of the forest inventory plots and the fractional vegetation cover estimated by the Random Forest (left) and the 1-D Convolutional Neural Network model (right).

Neither RF-R nor 1D-CNN could predict the plot's FVC based on their spectral signatures with satisfactory accuracy (Figure 21). In the case of the model predictions, R^2 was higher and RMSE was lower compared to the FVC-VI relationships. The RF-R performed slightly better than the 1D-CNN.

I decided to not use the data any further due to the weak relationship between FVC and VIs and the low accuracy of the model predictions.

4 Results

GGB SPA ranger records

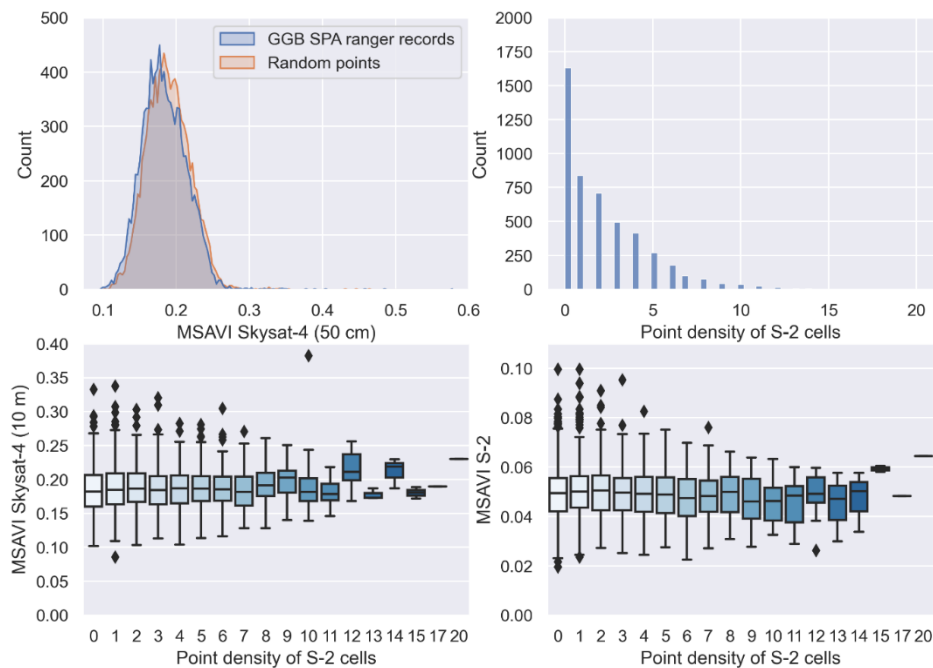


Figure 22: Usability assessment of Great Gobi B Strictly Protected Area ranger plots. Histograms of MSAVI values of the records and random points sampled in the SkySat-4 image (upper left), histogram of point density of S-2 cells overlapping the transects (upper right), boxplots of MSAVI values per point density bin of S-2 cells sampled in the aggregated SkySat-4 and S-2 images (lower left and lower right, respectively). The colour gradient in the bottom plots is for orientation only.

The expected distributions of the index values were a left-skewed distribution for the ranger records and a normal distribution for the random locations. In the present case, the distributions did overlap to a large extent and could not be clearly distinguished from each other. No robust relationship between record point density and index values could be observed for the S-2 cells overlapping the transects (Figure 22).

Because the pre-defined conditions were not met, I did not further use the dataset for the saxaul density estimation.

Visual assessment of saxaul density maps

All generated saxaul density maps (K-means, RF-C, RF-R, LSMA) looked plausible and strongly resembled each other (Figure 24). They depicted the scattered occurrence of saxaul trees and were consistent with the close-range camera images and the subjective visual interpretation of the SkySat-4 image.

Small differences were present between the discrete maps. The density estimate of the K-means clustering was less restrictive than the one of the RF-C. Larger differences were present between the continuous maps, generated with RF-R and LSMA. In the case of LSMA, it was

4 Results

apparent that the saxaul endmember was contaminated by the signal of the soil background. The endmember spectra could only insufficiently explain the composition of the image pixels. Without ASC being activated, the majority of the summed-up endmember fractions were lower than 1 (Figure 23).

Not all maps were equally suitable for further use. The results of K-means and RF-C were discrete, and those of RF-R and LSMA were continuous. Only the latter maps could provide the vegetated fraction of each pixel. Hence, I continued to work with the two continuous maps, even though the saxaul density map of the LSMA was severely affected by the soil background.

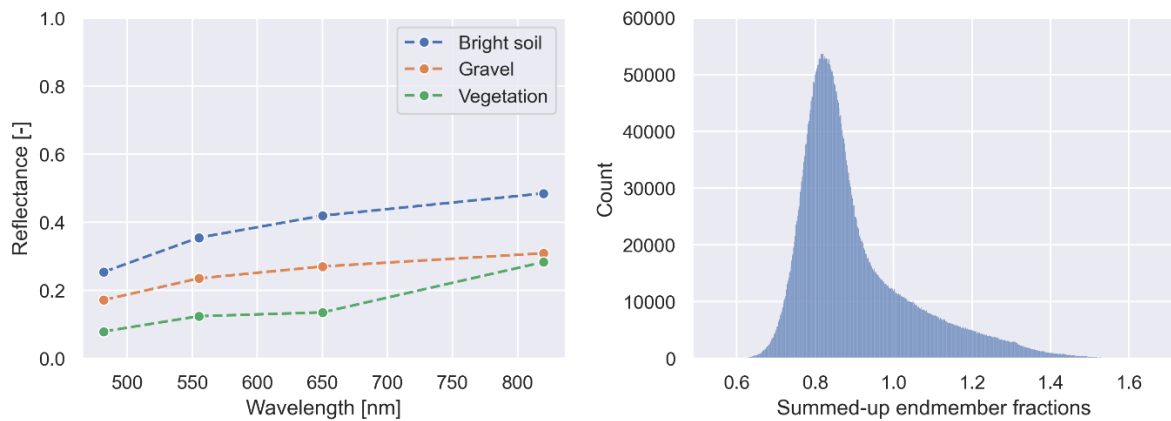


Figure 23: Linear spectral mixture analysis of the SkySat-4 image. Used endmember signatures (left) and summed-up endmember fractions of SkySat-4 linear spectral mixture analysis without active abundance sum-to-one constraint (right).

4 Results

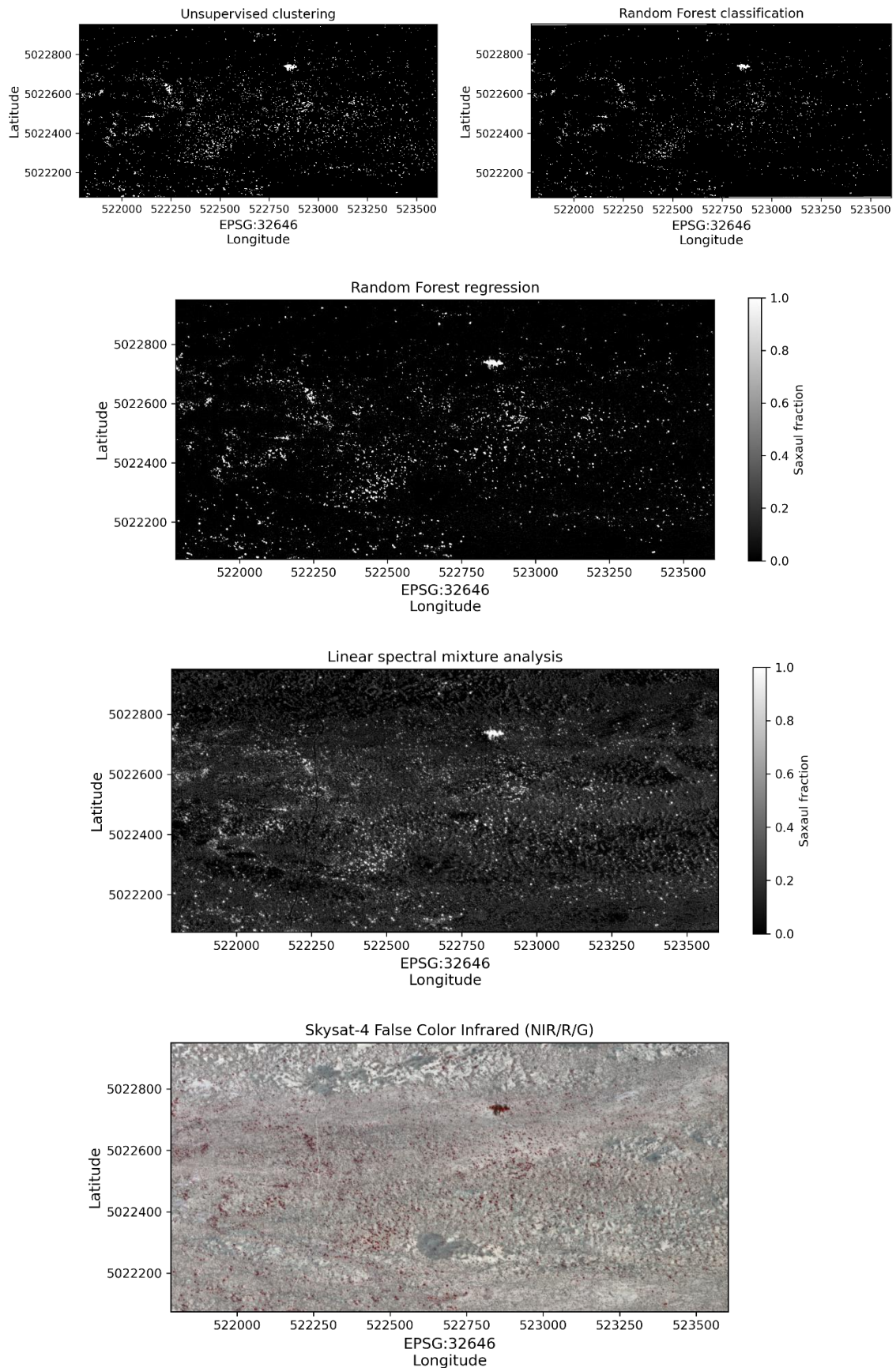


Figure 24: Saxaul density maps generated with the SkySat-4 image. The maps were generated with the following methods: unsupervised clustering (upper left), Random Forest classification (upper right), Random Forest regression and LSMA. Reddish color in the SkySat-4 False Color Infrared image corresponds to vegetation (center from top to bottom).

4 Results

Determination of predictor variables

Table 5 shows the different variable combinations. It should be noted that the O-combinations were identical for both models, RF-RF and RF-LSMA. This was not the case for the R-combinations (Table 6).

Table 5: Overview of composition and naming of variable combinations for machine learning models. The variables included in the groups (cf. Table 2) were used as input features for Random Forest regression models for saxaul density estimation. The most important variables were determined using mean decrease Gini.

Combination of variable groups	Number of features	Combination ID
<ul style="list-style-type: none"> S-2 bands 	10	O10
<ul style="list-style-type: none"> S-2 bands S-1 bands and indices 	13	O13
<ul style="list-style-type: none"> S-2 bands S-1 bands and indices S-2 indices 	27	O27
<ul style="list-style-type: none"> S-2 bands S-1 bands and indices S-2 indices Textural and temporal variables 	40	O40
<ul style="list-style-type: none"> 13 most important variables 	13	R13
<ul style="list-style-type: none"> 7 most important variables 	7	R7

4 Results

Table 6: Variables included in R13 and R7 combinations of the RF-RF and RF-LSMA models. The composition of the combinations was not identical because different training samples and input labels were used.

Combination	Elements
RF-RF R13	Greenness, NDVI, RVI, MSAVI, Blue, DVI, NGBDI, GNDVI, NDVI Std., EVI, Red, MSAVI Std., Brightness
RF-RF R7	Greenness, NDVI, RVI, Blue, NGBDI, NDVI Std., MSAVI
RF-LSMA R13	Greenness, GNDVI, NDVI, Blue, RVI, NGBDI, MSAVI, DVI, Sum Average, Green, Brightness Std., EVI, Red
RF-LSMA R7	Greenness, GNDVI, NDVI, Blue, NGBDI, RVI, MSAVI

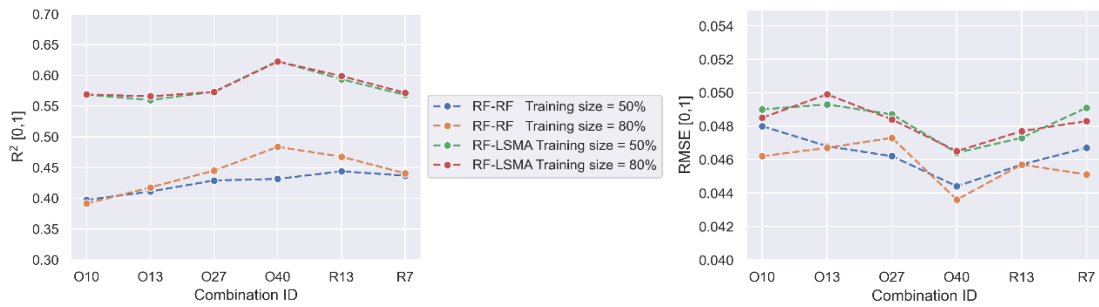


Figure 25: RF-RF and RF-LSMA model performances with different training set size. The coefficient of determination (left) and the root mean square error (right) were positively related to the number of variables in a combination (cf. Table 5). The size of the training set compared to the testing set was of secondary importance.

Figure 25 shows the averaged model performance metrics obtained with 3-fold random subsampling. First, it was noticeable that the labels had a greater influence on the performance than the size of the training set. The RF-LSMA labels had a higher correlation coefficient and a slightly higher error than the RF-RF labels. The size of the training set only caused small differences for the RF-RF labels.

The performance metrics improved with an increasing number of variables. Accordingly, the reduction of the number of variables led to worse results. However, the results for R13 were better than for O13. I concluded that the R13 combinations with a train/test split of 50/50 represented the best trade-off between performance and complexity for both methods.

Figure 26 shows the estimated saxaul density of both models for the extent of the SkySat-4 image.

4 Results

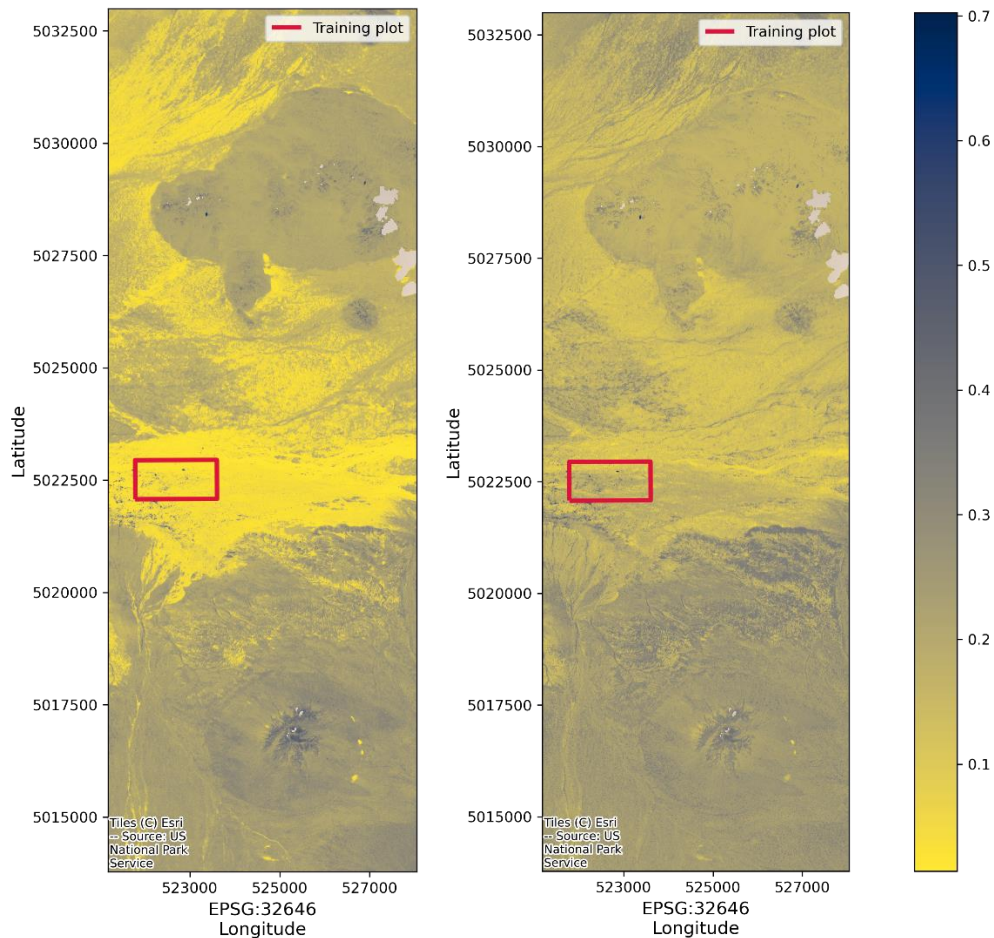


Figure 26: Estimated saxaul density of machine learning models. The RF-RF (left) and RF-LSMA models (right) were trained within the training plot (red line) and estimated the saxaul density for the extent of the SkySat-4 image. Light grey artefacts in the northeast represent masked clouds.

4.1.2 Linear spectral mixture analysis of Sentinel-2 imagery

Algorithm-extracted and simulated endmember spectra

The sets of algorithm-extracted endmembers were similar. PPI, N-FINDR, and VCA had in common that the reflectance for all endmembers and all spectral bands was > 0 . Three MVC-NMF-extracted endmembers included negative reflectance values. No endmember exhibited the characteristic properties of a vegetation signature, such as peaks in the green and NIR regions. The spectral signatures of the algorithm-extracted endmembers can be found in Supplementary materials C.

The simulated endmembers corresponded to typical vegetation signatures. In the combined endmember set, no negative reflectance values were included, as the MVC-NMF endmembers 1, 2, and 4 were sorted out for not corresponding to typical soil signatures. Figure 27 shows the simulated endmembers before scaling and the combined endmember set after scaling.

4 Results

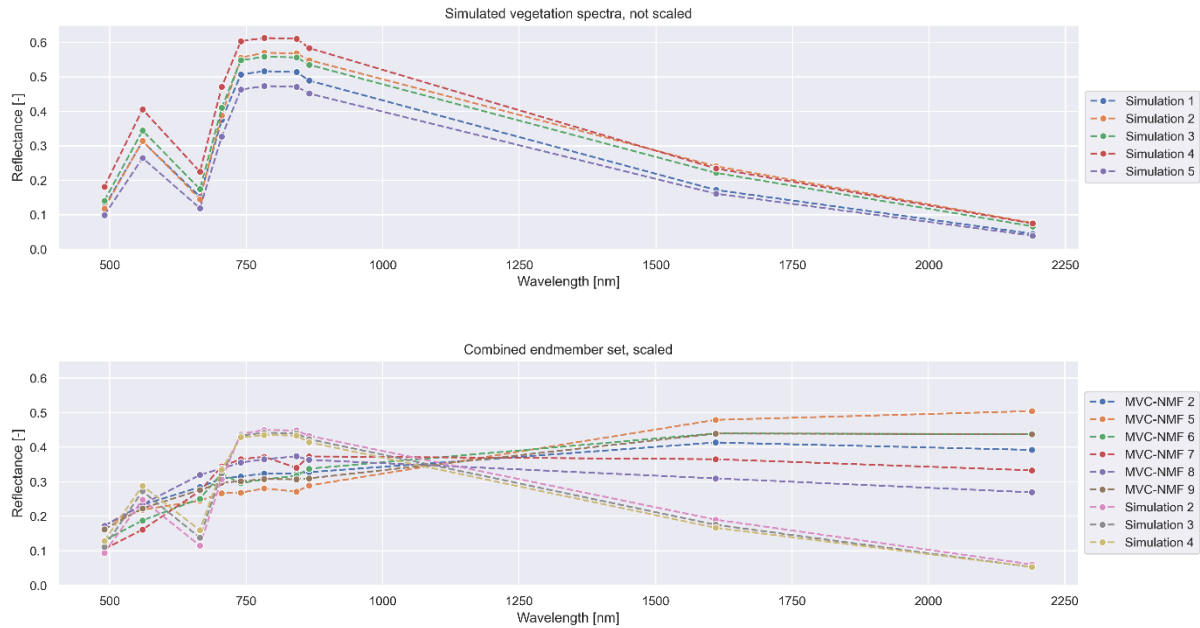


Figure 27: Spectral signatures of simulated endmembers and combined endmember set. The endmembers simulated with PROSPECT-4 corresponded to typical vegetation signatures with peaks in the visible green and near infrared part of the electromagnetic spectrum (top). For the combined endmember set, algorithm-extracted soil endmembers were added (bottom). For scaling, each spectrum was divided by the total energy in the spectrum to convert it to a unit vector with length = 1.

Abundance maps

As previously mentioned, none of the algorithm-extracted endmembers exhibited a vegetation-like spectral signature. Hence, I decided not to use the endmember sets with only algorithm-extracted endmembers any further.

Figure 28 shows the results of the LSMA with the combined endmember. The summed-up fraction of the simulated endmembers showed good agreement with the SkySat-4 image (cf. Figure 24). For most pixels, the sum of the endmember fractions without active ASC was close to 1. I decided to only validate the result of the combined endmember set.

4 Results

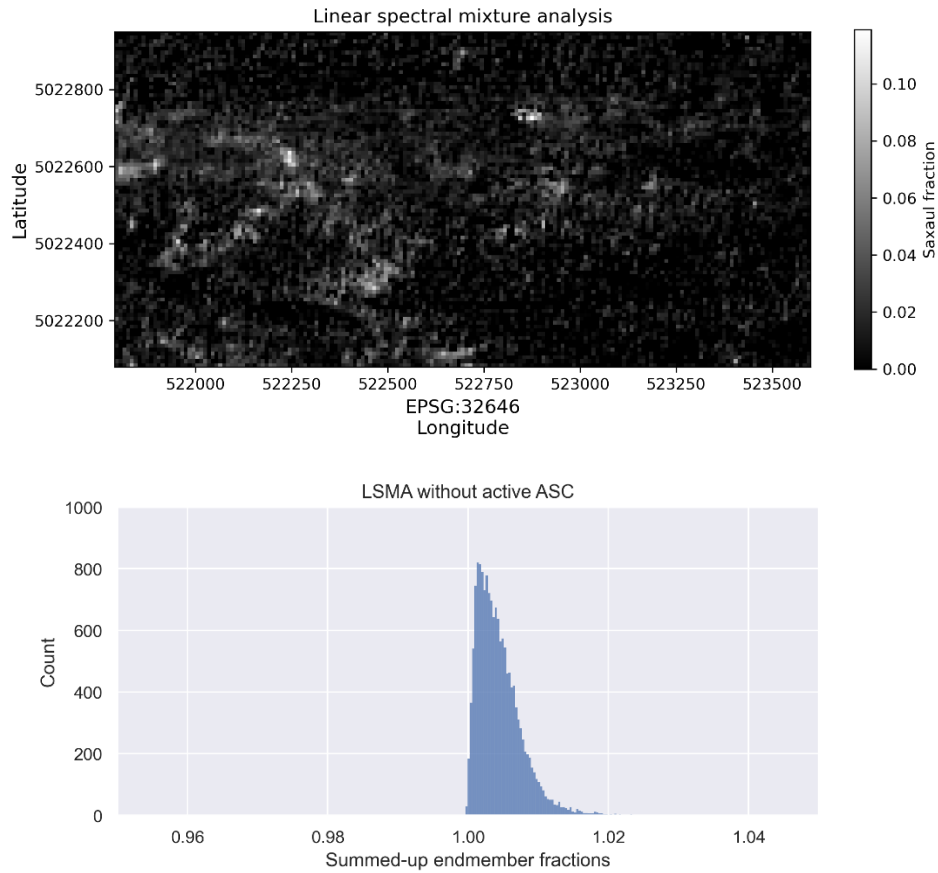


Figure 28: Linear spectral mixture analysis of Sentinel-2 image with combined endmember set. The saxaul density was expressed through the summed-up abundance of the saxaul endmembers (top). The summed-up endmember fractions of Sentinel-2 linear spectral mixture analysis without active abundance sum-to-one constraint were close to 1 (bottom).

4.1.3 Validation

The validated methods included the two machine learning models (RF-RF and RF-LSMA) and the summed-up fraction of simulated endmembers (hereafter referred to as S2-LSMA). Table 7 shows the calculated metrics, R^2 and RMSE, for the two validation plots.

In the case of the larger validation plot located south of the training plot, the calculated metrics were of the same order of magnitude for all three methods. RF-RF led to the best results, followed by RF-LSMA and S2-LSMA.

In the case of the smaller validation plot located 5 km southeast of the training plot, the differences were substantial. S2-LSMA performed best, the metrics were similar to those of the larger validation plot. The results of the other two methods showed no agreement with the validation data.

I decided to proceed with S2-LSMA because the results were more spatially consistent.

4 Results

Table 7: Validation results of the compared saxaul density estimates. The calculated metrics were of the same order of magnitude for all three estimates for the larger validation plot close to the training plot (top). Only the S-2 LSMA estimate showed an agreement with the smaller validation plot located about 5 km southeast of the training plot (bottom).

Validation plot large	RF-RF	RF-LSMA	S-2 LSMA
R ²	0.34	0.26	0.29
RMSE	0.07	0.11	0.10

Validation plot small	RF-RF	RF-LSMA	S-2 LSMA
R ²	0.03	0.07	0.25
RMSE	0.25	0.25	0.04

4.1.4 Oases prediction

Table 8 shows the confusion matrices for Takhi us and Khonin us for 2021. For 2019 and 2020, see Supplementary materials D.

Generated clusters could only be assigned to two plant communities: juniper shrubs and salt meadows. No cluster could be assigned to the saxaul community (Tables 9 and 10). In all clusters for which a larger proportion was classified as saxaul, the proportions were also the same or higher for other communities (e.g., Takhi us 2021 clusters 1 and 4; Khonin us 2021 cluster 8 and 10).

4 Results

Table 8: Assignment of vegetation community IDs. The vegetation communities present in Takhi us and Khonin us of von Wehrden and Gungalag (2003) were assigned numerical IDs due to space limitations, which were used in the following tables.

ID	Vegetation community
2	Juniper shrubs
3	Stipa gobica - Anabasis brevifolia
4	Stipa glareosa - Anabasis brevifolia
5	Caragana leucophloea
6	Stipa glareosa - Allium mongolicum
7	Reaumuria songorica - Anabasis brevifolia
9	Haloxylon ammodendron
10	Achnatherum
11	Nitraria sibirica
12	Salt meadows

Table 9: Confusion matrix of Takhi us 2021. The rows correspond to the vegetation community IDs found in the oasis (cf. Table 8). The columns correspond to the K-means clusters. 1'000 points were sampled per vegetation community. The best fit indicator indicates the largest proportion of a cluster that corresponded to a single ID.

↓ ID Clusters →	1	2	3	4	5	6	7	8
2	0	0	21	0	625	0	354	0
4	274	10	0	35	0	4	0	677
5	173	325	1	473	0	6	0	22
6	227	7	34	43	6	77	107	499
9	313	196	6	325	0	37	0	123
10	217	131	8	112	0	97	0	435
11	498	14	0	158	0	23	0	307
12	10	208	528	41	34	0	178	1
Best Fit [%]	29.09	36.48	88.29	39.85	93.98	39.75	55.40	32.80

4 Results

Table 10: Confusion matrix of Khonin us 2021. The rows correspond to the vegetation community IDs found in the oasis (cf. Table 8). The columns correspond to the K-means clusters. 1'000 points were sampled per vegetation community. The best fit indicator indicates the largest proportion of a cluster that corresponded to a single ID.

↓ ID Clusters →	1	2	3	4	5	6	7	8	9	10
2	16	210	0	0	772	0	2	0	0	0
3	4	0	18	279	0	61	105	190	137	206
4	0	0	2	163	0	56	0	409	23	347
5	1	0	447	1	0	460	1	8	0	82
6	0	0	3	456	0	22	2	325	55	137
7	0	5	76	18	0	524	11	83	11	272
9	0	0	44	162	0	170	9	288	64	263
10	0	0	3	437	0	15	9	318	133	85
11	2	0	3	403	0	35	3	397	65	92
12	311	86	21	50	25	22	422	28	11	24
Best Fit [%]	93.11	69.77	72.45	23.16	96.86	38.39	74.82	19.99	27.45	23.01

4.2 Land cover and vegetation community mapping

In the following, the results for the two mappings are presented separately. An alphabetical overview of the features used per combination including variable importance can be found in Supplementary materials E; the correlation matrices for 2019 before and after the removal of features can be found in Supplementary materials F. The removed correlated variables were the following: sum average, dissimilarity, brightness, greenness std., brightness std., and NDVI std.

Table 11 shows the variable combinations used for the testing.

Table 11: Variable combinations used for the land cover and vegetation community mapping. The variable combinations were assigned IDs due to space limitations, which were used in the following tables. An overview of all variables included in the combinations can be found in Supplementary materials E.

ID	Comment
Original	Same as in Chuluunkhuyag et al. (2021)
All	All available variables
All - SAR	S-1 variables removed
All - Corr	Selected correlated variables removed
All - Both	S-1 and selected correlated variables removed

4 Results

4.2.1 Land cover

Accuracy metrics

The results of the different combinations showed only marginal differences (Table 12). The combination without some of the correlated variables led to the best metrics averaged over both years.

The differences between the years were greater than between the combinations. However, no pattern was recognizable. Depending on the combination, the metrics for 2019 were higher (e.g., initial combination) or they differed depending on the metric (all other combinations).

The metrics for non-desert were slightly better than for desert.

Table 12: Accuracy metrics of land cover mapping. For all combinations (cf. Table 11), the accuracy metrics for 2019 and 2020 and the average value over both years are listed.

Metric	Original			All			All – SAR			All – Corr			All - Both		
	2019	2020	Mean	2019	2020	Mean	2019	2020	Mean	2019	2020	Mean	2019	2020	Mean
Overall accuracy	0.80	0.77	0.78	0.79	0.78	0.78	0.79	0.79	0.79	0.80	0.79	0.80	0.79	0.80	0.79
UA Non-Desert	0.84	0.81	0.82	0.82	0.83	0.83	0.83	0.84	0.83	0.83	0.84	0.84	0.82	0.84	0.83
UA Desert	0.75	0.72	0.73	0.74	0.72	0.73	0.75	0.73	0.74	0.76	0.74	0.75	0.74	0.74	0.74
PA Non-Desert	0.81	0.78	0.80	0.81	0.78	0.80	0.81	0.79	0.80	0.83	0.79	0.81	0.81	0.80	0.80
PA Desert	0.79	0.74	0.76	0.75	0.79	0.77	0.77	0.79	0.78	0.76	0.80	0.78	0.76	0.80	0.78
Kappa	0.59	0.52	0.56	0.56	0.56	0.56	0.58	0.58	0.58	0.59	0.58	0.58	0.56	0.59	0.58

Feature importance

Figure 29 shows the ranked feature importance of the different variable combinations averaged over all runs.

4 Results

Elevation was the most important variable for all combinations followed by the temporal change of the MSAVI and wetness (if included). For the combinations including additional variables, temporal and textural variables were among the most important. The two SAR bands, on the other hand, played a subordinate role.

4 Results

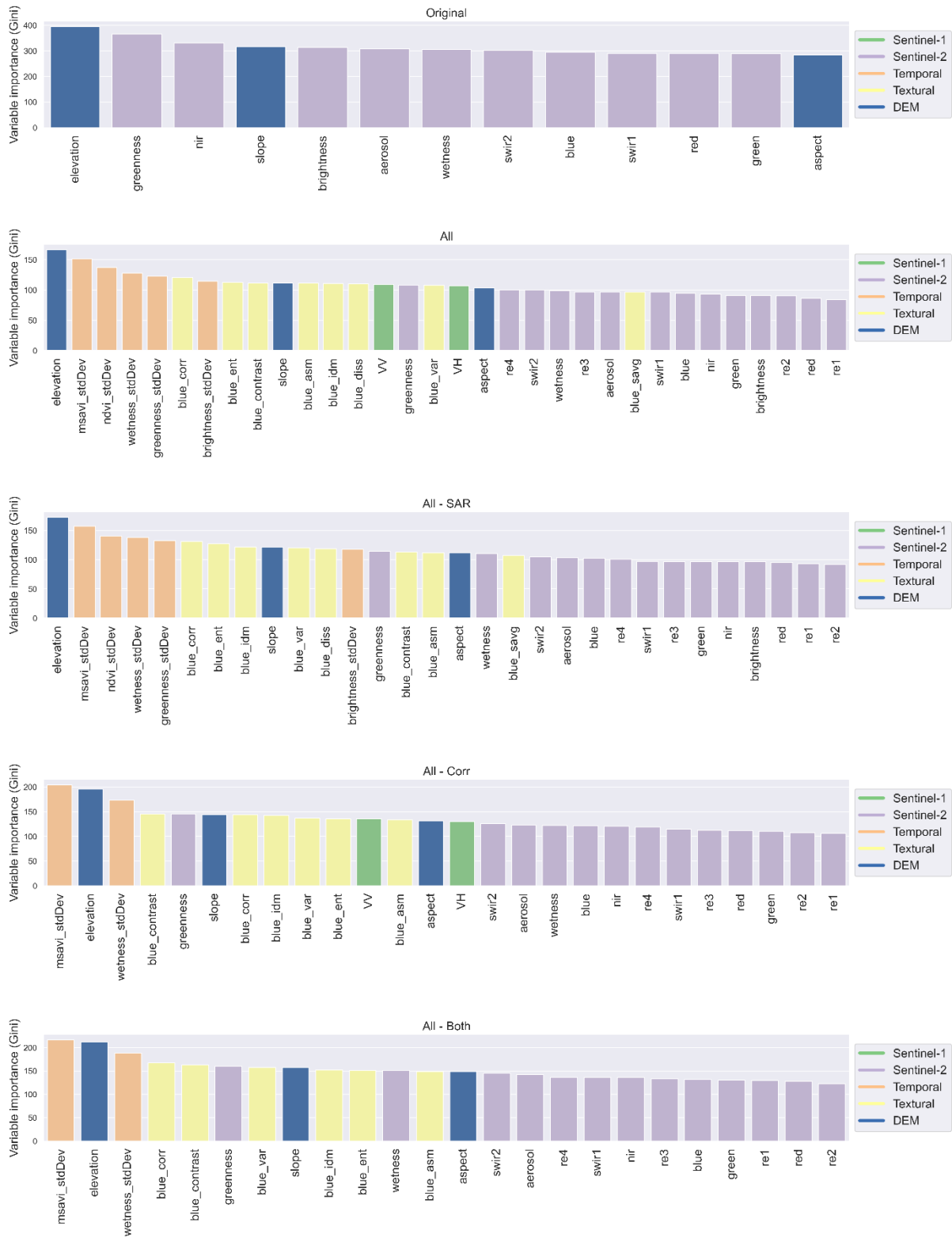


Figure 29: Variable importance of all variable combinations for land cover mapping. The combination IDs are listed in Table 11. The feature importance was expressed through the mean decrease Gini. The colors correspond to variable groups.

4 Results

Yearly maps

The variable combination without some of the correlated variables was used to produce yearly land cover maps for the GGB SPA (Figure 30). The two maps showed a high degree of agreement. Regional differences were observable throughout the area but were particularly evident in the easternmost part of the GGB SPA.

The area shares of desert for 2019 and 2020 were 10'116 and 10'564 km², respectively. This corresponds to 56.24 and 58.73% of the total area of the GGB SPA.

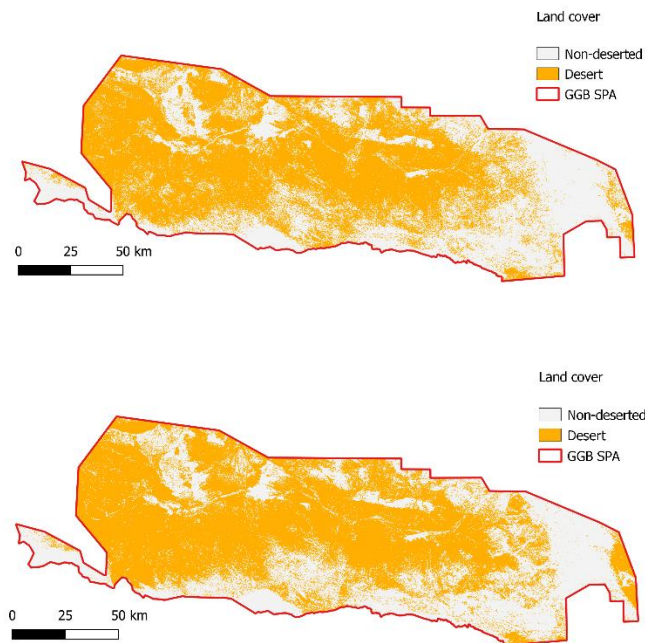


Figure 30: Land cover maps of the Great Gobi B Strictly Protected Area. The red line represents the boundaries of the Great Gobi B Strictly Protected Area. The maps for 2019 (top) and 2020 (bottom) show the spatial distribution of desert estimated with a Random Forest classifier.

4.2.2 Vegetation communities

Accuracy metrics

For the vegetation community mapping, the differences in accuracy metrics were considerably greater by combination and year (Table 13). The combination without some of the correlated variables led to the best metrics averaged over both years. However, several metrics were higher for all combinations with additional variables than for the initial combination (overall accuracy, kappa value, UA and PA of desert 1, and PA of desert 2).

Again, the largest differences were observed between the two years. For example, the difference in UA of desert 1 for the original combination was 0.29.

4 Results

The metrics for non-desert were by far the highest in most cases. In addition, there were considerable differences between low and mediocre accuracy metrics for desert 1 and desert 2.

Table 13: Accuracy metrics of vegetation community mapping. For all combinations (cf. Table 11), the accuracy metrics for 2019 and 2020 and the average value over both years are listed.

Metric	Original			All			All – SAR			All – Corr			All - Both		
	2019	2020	Mean	2019	2020	Mean	2019	2020	Mean	2019	2020	Mean	2019	2020	Mean
Overall accuracy	0.69	0.70	0.69	0.73	0.71	0.72	0.73	0.70	0.72	0.73	0.71	0.72	0.72	0.71	0.72
UA Non-Desert	0.75	0.77	0.76	0.79	0.78	0.78	0.79	0.79	0.79	0.79	0.78	0.79	0.80	0.79	0.79
UA Desert 1	0.23	0.52	0.38	0.65	0.50	0.57	0.49	0.38	0.44	0.54	0.52	0.53	0.46	0.50	0.48
UA Desert 2	0.62	0.60	0.61	0.65	0.61	0.63	0.66	0.61	0.63	0.65	0.63	0.64	0.65	0.62	0.63
PA Non-Desert	0.85	0.83	0.84	0.85	0.83	0.84	0.86	0.82	0.84	0.85	0.83	0.84	0.85	0.83	0.84
PA Desert 1	0.06	0.12	0.09	0.21	0.12	0.16	0.19	0.13	0.16	0.19	0.11	0.15	0.19	0.12	0.16
PA Desert 2	0.66	0.68	0.67	0.73	0.72	0.73	0.71	0.72	0.72	0.73	0.76	0.74	0.72	0.74	0.73
Kappa	0.42	0.44	0.43	0.50	0.46	0.48	0.50	0.46	0.48	0.50	0.47	0.49	0.49	0.47	0.48

Feature importance

Figure 31 shows the ranked feature importance of the different variable combinations averaged over all runs.

Again, elevation was the most important variable for all combinations followed by the temporal change of the MSAVI and wetness (if included). The temporal variables were among the most important for the combinations including additional variables. The textural and SAR variables provided added value to the model in roughly equal proportions

4 Results



Figure 31: Variable importance of all variable combinations for vegetation community mapping. The combination IDs are listed in Table 11. The feature importance was expressed through the mean decrease Gini. The colors correspond to variable groups.

4 Results

Yearly maps

Again, the variable combination without some of the correlated variables was used to produce yearly vegetation community maps for the GGB SPA (Figure 32).

For non-desert and desert 1, larger differences between the maps were noticeable in the east of the GGB SPA. For desert 2, which includes saxaul, no significant differences were observed.

The area shares of desert 1 for 2019 and 2020 were 434 and 669 km², respectively. This corresponds to 2.41 and 3.72% of the total area of the GGB SPA. The area shares of desert 2 were 8'141 and 8'323 km² or 45.26 and 46.27%, respectively.

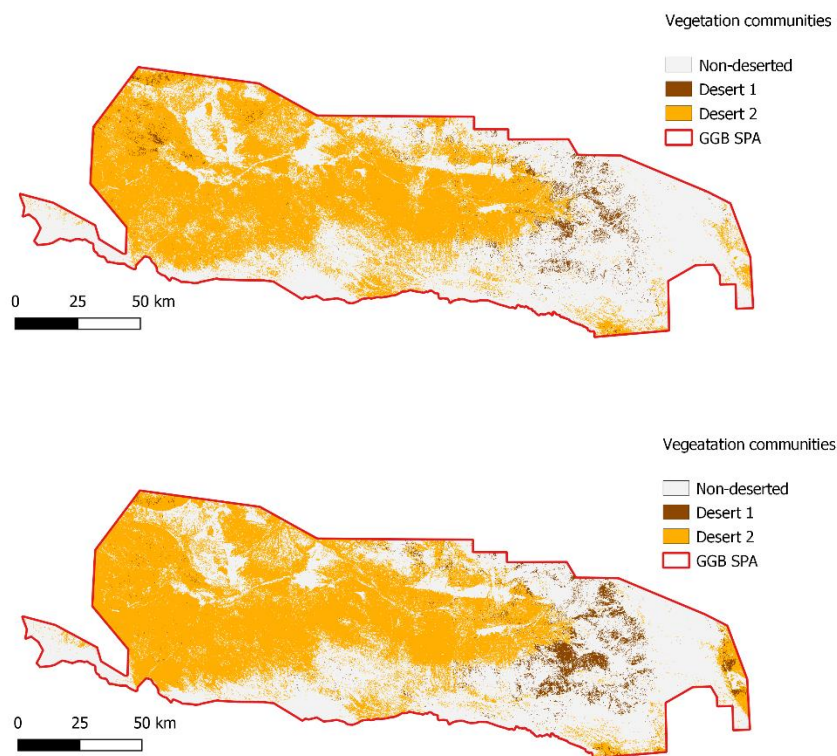


Figure 32: Vegetation community maps of the Great Gobi B Strictly Protected Area. The red line represents the boundaries of the Great Gobi B Strictly Protected Area. The maps for 2019 (top) and 2020 (bottom) show the spatial distribution of desert vegetation communities estimated with a Random Forest classifier.

5 Discussion

This chapter is divided into four parts. The first part deals with the field and satellite data, i.e., how the data availability had an impact on the workflows and to what extent the (pre-)processing might have influenced the results. In the second and third parts, I reflect and evaluate the methods and results of the two practical parts of the thesis. The fourth part outlines possible solutions to the difficulties encountered in connection with possible future data acquisition and field work.

5.1 Field data and satellite data

5.1.1 Data availability

Forest inventory 2020

The rejection of the forest inventory is unfortunate, as the dataset covers a large area of the GGB SPA and would have been valuable for our project due to its high information content. The reason for not meeting the usability criteria is not known to us, I can only make assumptions. First, information could have been lost in the (pre-)processing of the S-2 data. Second, VIs should be interpreted with caution, as they are based on assumptions about illumination effects and influenced by the viewing geometry (Damm et al., 2015; Verrelst et al., 2008). However, the positive correlation between VIs and FVC is usually strong (Coppin et al., 2004). Therefore, I would have expected at least a moderate correlation. Third, misinterpretation of the data cannot be fully excluded. The project reports are written in Mongolian, and despite the availability of machine translations and the great commitment of Batsukh Jamiyandorj, the content of the project reports remains mostly unclear to us. Unfortunately, it was not possible to establish fruitful communication with the data collectors. Nevertheless, such forest inventories could be a useful data source for saxaul research if they are made available and misinterpretation of the data can be excluded.

GGB SPA ranger records

The field survey of the GGB SPA rangers was the most valuable source of field data. I suspect that the spatial inaccuracy of the GPS devices was responsible for not finding a relationship between the records and the SkySat-4 image pixels. However, the close-range camera pictures allowed detailed insight into the composition of the surface and played a key role in the visual

image interpretation. However, this method of obtaining field data is only suitable for smaller areas with a land cover that is not too heterogeneous.

SkySat-4

The spectral differences between the individual scenes in the SkySat-4 image led to a further spatial limitation when testing and validating the methods. Outside of the training and validation plots, it was difficult to clearly distinguish vegetation from the surroundings. This had a particular impact on the spatial validity of the methods for saxaul density estimation (cf. chapter 5.2).

5.1.2 (Pre-)processing

The influence of the individual (pre-)processing steps on the results cannot be quantified within the scope of this thesis, as this would require sensitivity analyses. Even with only two sensors, the pre-processing consists of several steps with multiple possibilities for modification and optimisation. Some issues with potentially significant impact on the results are discussed below.

Sentinel-1

As outlined in chapter 2.5.1, several complex steps are necessary to obtain an S-1 ARD product. This can be a challenging task, especially in the case of large data sets due to the spatial extent and/or the length of the study period (Wagner et al., 2021). Thanks to the workflow implemented in the GEE, S-1 data become easier to use for projects such as ours while allowing some flexibility in terms of parametrisation. However, this also means that the user must decide on suitable parameter values and the data is processed on demand. Regarding the parameters, I relied exclusively on literature, although alternative parametrisation would have been possible. A method for determining the optimal speckle filter and window size would be useful to prevent the loss of image information. Figure 33 shows the different VH backscatter coefficient time series for vegetated and non-vegetated pixels inside the monitoring plot. I interpret the fact that the S-1 data show some correlation with land cover as an indication of the basic adequacy of pre-processing. Processing on demand implies that the memory limit of the GEE must not be exceeded, and intermediate products must be exported. This can lead to memory bottlenecks. For this reason, the yearly products for the area of almost 18'000 km² were calculated from the monthly medians. However, finer subdivision of the data would allow other workflows, such as iterative calculation of yearly products of spatial subsets.

5 Discussion

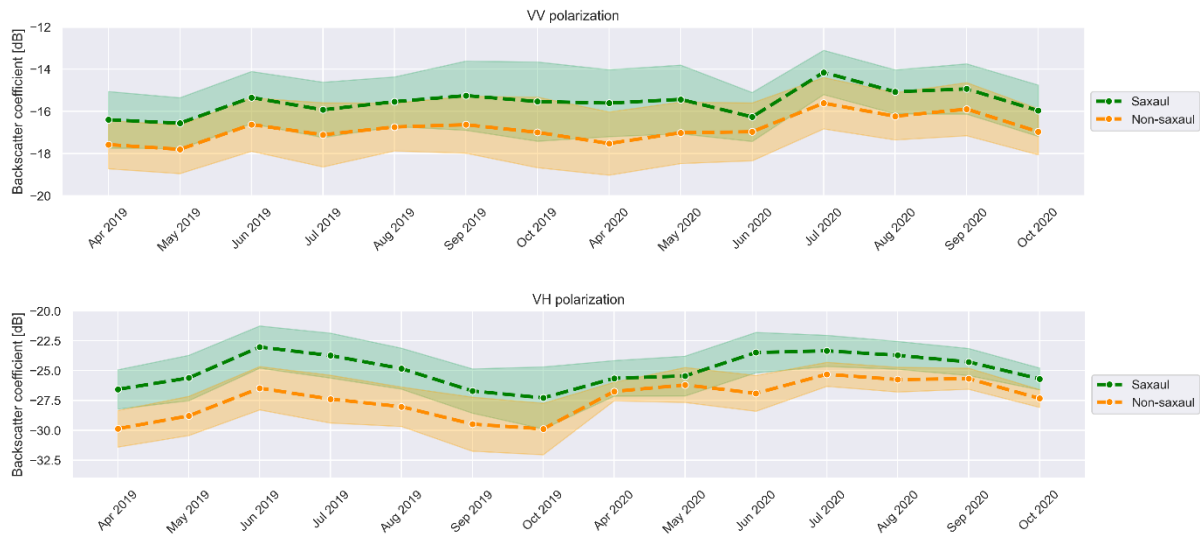


Figure 33: Time series of Sentinel-1 backscatter coefficients of saxaul and non-saxaul areas in VV and VH polarisation. Lines represent the mean of 50 points per category, the bands represent the mean ± 1 standard deviation. The sampling points were selected by visual interpretation of the SkySat-4 image.

One of the major discussion points in the academic literature regarding S-1 data and the GEE is the terrain normalisation. Its application is a prerequisite for the comparability of SAR backscatter over larger regions, especially in the case of uneven terrain (Waser et al., 2021). The Committee on Earth Observation Satellites (CEOS) recommends the use of the pixel-area-based gamma nought introduced by Small (2011) (CEOS, 2019). The angular-based slope correction implemented in the GEE workflow of Mullissa et al. (2021) is not as accurate as gamma nought, but computing gamma nought is not possible without the state orbit vectors, which are not available in the GEE assets (Vollrath et al., 2020). However, other cloud-based S-1 ARD products, such as the S-1 backscatter datacube (Wagner et al., 2021), also use sigma nought instead of gamma nought due to the computational complexity of the latter. This makes clear that cloud-based environments create a variety of new opportunities to analyze large amounts of S-1 data, but local processing on a smaller scale may have advantages depending on the application. Markert et al. (2020) pre-processed S-1 data locally including radiometric terrain normalisation and found that it is better suited for surface water mapping than the S-1 data available in the GEE.

In the present thesis, the appropriateness of the choice of parameters and the angular-based slope corrected product was assumed. First, because of the correlation in Figure 33, and second, because the pre-processing workflow by Mullissa et al. (2021) was also used in other studies (Kacic et al., 2021; Verhelst et al., 2021). In addition, local pre-processing and uploading of 293 S-1 images would have been disproportionate.

Sentinel-2

Several pre-processing steps of the S-2 data were functions implemented by Nguyen et al. (2020) and debugged by the student if needed. However, the correctness of the used functions cannot be guaranteed. For example, numerous coefficients are used for the BRDF correction whose correct implementation has not been fully verified by our side.

The TCT certainly had an impact on the validity of our results. The coefficients used were calculated for at-sensor reflectance and not for surface reflectance (Shi and Xu, 2019). In the case of S-2 data, the atmospheric correction as implemented in Sen2Cor performs the transformation from at-sensor reflectance to surface reflectance (Müller-Wilm, 2017). Consequently, the coefficients cannot be easily adjusted for surface reflectance, which means that the TCT variables calculated in this thesis were flawed and all statements depending on them should be interpreted with caution.

SkySat-4

The mean reflectance of the SkySat-4 pixels included in the S-2 pixels was used to harmonize the spatial resolution of SkySat-4 and S-2. Reducing the spatial resolution in this way is not new. Claverie et al. (2018) calculated the mean to reduce the spatial resolution of S-2 data from 10 to 30 m (from 9 to 1 cell). In this thesis, the spatial resolution of SkySat-4 was reduced from 50 cm to 10 m (from 400 to 1 cell), which corresponds to an increase of more than 44 times. Such harmonisation leads to identical pixel size, but not necessarily to comparable data (Figure 34).

First, the smoothness of the images differed. One reason could be that different algorithms were used for the atmospheric correction, which estimate the influence of path radiance and adjacency radiation, influencing the calculated surface reflectance value (Richter and Schläpfer, 2017).

Second, the aggregated SkySat-4 and S-2 images were spatially misregistered. Spatial misregistration can lead to large errors, even if the misregistration is in the sub-pixel range (Townshend et al., 1992). Accordingly, the labels based on the SkySat-4 image with reduced resolution used as input for the machine learning models (RF-RF and RF-LSMA) arguably exhibited spatial misregistration in the sub-pixel range.

5 Discussion

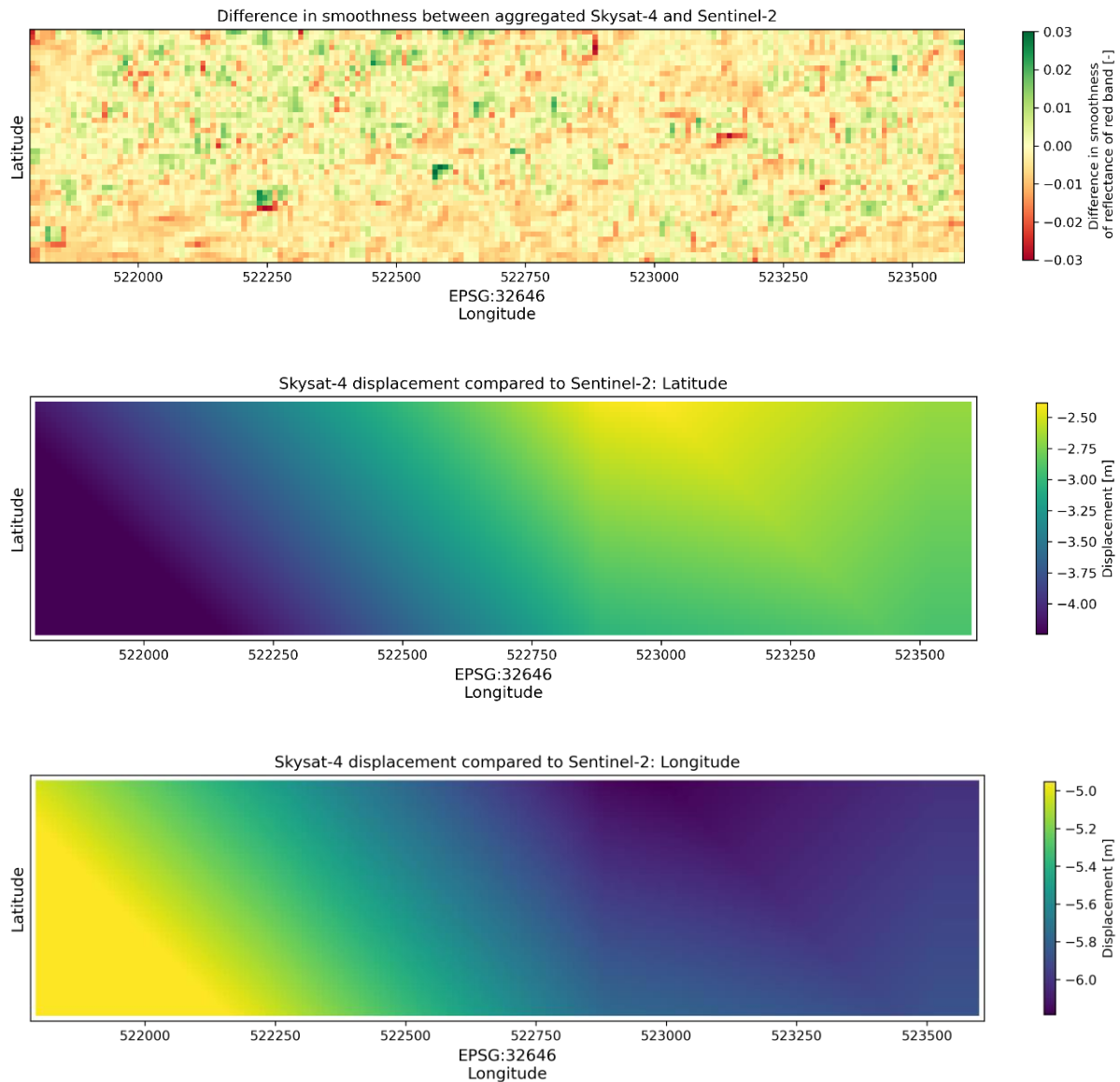


Figure 34: Comparison of aggregated SkySat-4 and Sentinel-2 data. The difference in smoothness between aggregated SkySat-4 and S-2 data was calculated as the standard deviation of the red band in a 3 x 3 window (top). Positive values indicate a lower smoothness of the aggregated SkySat-4 image. The latitudinal (middle) and longitudinal displacement of the SkySat-4 image compared to the S-2 image (bottom) was determined using the displacement()-function in the Google Earth Engine.

5.2 Saxaul density estimation

In the following, issues regarding the first practical part of the work are addressed. These include the selection of methods, problematic aspects of data processing, intermediate steps which were not taken into account, and a statement about the usefulness of the generated product.

5.2.1 Image classification methods

Remote sensing offers a variety of methods for image classification, which can be divided into pixel-based, sub-pixel-based, and object-based (Li et al., 2014). For obvious reasons, the

number of methods that can be tested for a specific application is limited. I worked exclusively with pixel and sub-pixel-based methods, e.g., Random Forest regression and LSMA, respectively. These two groups of methods are particularly well suited if the target of interest is smaller than the pixel size (Praticò et al., 2021). This is clearly the case for sparse saxaul forests.

Theoretically, it would also have been possible to use object-based methods to shift the focus away from the individual trees to the forests. Object-based methods have been successfully applied to cropland mapping with S-2 data (Belgiu and Csillik, 2018). However, the distinction between cropland and surroundings is easier than between sparse saxaul forests and non-forested areas. I decided against using object-based methods because the distinction between forest and non-forested areas would have been more arbitrary than the identification of individual trees in the SkySat-4 image.

5.2.2 Machine learning models

Model selection

The estimation of the saxaul density outside the training area was performed with a RF regressor. RF belongs to the non-parametric methods, which do not need normally distributed input variables and are among the most used methods for image classification in the GEE (Belgiu and Drăgu, 2016; Tamiminia et al., 2020). In multisource remote sensing, parametric methods are less accurate and not recommended (Gislason et al., 2006; Sarzynski et al., 2020).

RF and Support Vector Machine (SVM), also a non-parametric method, perform well with high-dimensional input data (Zafari et al., 2019). However, SVM is sensitive to kernel design and performs better if the input variables are standardised (Luor, 2015; Zafari et al., 2019). RF, on the other hand, copes well with a high number of features, multicollinearity, and noise, and is not as susceptible to overfitting (Belgiu and Drăgu, 2016; Zafari et al., 2019). Moreover, the parametrisation of a RF model is less complicated than the tuning of an SVM kernel. For two important parameters, the number of trees and the number of variables per tree, good experience has been made with 500 trees and the square root of the number of input variables (Chuluunkhuyag et al., 2021; Gislason et al., 2006).

Deep learning methods might lead to better results in land cover classification, but the high demand for training data can be problematic (Song et al., 2019; Yuan et al., 2020). In the present thesis, I estimated the chances of success in developing a well-functioning deep

5 Discussion

learning model to estimate saxaul density as low because the amount of available training data was limited. As of today, deep learning methods are not implemented in the GEE. Pre-trained models can be imported from the Google Cloud Platform (GCP) (Arruda et al., 2021). However, the GCP is not always free of charge.

The focus on RF was ultimately a question of feasibility, complexity, and comprehensibility of the model's mode of operation.

Selection and derivation of predictor variables

Regarding the textural variables, the findings of other studies on GLCM metrics and kernel size were used (Pandit et al., 2020; Verde et al., 2020; Zheng et al., 2017). However, these studies do not refer to a desert ecosystem. A sensitivity analysis could help to determine the most appropriate metrics and kernels. If the kernel is too small, the texture will not be captured and if the kernel is too large, different textures will be mixed. The optimal kernel size could be approximated by spatial autocorrelation (Haralick et al., 1973).

The incorrect calculation of the TCT variables (cf. chapter 5.1.2) also affected the temporal variables. This influence of this calculation error is difficult to quantify, but I assume a considerable error as brightness and greenness were among the most important variables in both models, RF-RF and RF-LSMA.

It is therefore possible that the combinations of predictor variables contained erroneous variables and/or important variables were not considered.

Determination of feature importance

The mean decrease in impurity (MDG) was used to determine the most important variables for reducing dimensionality. Behnamian et al. (2019) have shown that MDG scores are not accurate for correlated variables. In our groups of predictor variables, multicollinearity was present. Therefore, it would have been more accurate to reduce the multicollinearity within the input data by dropping correlated variables before calculating MDG scores. This could have led to a different selection of variables and correspondingly different results.

Spatial issues

Two problems caused by the spatial nature of geographic data need to be addressed. First, statements about the accuracy of the two RF regressor models, RF-RF and RF-LSMA, are valid

only for the surroundings of the training area. The models learn the relationship between FVC and the spectral information using training data, which should cover all present land cover classes. In a region with a different soil background, the regressor is not familiar with the relationship between the spectral information and FVC. Therefore, the model does not produce reliable estimates. Accordingly, the results of the two RF regressor models for the more distant validation plot were poor.

Second, spatial autocorrelation (SAC) may have had an impact on the validity of our results. The concept of SAC can be expressed as follows: *I invoke the first law of geography: everything is related to everything else, but near things are more related than distant things* (Tobler, 1970). In other words, spatially adjacent data points are not independent of each other, which violates basic assumptions of many statistical models (Ploton et al., 2020). SAC was not considered in the training and validation stages of the RF regressor models, which could have led to a significant overestimation of their predictive power (ibid.). Based on tests conducted after the completion of the practical part of this thesis was completed, I assume that the performance of the two models was indeed overestimated. Further details in Supplementary materials G.

5.2.3 Linear spectral mixture analysis of Sentinel-2 imagery

Endmember variability

Algorithm-extracted endmembers have in common that they are site-dependent. They are calculated by an algorithm that approximates the endmember spectra based on the number of endmembers to be found and the spectra present in the given image – if the image input changes, the result also changes. Therefore, the soil endmembers extracted with MVC-NMF are not per se valid for the whole GGB SPA. In addition to the spatial variability, there is also a temporal variability of vegetation endmembers, each of whose spectral signature represents a specific phenological stage (Somers et al., 2011).

Furthermore, endmembers are sensor-specific. The available number of spectral bands determines the maximum possible number of endmembers. In the present thesis, NWHFC was used to determine the number of available endmembers in the S-2 image, resulting in nine endmembers. It is likely that the actual number of endmembers present in the image was much higher, but their identification was not possible. For more precise results, more spectral bands would be necessary, e.g., by using hyperspectral data.

5 Discussion

The appropriateness of the algorithm-extracted endmembers as input for LSMA is therefore limited to the extent of the SkySat-4 image, the time of acquisition, and S-2 data. A LSMA for the whole GGB SPA using these endmembers could result in unreliable estimates.

RTM parametrisation

The simulated endmembers are not site-dependent since they are not generated from the image data. Instead, they depend on the parametrisation of the RTM.

As illustrated in Figure 35, the proportions of the three saxaul endmembers differed considerably. Within the framework of this thesis, only three parameter combinations were tried out (Table 14). No statement can be made about their appropriateness since the parametrisation was experimental and may not correspond to the real situation in the field. For example, the leaf structure parameter (N) refers to the number of homogeneous layers of a leaf (Jacquemoud and Baret, 1990), but saxaul leaves are mostly degenerated and hardly dominate the tree's spectral signature. In addition, simulated vegetation endmembers may only be representative of a specific phenological stage (Schiefer et al., 2021) since parameters such as C_{ab} and C_w are subject to seasonal variation.

The biggest influence on the appropriateness of the simulated spectra was probably an error in the implementation. As was discovered afterward, the custom S-2 sensor with a 10-band configuration was wrongly set-up within the ARTMO toolbox by the student. Instead of B8A (RE4), B9 (water vapour) was used for the simulations. The influence on the result cannot be estimated at this point since the simulation with subsequent LSMA and validation was not repeated shortly before the submission deadline.

5 Discussion

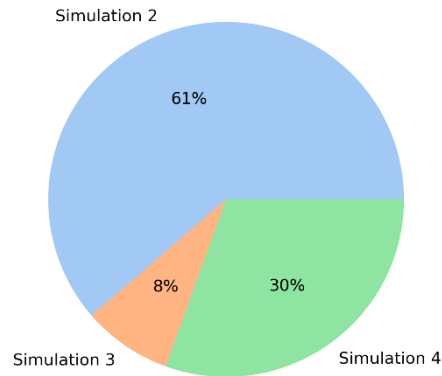


Figure 35: Relative proportions of the three simulated endmembers in the total detected saxaul fraction. The simulated endmembers correspond to the PROSPECT-4 simulated endmembers used for linear spectral mixture analysis of Sentinel-2 data. The total detected saxaul fraction corresponds to the summed-up abundance of these endmembers with active abundance sum-to-one constraint.

Table 14: Traits of the simulated endmembers used for saxaul density estimation. Of five endmembers simulated with PROSPECT-4, three were randomly selected for the linear spectral mixture analysis of Sentinel-2 data. Their respective endmember fractions are shown in Figure 35.

Simulated endmember	N [-]	C_w [cm ³ cm ⁻²]	C_m [g cm ⁻²]	C_{ab} [μg cm ⁻²]
Simulation 2	3.4767	0.0576	0.0274	19.7696
Simulation 3	3.1171	0.0604	0.0245	14.084
Simulation 4	3.6111	0.0713	0.0184	11.8166

Linear mixture assumption

The assumption of linearity is not valid for fine materials with internal reflection like vegetation and soil in desert ecosystems (Ray and Murray, 1996; Winter, 2004). In cases where this condition of linear mixing is violated, Artificial Neural Networks (ANNs) can be used (Lillesand et al., 2015). However, ANNs are not available in the GEE (Tamiminia et al., 2020) and no further testing was done at this point.

5.2.4 Validation

Two factors are believed to have affected the results of the validation. The first was the method by which the validation data were generated. RF regression was used because labeling pixels as vegetated/non-vegetated seemed to us to be less subjective than determining endmembers in SkySat-4 image regions for which close-range camera images were not available. Therefore,

it is possible that the relationship between RF-RF estimate and validation was overestimated. Validation data generated with LSMA and a contaminated vegetation endmember (cf. chapter 4.1.1) would likely have benefited the RF-LSMA.

The second was that the SAC may have biased the model results (cf. chapter 5.2.2). The validation was partially repeated taking SAC into account after completion of the practical part of this thesis. I assume that the statistical metrics were influenced by SAC, but the assessment of the methods would have remained the same. Further details in Supplementary materials G.

5.2.5 Oases prediction

The reference map can be considered relatively accurate for the areas around the oasis complexes (Kaczensky, 2022, personal communication). It is a nominal map; each pixel is assigned to a vegetation class without information about the vegetation density. Saxaul forests cover a large area that; presumably non-vegetated areas were also assigned to this class, which could have influenced the comparison between vegetation classes and clusters.

Since it was not known which cluster belonged to which community, a different type of assignment had to be found. The introduced best-fit indicator is simplistic, but the focus was on coarse correlations. I conclude from the results that no isolation of saxaul trees is possible with FVC and MSAVI(-derived) variables. The phenology could be a reason why saxaul could not be isolated. A single data point per month may not have provided the level of detail needed to distinguish plant species.

5.2.6 Product evaluation

The results show that an estimation of FVC with medium-resolution satellite data is possible. This is an important finding since spatial resolution plays an important role in the extraction of vegetation in arid ecosystems due to the possible dominance of the soil background (Ji et al., 2020). The LSMA of S-2 data with an endmember set consisting of algorithm-extracted soil endmembers and RTM-simulated saxaul endmembers produced the best results.

The proposed method does not rely on field data because the endmembers are calculated from the image or simulated with an RTM. Therefore, the soil endmembers have greater spatial validity than if they were defined manually. However, the ideal parametrisation of the RTM for the detection of saxaul remains largely unknown. The physiological, spatial, and temporal variation could not be adequately accounted for in this thesis. Furthermore, a wrong band was used for the RTM simulations (B9 instead of B8A, cf. chapter 5.2.3).

The distinction of plant species with a clustering approach and estimated FVC and MSAVI-derived variables as input was not possible.

5.3 Land cover and vegetation community mapping

5.3.1 Multicollinearity

This input data for the RF classifier were highly subject to multicollinearity. Removing selected correlated variables improved the model performance to a certain degree. However, the original S-1 and S-2 bands were kept. Accordingly, groups of highly correlated variables remained (cf. Supplementary materials F). Tests have shown that the same classification accuracy could be achieved with only the ten most important variables based on the MDG scores (results not shown). The same limitations on the accuracy of MDG scores in the case of correlated variables apply as in chapter 5.2.2.

5.3.2 Plausibility of results

Based on visual assessment, the resulting maps seem to be plausible. The spatial extent of desert in the land cover maps as well as desert 1 and 2 in the vegetation community maps are roughly consistent with the map of Chuluunkhuyag et al. (2021). In case of the vegetation community mapping, the three most important variables of the initial combination were identical to those of the reference mapping (Figure 36). However, comparisons of feature importance should be interpreted with caution. The GEE returns the mean decrease in impurity (also called mean decrease Gini, MDG), whereas Chuluunkhuyag et al. (2021) reported the mean decrease accuracy (MDA). Absolute values of feature importance also depend on the number of variables.

Furthermore, the maps are similar for each of the two years, which is consistent with our expectations since the land cover and dominant vegetation communities generally change over larger time scales (Figure 37). The differences between the estimated area shares in 2019 and 2020 could be due to the respective amounts of precipitation (Kaczensky, 2022, personal communication).

5 Discussion

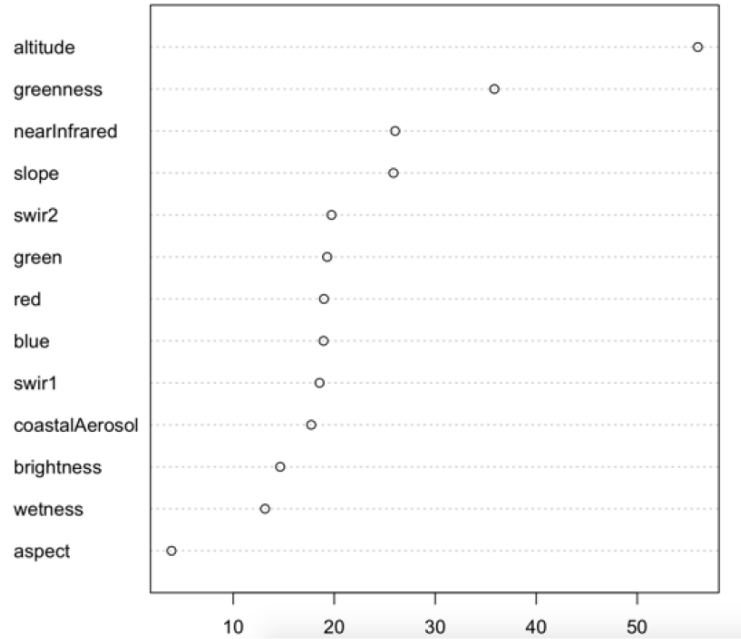


Figure 36: Variable importance of Random Forest model of Chuluunkhuyag et al. (2021). Taken from Chuluunkhuyag et al. (2021). The variable importance is expressed through the mean decrease accuracy.

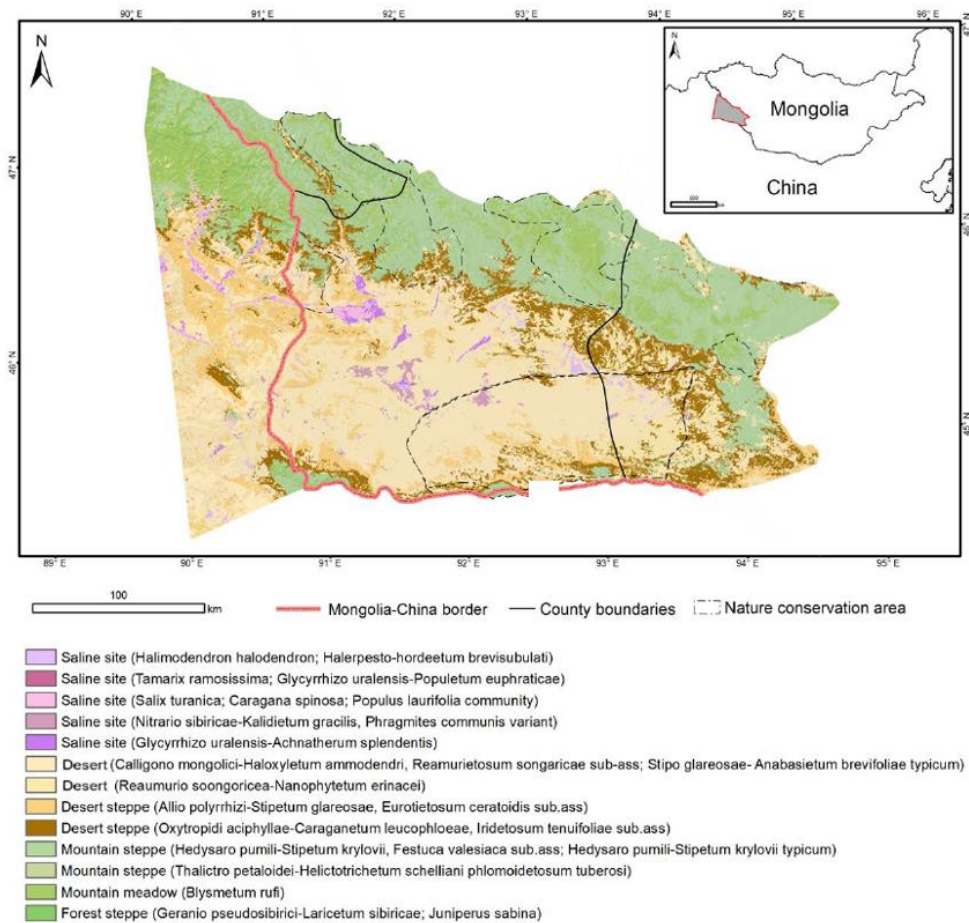


Figure 37: Adapted land cover and vegetation community map of Chuluunkhuyag et al. (2021). The map shows the spatial distribution of land cover classes and dominant vegetation communities in the Dzungarian Gobi and was created with a Random Forest classifier and the vegetation plots described in chapter 2.4.2.

5.3.3 Product evaluation

Detailed knowledge about the distribution of dominant vegetation communities in the GGB SPA is a valuable complement to the vegetation density estimate, as the latter does not allow distinction of individual species. In addition, the part of the GGB SPA relevant for saxaul research could be extracted, reducing data volume and processing time.

In our case, the deserted areas were of particular interest. In the case of land cover mapping, UA and PA of 0.75 and 0.78 were achieved with the best variable combination. In the case of vegetation community mapping, the accuracy metrics were only 0.53 and 0.15 for desert 1, but 0.64 and 0.74 for desert 2 (including saxaul). I rate the model performance as satisfactory. Unfortunately, I do not know of any metrics for the mapping of Chuluunkhuyag et al. (2021). Thus, a direct comparison of model performances was not possible.

Temporal and textural variables increased the classification accuracy whereas the S-1 variables played a subordinate role in vegetation community mapping and were not relevant to land cover mapping. Determination of the exact added value of these variable groups would require a strict reduction of multicollinearity in order not to affect the MDG scores.

5.4 Future possibilities

5.4.1 Field survey design

For a small-scale distinction of plant species, corresponding field data are required. The survey design with transects in the monitoring plot was not successful, presumably because the accuracy of the GPS devices was too low.

I propose a different approach. First, the extent of the GGB SPA is reduced to areas of interest or selected land cover classes, e.g., oases complexes or deserts. Subsequently, either drone flights take place (planned for 2022), or high-resolution satellite imagery is ordered. The field survey takes place after receiving the remote sensing data and is dedicated to labeling the vegetation identified in the remote sensing data. This could prevent a spatial mismatch of remote sensing and field data.

Areas with homogeneous vegetation composition are particularly suitable and can be used as labels for medium-resolution satellite imagery. This approach would allow for creating time series of spectral signatures for different plant species. Ideally, several areas per species would be available to account for variability adequately.

5.4.2 Addressing endmember variability

The challenges of spectral, spatial, and temporal variation of endmembers in LSMA were discussed in chapter 5.2.3.

The Multiple Endmember Spectral Mixture Analysis (MESMA) could help address these challenges (Somers et al., 2011). With MESMA, groups of endmembers are formed that are assigned to the same target. In an iterative process, the highest match between endmember and spectrum is found. MESMA has been used successfully for monitoring shrub vegetation (Lippitt et al., 2018). Defining multiple endmembers per target would allow accounting for phenological and physiological variability. However, MESMA is not currently implemented in the GEE. The added value of MESMA for saxaul mapping could be determined by testing MESMA outside the GEE.

5.4.3 RTM inversion

In this thesis, vegetation spectra were simulated with an RTM using plant traits from the literature. With sufficient availability of field data, the RTM parametrisation could be tuned to the local conditions, e.g., with hybrid inversion.

First, a larger number of vegetation spectra is simulated, e.g., 1'000. Second, a machine learning regression algorithm (MLRA) is trained with the simulated spectra, learning the relationship between plant traits and spectra (Verrelst et al., 2019). Third, the MRLA is used to determine the plant traits of the field data. This opens up two new possibilities. First, saxaul-specific vegetation spectra can be simulated, which could be used as endmembers for MESMA. Second, the calculation of additional variables such as biomass becomes possible.

Gaussian Processes regression (GPR) is one of the most accurate regression methods for hybrid inversion (Verrelst et al., 2015, 2013). GPR is not currently implemented in the GEE but Pipia et al. (2021) have shown that it is possible to run a pre-trained GPR model in GEE. Until the development of GPR models in GEE eventually becomes possible the proposed RTM inversion for the GGB SPA could be tested locally.

5.4.4 Sentinel-1 data

There are two types of S-1 data: the Single-look Complex (SLC) product providing amplitude and phase information, and the Ground Range Detected (GRD) product providing intensity (ESA, 2012). Only the GRD product is available in the GEE.

5 Discussion

The phase information of the S-1 SLC product can be used for coherence change detection (CCD), through which subtle changes in the Earth's surface become detectable, even at the sub-pixel level (Ullmann et al., 2019). The volume scattering of vegetation canopies reduces coherence (Ouaadi et al., 2020) - a fact that could be used for detecting vegetation in the GGB SPA. For testing purposes, S-1 SLC data could be processed locally and uploaded to the GEE.

6 Conclusion

Summary

This methodological exploratory thesis aimed to find a method to accurately estimate the density of saxaul forest with Sentinel-1 and Sentinel-2 data. The density estimates of the following methods were compared: two Random Forest regression models, which differed in the origin of the labels and were trained with different variable types, and LSMA of Sentinel-2 data with a combination of algorithm-extracted and RTM-simulated endmembers. Subsequently, an attempt was made to distinguish plant species in two oases complexes using estimated density and additional variables. I estimated the possible spatial distribution of saxaul forests by classifying the Great Gobi B Strictly Protected Area (GGB SPA) according to dominant vegetation community. For training purposes, different groups of variables were used to determine their influence on the model accuracy.

Answers to research questions

- 1) How can the saxaul density be estimated most accurately on the pixel level?

The most spatially consistent estimation of vegetation density for two validation plots near the Khonin us ranger station was achieved with LSMA of Sentinel-2 data, for which a combination of algorithm-extracted soil and RTM-simulated vegetation endmembers was used ($R^2 = 0.29$ and 0.25 , RMSE = 10 and 4% for the larger and smaller validation plot, respectively). The soil endmembers corresponded to selected spectra identified as endmembers using MVC-NMF. The vegetation endmembers were simulated with PROSPECT-4. The input parameters were determined using literature and the TRY Plant Trait Database. In the case of one of the Random Forest regressor models, the accuracy was higher for the larger validation plot close to the training plot ($R^2 = 0.34$, RMSE = 7%). However, its applicability was limited to the immediate vicinity of the training plot. If the soil background changed, as in the case of the smaller validation plot, the model did not produce reliable estimates ($R^2 = 0.03$, RMSE = 25%).

Experimental tests in two oasis complexes showed that the distinction of plant species with the estimated density and MSAVI(-derived) variables was not possible. Therefore, the proposed method allows the determination of vegetation density for the analyzed area near the Khonin us ranger station, but not the determination of saxaul forest density.

6 Conclusion

- 2) How accurately can the vegetation community distribution be mapped using moderate-resolution satellite remote sensing data?

I tested different combinations of variable groups to replicate the vegetation community mapping of Chuluunkhuyag et al. (2021) with annual composites of Sentinel-2 data for 2019 and 2020. For the vegetation community containing saxaul, PA and UA were 0.74 and 0.64, respectively (average values over both years). The spatial extent of saxaul forests in the GGB SPA was estimated at 8'141 and 8'323 km² for 2019 and 2020, respectively. A statistical comparison with the mapping of Chuluunkhuyag et al. (2021) was not possible, as no accuracy metrics were available. However, according to visual assessment, the obtained maps are consistent with the reference mapping.

The most important variables for mapping the possible spatial distribution of saxaul forests included elevation and temporal variables, followed by textural and SAR variables. This would indicate an added value of combining Sentinel-1 and Sentinel-2 data. However, these results should be interpreted with caution, as the input data were subject to multicollinearity.

Recommendations for future research

For further development of the products, the generation of additional field data is necessary. I suggest that for areas of interest drone flights take place or high-resolution satellite imagery is ordered. Subsequently, the vegetation on the images would be identified by a field survey. Ideally, endmembers could be isolated for Multiple Endmember Spectral Mixture Analysis (MESMA) to account for endmember variability. An attempt could also be made to determine the plant traits of saxaul using the hybrid inversion of PROSPECT-4. Based on this, the calculation of additional products such as biomass would be conceivable.

Supplementary materials A: Comparison of cloud removal algorithms

I randomly selected 20 S-2 images regardless of their cloudy pixel percentage between April and October 2020 to compare the performance of two methods for cloud removal: Sen2Cor and s2cloudless.

In the case of Sen2Cor, I worked with the SCL bit mask. Only vegetation, bare soil, water, and snow were kept. Snow was not masked out because this option does not exist in s2cloudless and would have influenced the comparison.

S2cloudless is a machine-learning single-scene cloud detector based on the Light Gradient Boosting Machine (LightGBM) algorithm (Zupanc, 2017). The minimum of the bimodal distribution of cloud probability is described as a reasonable threshold (Braaten et al., 2020). To determine a meaningful threshold to be applied to multiple images, 20 additional images were randomly selected, but with a cloudy pixel percentage between 60 and 80% to avoid cloud-free and heavily clouded images. Despite this condition, two images were cloud-free. The average optimal threshold was 49.94%, the median 51% (Table 15).

I set the cloud probability threshold to 51%, the near-infrared reflectance threshold (NIR_DRK_THRESH) to 0.1, and the maximum distance to search for clouds (CLD_PRJ_DIST) to 5 km to compare the performance with Sen2Cor.

Table 16 shows the results of the performance comparison.

The performance was similar but differed by cloud cover type. In the EO Browser (<https://apps.sentinel-hub.com/eo-browser/>), the type of cloud cover was determined visually for all images during the period April to October 2020. In 27 cases cumulus clouds were dominant, in 50 cases the coverage was mixed. Therefore, our final decision was in favor of Sen2Cor.

Table 15: Determination of s2cloudless threshold. 20 Sentinel-2 images with a cloudy pixel percentage between 60 and 80% were analyzed. The optimal threshold for s2cloudless was assumed to correspond to the absolute low of the bimodal distribution of the image pixel's cloud probability.

Image ID	Cloudy pixel percentage	Clouds present?	Absolute low of bimodal distribution
20200405T045651_20200405T045718_T46TCR	76.22	yes	38
20200412T044701_20200412T045530_T46TCQ	76.21	yes	54
20200427T044659_20200427T044735_T46TCR	79.36	no	
20200427T044659_20200427T044735_T46TDQ	69.73	no	
20200509T043711_20200509T044259_T46TFR	69.59	yes	64
20200512T044701_20200512T045536_T46TDR	73.64	yes	85
20200512T044701_20200512T045536_T46TER	69.40	yes	36
20200529T043711_20200529T043707_T46TDR	61.08	yes	40
20200621T044711_20200621T045324_T46TER	76.45	yes	45
20200713T043659_20200713T043702_T46TDQ	63.64	yes	51
20200713T043659_20200713T043702_T46TER	63.23	yes	52
20200815T044709_20200815T044920_T45TYL	70.99	yes	51
20200815T044709_20200815T044920_T46TCR	78.75	yes	48
20200827T043711_20200827T044502_T46TDQ	68.40	yes	51
20200902T045701_20200902T050522_T46TCR	79.20	yes	53
20200916T043711_20200916T044458_T46TDQ	61.45	yes	36
20200929T044711_20200929T045454_T46TER	78.02	yes	58
20201009T044711_20201009T044713_T46TDR	75.25	yes	45
20201009T044711_20201009T045556_T45TYL	63.26	yes	28
20201012T045731_20201012T045732_T45TYL	61.61	yes	64

Table 16: Overview of the performances of Sen2Cor and s2cloudless. 20 Sentinel-2 images without cloud pixel percentage restrictions were analyzed. The best performer (1 = Sen2Cor, 2 = s2cloudless, 3 = draw) was determined by visual assessment. The threshold for s2cloudless was set to 51%.

Image ID	Cloudy pixel percentage	Best performer	Cloud type
20200623T043709_20200623T043703_T46TDQ	0.69		
20200420T045649_20200420T045651_T46TCQ	7.78	1	Mixed cloud cover
20200514T043659_20200514T043659_T46TDR	6.00	3	Cumulus
20200509T043711_20200509T044259_T46TDR	76.38	3	Mixed cloud cover
20200924T044659_20200924T045505_T46TCQ	0.26		
20200723T043659_20200723T043734_T46TER	89.43	1	Mixed cloud cover
20200402T044701_20200402T045415_T46TCQ	84.45		
20200724T045701_20200724T050437_T46TCQ	60.94	1	Mixed cloud cover
20201004T044709_20201004T044703_T46TCQ	0.07		
20200726T044659_20200726T044734_T45TYL	0.57	2	Cumulus
20200623T043709_20200623T043703_T46TFR	5.93	2	Cumulus
20200731T044711_20200731T045436_T46TCQ	2.57	2	Cumulus
20200507T044659_20200507T044657_T46TCR	2.70	2	Cumulus
20200623T043709_20200623T043703_T46TEQ	0.69		
20200629T045659_20200629T045659_T46TCR	2.27		
20200810T044711_20200810T045542_T46TEQ	10.17	1	Mixed cloud cover
20200723T043659_20200723T043734_T46TEQ	86.48	3	Almost entirely cloudy
20200417T044659_20200417T045549_T46TEQ	97.04	2	Almost entirely cloudy
20200805T044709_20200805T044703_T46TDR	17.78	2	Cumulus
20200420T045649_20200420T045651_T46TDR	24.45	1	Mixed cloud cover

Supplementary materials B: Parameter settings and model architectures of usability assessment of field data

Table 17: Parametrisation of the Random Forest model used for forest inventory usability assessment. I used the Random Forest regressor implemented in the Scikit-learn python library.

Parameter	Value
N_estimators	1000
min_samples_split	10
min_samples_leaf	10
max_features	'sqrt' (square root of number of input features)
max_depth	20
bootstrap	True

Table 18: Architecture of the 1-D Convolutional Neural Network model used for forest inventory usability assessment. I used a sequential model implemented in the Keras python library running on top of TensorFlow.

1D-CNN architecture
<pre>model = Sequential() model.add(Conv1D(32, 2, activation="relu", input_shape=(10, 1))) model.add(MaxPooling1D(pool_size=2)) model.add(Flatten()) model.add(Dense(64, activation="relu")) model.add(Dense(1)) model.compile(loss="mse", optimizer="adam")</pre>

Supplementary materials C: Algorithm-extracted endmember signatures

The pixel purity index (PPI), after dimensionality reduction and noise whitening, determines the most extreme pixels when projecting the data onto random unit vectors (Boardman et al., 1995). With N-finder (N-FINDR), the endmembers spectra are assumed to represent the simplex, a convex geometric body enveloping the n-dimensional feature space (Winter, 1999). In an iterative process, each pixel is sampled as each possible endmember until the volume of the simplex is maximised (Winter, 2004). With vertex component analysis (VCA), the endmembers are vertices of this simplex, and each endmember corresponds to the extreme of a projection of the data (Nascimento and Dias, 2005). For each endmember, the data are reprojected perpendicular to the previously spanned subspace until the defined number of endmembers is found. Minimum volume constrained non-negative matrix factorisation (MVC-NMF) combines the most accurate approximation of endmembers with minimisation of simplex volume (Miao and Qi, 2007). NMF forms non-negative vectors that approximate the input data with a cost function. If all pixels are mixtures, then the endmembers do not correspond to the vertices of the simplex but must lie outside. The MVC keeps the volume of the simplex as small as possible, which makes the algorithm applicable to a larger number of endmembers and less susceptible to noise.

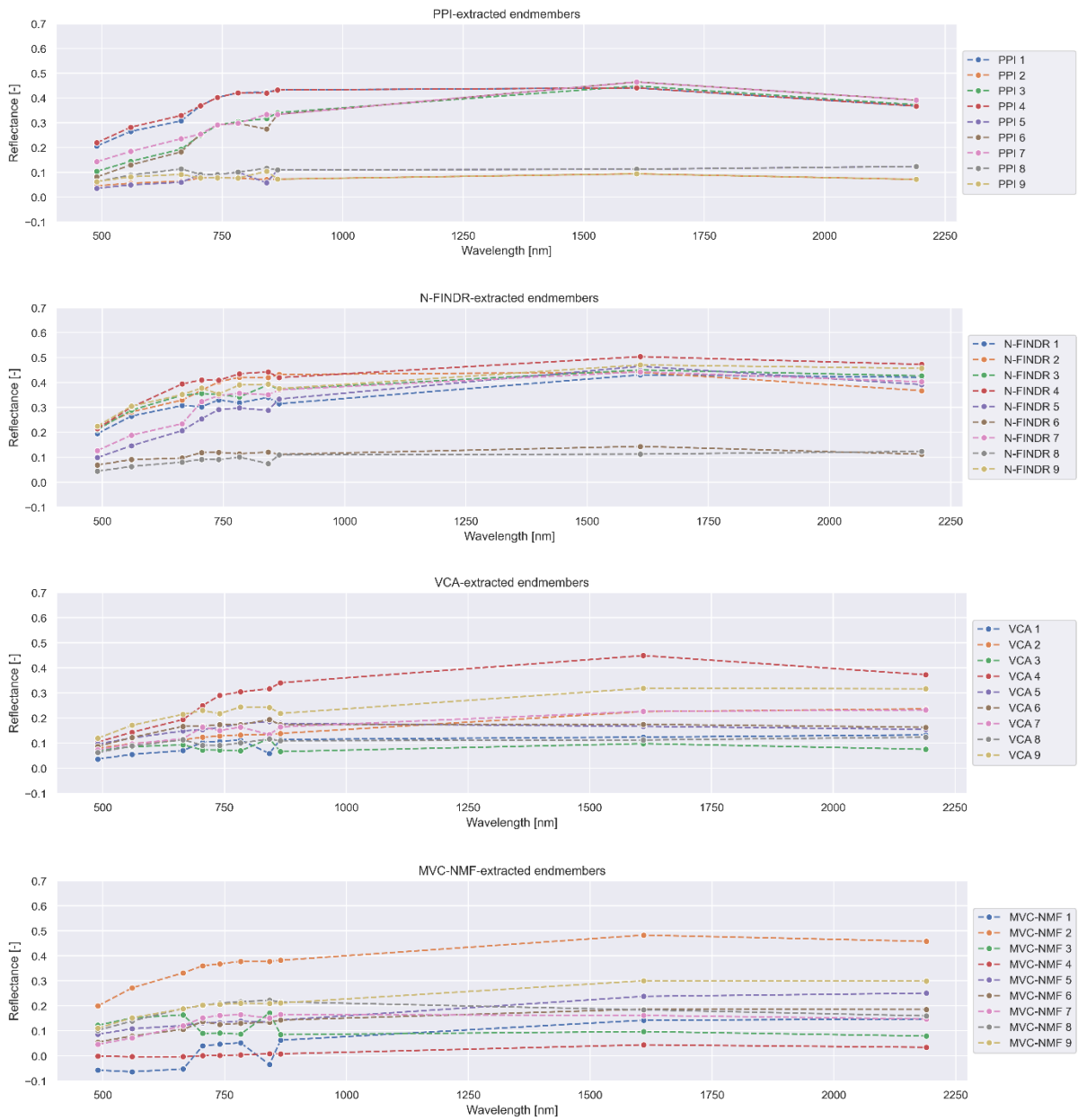


Figure 38: Algorithm-extracted endmember signatures. I used built-in and custom functions to extract the endmembers of the Sentinel-2 image in MATLAB 2021a with the following methods: pixel purity index, N-Finder, vertex component analysis, and minimum volume constrained non-negative matrix factorisation (from top to bottom). The number of endmembers to be extracted was previously determined using the Noise-Whitened Harsanyi-Farrand-Chang method.

Supplementary materials D: Confusion matrices for 2019 and 2020

Table 19: Confusion matrix of Takhi us 2019. The rows correspond to the vegetation community IDs found in the oasis (cf. Table 8). The columns correspond to the K-means clusters. 1'000 points were sampled per vegetation community. The best fit indicator indicates the largest proportion of a cluster that corresponded to a single ID.

↓ ID Clusters →	1	2	3	4	5	6	7	8
2	18	712	0	1	1	268	0	0
4	0	0	900	1	2	0	87	10
5	0	0	144	57	8	0	520	271
6	36	12	556	6	11	133	218	28
9	0	0	141	131	9	0	376	343
10	0	0	455	120	6	0	275	144
11	0	0	427	12	0	0	423	138
12	390	44	2	16	380	118	10	40
Best Fit [%]	87.84	92.71	34.29	38.08	91.13	51.64	27.24	35.22

Table 20: Confusion matrix of Takhi us 2020. The rows correspond to the vegetation community IDs found in the oasis (cf. Table 8). The columns correspond to the K-means clusters. 1'000 points were sampled per vegetation community. The best fit indicator indicates the largest proportion of a cluster that corresponded to a single ID.

↓ ID Clusters →	1	2	3	4	5	6	7	8
2	724	0	0	265	11	0	0	0
4	0	122	5	0	0	9	793	71
5	0	187	462	0	7	0	31	313
6	5	125	7	71	22	167	560	43
9	0	245	269	0	6	39	171	270
10	0	154	114	0	5	246	383	98
11	0	179	52	0	0	73	417	279
12	37	3	191	185	529	2	2	51
Best Fit [%]	94.52	24.14	42.00	50.86	91.21	45.90	33.64	27.82

Table 21: Confusion matrix of Khonin us 2019. The rows correspond to the vegetation community IDs found in the oasis (cf. Table 8). The columns correspond to the K-means clusters. 1'000 points were sampled per vegetation community. The best fit indicator indicates the largest proportion of a cluster that corresponded to a single ID.

↓ ID Clusters →	1	2	3	4	5	6	7	8	9	10
2	0	0	1	0	0	6	102	0	0	891
3	124	6	0	302	233	0	0	272	63	0
4	144	0	0	303	259	0	0	250	44	0
5	82	356	1	1	36	3	0	3	518	0
6	102	5	2	338	145	0	0	390	18	0
7	347	85	12	59	136	8	3	23	327	0
9	186	75	8	253	207	0	0	90	181	0
10	82	8	1	398	120	0	0	362	29	0
11	53	0	0	411	113	0	0	401	22	0
12	16	58	372	4	20	322	122	20	30	36
Best Fit [%]	30.55	60.03	93.70	19.86	20.41	94.99	53.74	22.14	42.05	96.12

Table 22: Confusion matrix of Khonin us 2020. The rows correspond to the vegetation community IDs found in the oasis (cf. Table 8). The columns correspond to the K-means clusters. 1'000 points were sampled per vegetation community. The best fit indicator indicates the largest proportion of a cluster that corresponded to a single ID.

↓ ID Clusters →	1	2	3	4	5	6	7	8	9	10
2	0	0	98	896	0	0	0	6	0	0
3	263	11	0	0	60	177	222	3	232	32
4	211	24	0	0	218	106	183	0	71	187
5	7	614	0	0	59	248	1	4	4	63
6	198	8	0	0	79	37	398	0	128	152
7	39	519	6	0	83	105	18	2	2	226
9	217	131	0	0	112	120	130	1	62	227
10	432	12	0	0	14	23	290	0	73	156
11	271	6	0	0	23	23	372	0	67	238
12	31	111	197	43	60	143	8	355	21	31
Best Fit [%]	25.88	42.76	65.45	95.42	30.79	25.25	24.54	95.69	35.15	18.14

Supplementary materials E: Feature combinations and variable importance of land cover and vegetation community mapping

Table 23: Feature importance of all variable combinations for land cover mapping. For all combinations (cf. Table 11), the feature importance expressed through the mean decrease Gini is listed.

Variable	Original		All		All – SAR		All – Corr		All - Both	
	2019	2020	2019	2020	2019	2020	2019	2020	2019	2020
Aerosol	306	307	93	100	103	103	120	126	141	143
Aspect	290	277	106	101	115	108	132	131	149	149
Blue	298	291	93	97	102	102	118	125	129	135
Blue_asm			111	111	111	112	131	136	151	146
Blue_contrast			101	122	105	121	138	153	155	172
Blue_corr			121	120	131	131	138	149	164	170
Blue_diss			103	117	113	124				
Blue_ent			114	111	126	129	142	130	149	153
Blue_idm			109	113	121	123	142	143	150	154
Blue_savg			96	97	103	110				
Blue_var			102	113	115	125	132	142	156	159
Brightness	300	325	89	94	94	99				
Brightness Std.			116	113	119	116				
Elevation	398	392	156	177	166	179	187	205	210	215
Green	291	286	91	92	97	97	109	111	127	134
Greenness	367	365	100	116	108	121	140	150	154	166
Greenness Std.			123	123	132	133				
MSAVI Std.			158	145	165	150	216	193	227	207
NDVI Std.			140	134	142	139				
NIR	325	337	89	97	92	101	115	126	126	145
RE1			80	88	94	93	103	111	127	132
RE2			85	96	90	94	103	110	117	127
RE3			92	102	90	104	107	118	127	139
RE4			96	105	98	104	114	124	131	142
Red	286	293	82	92	91	99	112	111	125	131
Slope	330	303	108	114	120	123	144	144	155	160
SWIR1	290	290	95	98	95	99	117	112	136	135
SWIR2	300	303	99	101	102	108	125	127	142	148
VH			107	107			129	132		
VV			108	109			132	139		
Wetness	304	304	100	98	111	110	122	123	149	152
Wetness Std.			130	126	141	135	182	165	195	181

Table 24: Feature importance of all variable combinations for vegetation community mapping. For all combinations (cf. Table 11), the feature importance expressed through the mean decrease Gini is listed.

Variable	Original		All		All – SAR		All – Corr		All - Both	
	2019	2020	2019	2020	2019	2020	2019	2020	2019	2020
Aerosol	436	445	147	153	156	162	175	187	206	217
Aspect	416	408	159	163	171	173	185	196	214	226
Blue	431	428	130	131	144	146	169	174	205	205
Blue_asm			153	156	165	171	190	198	213	218
Blue_contrast			155	167	167	177	192	206	213	232
Blue_corr			169	172	185	200	208	221	242	257
Blue_diss			161	167	164	176				
Blue_ent			150	147	165	172	187	188	213	214
Blue_idm			154	161	157	169	183	186	206	220
Blue_savg			150	143	150	158				
Blue_var			162	175	171	178	201	210	224	231
Brightness	418	424	122	129	135	145				
Brightness Std.			178	172	183	179				
Elevation	557	570	223	245	232	257	287	300	301	326
Green	425	421	128	131	141	148	161	161	181	190
Greenness	492	498	148	160	154	174	192	204	211	225
Greenness Std.			176	188	184	190				
MSAVI Std.			200	191	220	213	270	271	281	273
NDVI Std.			188	184	201	192				
NIR	466	470	130	135	142	146	171	175	193	208
RE1			128	135	127	137	154	153	182	201
RE2			130	130	137	143	155	155	182	195
RE3			125	134	139	145	156	161	177	194
RE4			133	137	141	148	170	173	186	194
Red	433	421	123	131	139	147	167	166	193	191
Slope	446	431	150	155	174	173	187	194	227	234
SWIR1	433	421	139	138	141	149	163	167	201	209
SWIR2	451	441	142	150	158	164	178	178	203	215
VH			173	176			201	217		
VV			161	175			196	223		
Wetness	431	434	148	145	162	159	187	180	204	208
Wetness Std.			197	179	208	195	254	238	284	253

Supplementary materials F: Correlation matrices of input data for land cover and community mapping 2019

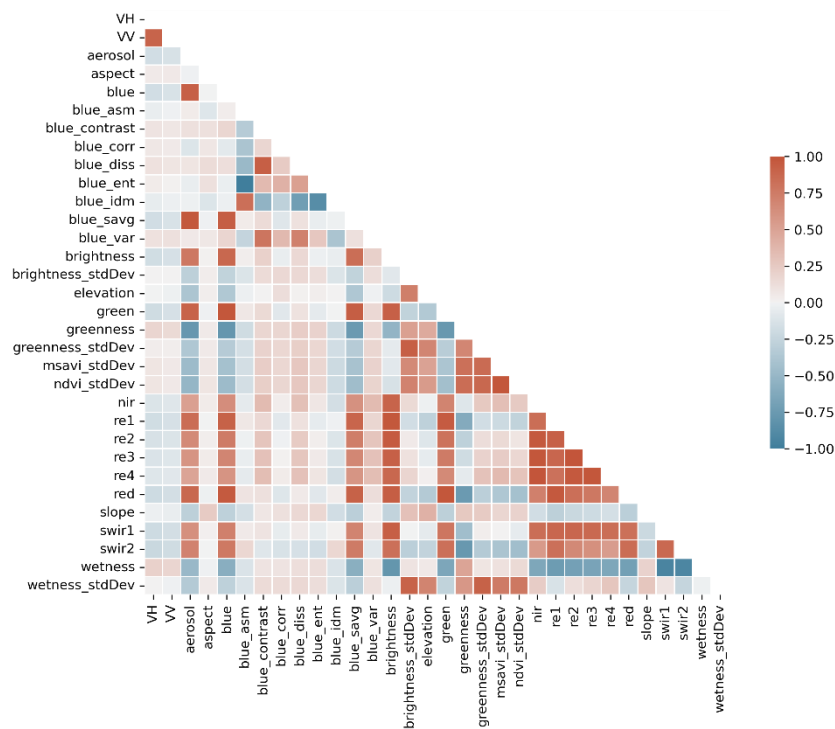


Figure 39: Correlation matrix of input variables for land cover and community mapping 2019. The correlation is expressed through the Pearson correlation coefficient.

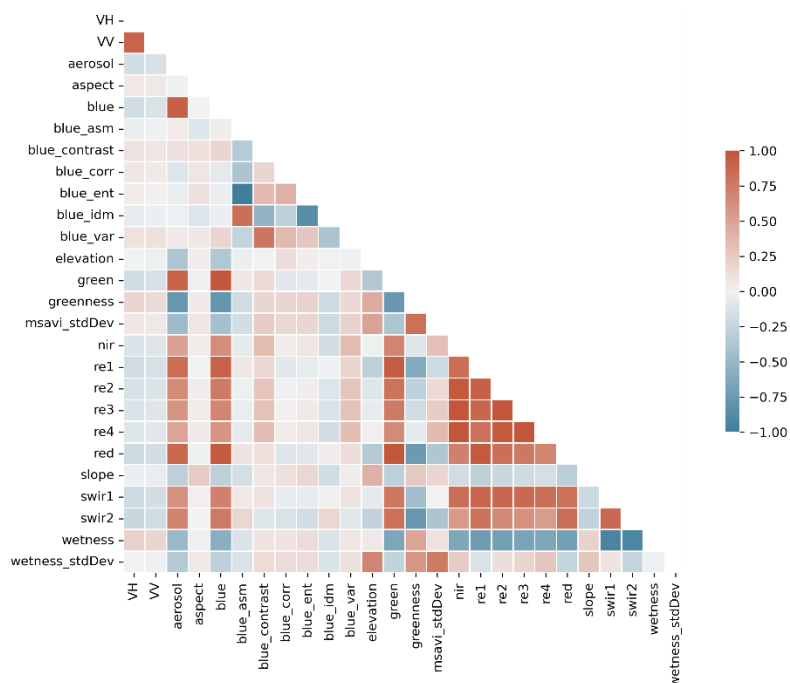


Figure 40: Correlation matrix of input variables for land cover and community mapping 2019 after removing selected correlated variables. The correlation is expressed through the Pearson correlation coefficient.

Supplementary materials G: Spatial autocorrelation

Training stage

I repeated the training of the two RF regressor models using three training subsets with reduced SAC determined using Moran's I (Moran, 1948) (Table 25). Each subset consisted of 300 samples with a minimum distance of 50 m between them. The same variable combinations were used as in the original implementation. For each model and combination, a 3-fold random subsampling was performed.

The use of training subsets influenced the mean model performances (Figure 41). The best trade-off would no longer necessarily have been the R13 combination. The performances were volatile, varying considerably between the individual runs (results not shown). However, the metrics were generally lower than for the original implementation, which is consistent with the results of (Ploton et al., 2020). Therefore, I assume that the performances of RF-RF and RF-LSMA in the original implementation were overestimated because SAC was not considered.

Table 25: Presence of spatial autocorrelation in training sets for machine learning models. The table shows the outputs of the ArcGIS Spatial Autocorrelation (Global Moran's I) function for the training sets of the RF-RF and RF-LSMA models. The training sets included either all Sentinel-2 pixels, randomly selected 50% of the pixels, or 300 randomly selected pixels each with a minimum distance of 50 m between the points.

Set	Moran's Index	Expected Index	Variance	z-score	p-value	Confidence level [%]
RF-RF All Cells	0.3895	-0.0001	0	67.8324	0	>99
RF-RF 50% Training	0.2853	-0.0001	0	58.3566	0	>99
RF-RF Subset 1	0.0141	-0.0033	0.0019	0.404	0.6862	<90
RF-RF Subset 2	0.0634	-0.0033	0.0019	0.0019	0.1229	<90
RF-RF Subset 3	0.1218	-0.0033	0.002	2.7641	0.0057	>99
RF-LSMA All Cells	0.5762	-0.0001	0	101.0962	0	>99
RF-LSMA 50% Training	0.4627	-0.0001	0	90.3692	0	>99
RF-LSMA Subset 1	0.2699	-0.0033	0.0021	5.9213	0	>99
RF-LSMA Subset 2	0.2393	-0.0033	0.002	5.422	0	>99
RF-LSMA Subset 3	0.3586	-0.0033	0.0022	7.7544	0	>99

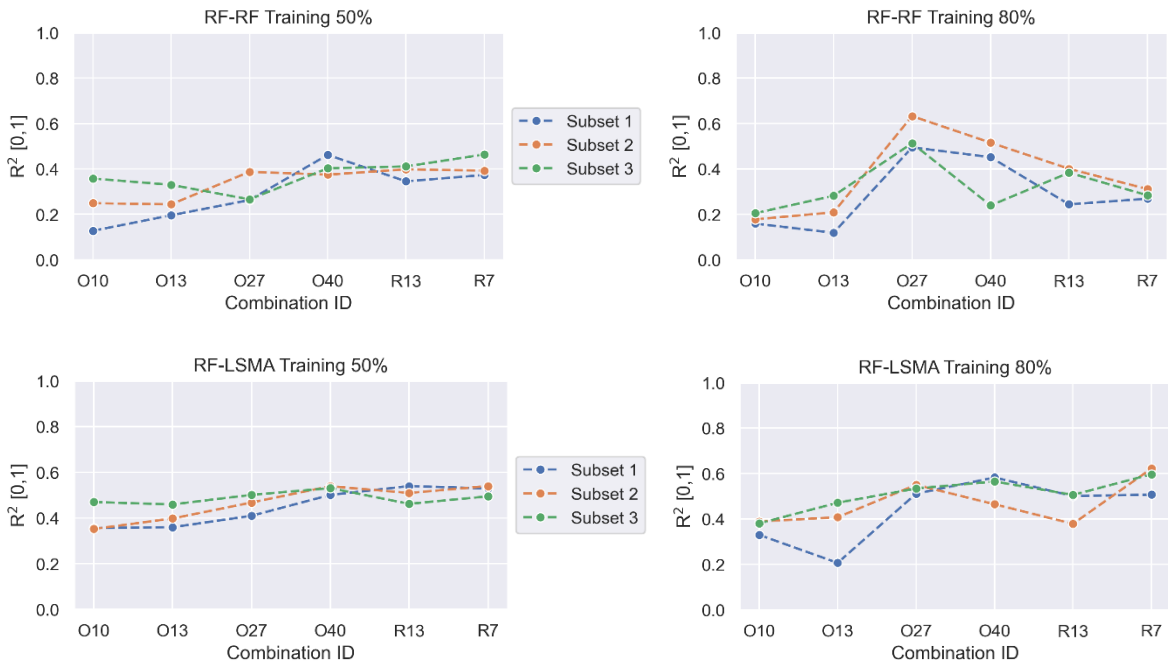


Figure 41: RF-RF and RF-LSMA model performances with different training subsets and training set size. The coefficient of determination corresponds to the average of three runs per model, training subset, and training set size. The combination IDs are listed in Table 5. The training subsets are listed in Table 25.

Validation stage

The validation was repeated for the larger plot with three subsets of 200 samples with a minimum distance of 50 m between them (Table 26). The results were different for each subset, which is probably due to the low number of samples. Nevertheless, the metrics for RF-RF were highest, followed by S2-LSMA and RF-LSMA (Table 27). This procedure was not applied to the smaller validation plot due to its small area.

Table 26: Presence of spatial autocorrelation in the larger validation plot. The table shows the outputs of the ArcGIS Spatial Autocorrelation (Global Moran's I) function for the validation sets of the larger validation plot. The validation sets included either all Sentinel-2 pixels, or 200 randomly selected pixels each with a minimum distance of 50 m between the points.

Set	Moran's Index	Expected Index	Variance	z-score	p-value	Confidence level [%]
All Cells	0.3589	-0.0001	0.0001	45.465	0	>99
Subset 1	0.0968	-0.005	0.0033	1.7672	0.0772	>90
Subset 2	0.0766	-0.005	0.0037	1.3387	0.1807	<90
Subset 3	-0.0318	-0.005	0.003	-	0.6256	<90

Table 27: Validation results of the compared saxaul density estimates with different validation sets. The validation sets for the larger validation plot are listed in Table 26.

Validation plot large	RF-RF	RF-LSMA	S2-LSMA
R ² All Cells	0.34	0.26	0.29
R ² Subset 1	0.22	0.14	0.21
R ² Subset 2	0.54	0.38	0.46
R ² Subset 3	0.41	0.33	0.32
RMSE All Cells	0.07	0.11	0.10
RMSE Subset 1	0.07	0.11	0.10
RMSE Subset 2	0.06	0.11	0.10
RMSE Subset 3	0.06	0.11	0.09

Acknowledgments

I would like to thank my supervisor, Christian Rossi, and my co-supervisors, Mathias Kneubühler, Petra Kaczensky, and Marius Rüetschi, for their exceptional support during the past year and for allowing me to get to know the fascinating ecosystem of the Dzungarian Gobi.

Extraordinary thanks go to all people, without whose tireless efforts for field data last summer this thesis would not have been possible: Ganbaatar Oyunsaikhan, Dalaitseren Sukhbaatar, Lhachin Oinbayer, Zentger Baast, Pognogor Tserentogtokh, Janchiv Tugsbaatar, Galbadrakh Batsaikhan, Tomor Lhagva, Choijiljav Tserendorj, Urtnasan Duurenbayar, and all other people who assisted in the collection of the data.

Special thanks go to Batsukh Jamiyandorj, who organised the access to the forest inventory data and always helped me with language and administrative issues, and Oyundari Chuluunkhuyag for providing and explaining me her field data.

At an earlier stage, a SkySat Pansharpened Multispectral Scene product was used. At this point, many thanks to Rolf Richter for his explanations regarding the atmospheric correction of such an image.

Finally, my deepest thanks go to all the people who made it possible for me to complete my studies and who have always supported me in my private and academic life.

References

- Amani, M., Mahdavi, S., Afshar, M., Brisco, B., Huang, W., Mirzadeh, S.M.J., White, L., Banks, S., Montgomery, J., Hopkinson, C., 2019. Canadian wetland inventory using Google Earth Engine: The first map and preliminary results. *Remote Sens.* 11, 1–20. <https://doi.org/10.3390/RS11070842>
- Annala, L., Honkavaara, E., Tuominen, S., Pölönen, I., 2020. Chlorophyll concentration retrieval by training convolutional neural network for stochastic model of leaf optical properties (SLOP) inversion. *Remote Sens.* 12, 283. <https://doi.org/10.3390/rs12020283>
- Arruda, V.L.S., Piontekowski, V.J., Alencar, A., Pereira, R.S., Matricardi, E.A.T., 2021. An alternative approach for mapping burn scars using Landsat imagery, Google Earth Engine, and Deep Learning in the Brazilian Savanna. *Remote Sens. Appl. Soc. Environ.* 22, 100472. <https://doi.org/10.1016/j.rsase.2021.100472>
- Arthur, D., Vassilvitskii, S., 2007. K-means++: The advantages of careful seeding, in: *Proceedings of the Annual ACM-SIAM Symposium on Discrete Algorithms*. pp. 1027–1035.
- Aschbacher, J., 2017. ESA's earth observation strategy and Copernicus, in: *Satellite Earth Observations and Their Impact on Society and Policy*. Springer Singapore, pp. 81–86. https://doi.org/10.1007/978-981-10-3713-9_5
- Batchuluun, B., Wunderlich, J., Schmitt, M., 2020. Diversity of beetles (Coleoptera) in natural and planted saxaul forests (haloxylon ammodendron) in the south gobi desert, Mongolia. *Zookeys* 2020, 59–70. <https://doi.org/10.3897/zookeys.1000.56856>
- Batsaikhan, B., Lkhamjav, O., Batsaikhan, G., Batsaikhan, N., Norovsuren, B., 2020. Carbon stock estimation using remote sensing data and field measurement in haloxylon ammodendron dominant winter cold desert region of mongolia. *ISPRS Ann. Photogramm. Remote Sens. Spat. Inf. Sci.* 5, 9–17. <https://doi.org/10.5194/isprs-Annals-V-3-2020-9-2020>
- Behnamian, A., Banks, S., White, L., Millard, K., Pouliot, D., Pasher, J., Duffe, J., 2019. Dimensionality Reduction in the Presence of Highly Correlated Variables for Random Forests: Wetland Case Study, in: *International Geoscience and Remote Sensing Symposium (IGARSS)*. Institute of Electrical and Electronics Engineers Inc., pp. 9839–

9842. <https://doi.org/10.1109/IGARSS.2019.8898308>

Belgiu, M., Csillik, O., 2018. Sentinel-2 cropland mapping using pixel-based and object-based time-weighted dynamic time warping analysis. *Remote Sens. Environ.* 204, 509–523. <https://doi.org/10.1016/j.rse.2017.10.005>

Belgiu, M., Drăgu, L., 2016. Random forest in remote sensing: A review of applications and future directions. *ISPRS J. Photogramm. Remote Sens.* <https://doi.org/10.1016/j.isprsjprs.2016.01.011>

Berrar, D., 2018. Cross-validation, in: *Encyclopedia of Bioinformatics and Computational Biology: ABC of Bioinformatics*. Academic Press, pp. 542–545. <https://doi.org/10.1016/B978-0-12-809633-8.20349-X>

Braaten, J., Schwehr, K., Ilyushchenko, S., 2020. More accurate and flexible cloud masking for Sentinel-2 images [WWW Document]. URL <https://medium.com/google-earth/more-accurate-and-flexible-cloud-masking-for-sentinel-2-images-766897a9ba5f> (accessed 10.4.21).

Breiman, L., 2001. Random forests. *Mach. Learn.* 45, 5–32. <https://doi.org/10.1023/A:1010933404324>

Burnik Šturm, M., Ganbaatar, O., Voigt, C.C., Kaczensky, P., 2017. Sequential stable isotope analysis reveals differences in dietary history of three sympatric equid species in the Mongolian Gobi. *J. Appl. Ecol.* 54, 1110–1119. <https://doi.org/10.1111/1365-2664.12825>

Campos-Taberner, M., Moreno-Martínez, Á., García-Haro, F.J., Camps-Valls, G., Robinson, N.P., Kattge, J., Running, S.W., 2018. Global estimation of biophysical variables from Google Earth Engine platform. *Remote Sens.* 10, 1–17. <https://doi.org/10.3390/rs10081167>

Carrasco, L., O’Neil, A.W., Daniel Morton, R., Rowland, C.S., 2019. Evaluating combinations of temporally aggregated Sentinel-1, Sentinel-2 and Landsat 8 for land cover mapping with Google Earth Engine. *Remote Sens.* 11, 288. <https://doi.org/10.3390/rs11030288>

CEOS, 2019. Analysis Ready Data For Land 1–10.

Chang, C.I., Du, Q., 2004. Estimation of number of spectrally distinct signal sources in hyperspectral imagery. *IEEE Trans. Geosci. Remote Sens.* 42, 608–619. <https://doi.org/10.1109/TGRS.2003.819189>

- Chen, R.C., Dewi, C., Huang, S.W., Caraka, R.E., 2020. Selecting critical features for data classification based on machine learning methods. *J. Big Data* 7, 1–26. <https://doi.org/10.1186/s40537-020-00327-4>
- Cheng, K., Wang, J., 2019. Forest type classification based on integrated spectral-spatial-temporal features and random forest algorithm-A case study in the Qinling Mountains. *Forests* 10, 559. <https://doi.org/10.3390/f10070559>
- Chierchia, G., El Gheche, M., Scarpa, G., Verdoliva, L., 2017. Multitemporal SAR Image Despeckling Based on Block-Matching and Collaborative Filtering. *IEEE Trans. Geosci. Remote Sens.* 55, 5467–5480. <https://doi.org/10.1109/TGRS.2017.2707806>
- Chollet, F., 2015. Keras. www.keras.io.
- Chuluunkhuyag, O., Chaoyan, L., Treiber, J., Batlai, O., von Wehrden, H., Feller, R., Wesche, K., 2021. Influence of altitude and longitude on vegetation in the dzungarian gobi and the south-western mongolian altai. *Phytocoenologia* 50, 339–369. <https://doi.org/10.1127/phyto/2021/0371>
- Claverie, M., Ju, J., Masek, J.G., Dungan, J.L., Vermote, E.F., Roger, J.C., Skakun, S. V., Justice, C., 2018. The Harmonized Landsat and Sentinel-2 surface reflectance data set. *Remote Sens. Environ.* 219, 145–161. <https://doi.org/10.1016/j.rse.2018.09.002>
- Coppin, P., Jonckheere, I., Nackaerts, K., Muys, B., Lambin, E., 2004. Digital change detection methods in ecosystem monitoring: A review. *Int. J. Remote Sens.* 25, 1565–1596. <https://doi.org/10.1080/0143116031000101675>
- Damm, A., Guanter, L., Verhoef, W., Schläpfer, D., Garbari, S., Schaepman, M.E., 2015. Impact of varying irradiance on vegetation indices and chlorophyll fluorescence derived from spectroscopy data. *Remote Sens. Environ.* 156, 202–215. <https://doi.org/10.1016/j.rse.2014.09.031>
- de Sá, N.C., Baratchi, M., Hauser, L.T., van Bodegom, P., 2021. Exploring the impact of noise on hybrid inversion of prosail RTM on sentinel-2 data. *Remote Sens.* 13, 1–20. <https://doi.org/10.3390/rs13040648>
- Enkhchimeg, T., Ser-Oddamba, B., Oyuntugs, A., Zoljargal, S., Narantugs, D., Batkhuu, N.-O., 2020. Population Demographic Characteristics of *Haloxylon ammodendron* (C.A. Mey.) Bunge ex Fenzl in Gobi Desert of Mongolia. *Mong. J. Biol. Sci.* 18, 29–40.

<https://doi.org/10.22353/mjbs.2020.18.13>

ESA, 2015. Sentinel-2 User Handbook Issue 1 Revision 2. Noordwijk.

ESA, 2012. Sentinel-1: ESA's radar observatory mission for GMES operational services, ESA Special Publication.

ESRI Inc., 2021. ArcGIS Pro 2.8.3. <https://www.esri.com/en-us/arcgis/products/arcgis-pro/overview>.

FAO, 2020. Global Forest Resources Assessment 2020 Report Mongolia. Rome.

FAO, 2014. Global Forest Resources Assessment 2015 Country Report Mongolia. Rome.

Farr, T.G., Rosen, P.A., Caro, E., Crippen, R., Duren, R., Hensley, S., Kobrick, M., Paller, M., Rodriguez, E., Roth, L., Seal, D., Shaffer, S., Shimada, J., Umland, J., Werner, M., Oskin, M., Burbank, D., Alsdorf, D.E., 2007. The shuttle radar topography mission. *Rev. Geophys.* 45, 2004. <https://doi.org/10.1029/2005RG000183>

Filipponi, F., 2019. Sentinel-1 GRD Preprocessing Workflow, in: *Proceedings 2019*, Vol. 18, Page 11. Multidisciplinary Digital Publishing Institute, p. 11. <https://doi.org/10.3390/ecrs-3-06201>

Franch, B., Vermote, E., Skakun, S., Roger, J.C., Masek, J., Ju, J., Villaescusa-Nadal, J.L., Santamaria-Artigas, A., 2019. A method for Landsat and Sentinel 2 (HLS) BRDF normalization. *Remote Sens.* 11, 632. <https://doi.org/10.3390/rs11060632>

Frantz, D., Haß, E., Uhl, A., Stoffels, J., Hill, J., 2018. Improvement of the Fmask algorithm for Sentinel-2 images: Separating clouds from bright surfaces based on parallax effects. *Remote Sens. Environ.* 215, 471–481. <https://doi.org/10.1016/j.rse.2018.04.046>

Ganbaatar, O., Munkhchuluun, B., Tuguldur, E., Enkhmunkh, G., Sarsarbayar, E., 2019. A Management Plan for the Great Gobi B Strictly Protected Area. Period: 2019-2023. Ulan Baatar.

Gao, X., Gray, J., Cohrs, C.W., Cook, R., Albaugh, T.J., 2021. Longer greenup periods associated with greater wood volume growth in managed pine stands. *Agric. For. Meteorol.* 297, 108237. <https://doi.org/10.1016/j.agrformet.2020.108237>

Gascon, F., Bouzinac, C., Thépaut, O., Jung, M., Francesconi, B., Louis, J., Lonjou, V., Lafrance, B., Massera, S., Gaudel-Vacaresse, A., Languille, F., Alhammoud, B.,

- Viallefont, F., Pflug, B., Bieniarz, J., Clerc, S., Pessiot, L., Trémas, T., Cadau, E., De Bonis, R., Isola, C., Martimort, P., Fernandez, V., 2017. Copernicus Sentinel-2A calibration and products validation status. *Remote Sens.* 9, 584. <https://doi.org/10.3390/rs9060584>
- Gillies, S., 2019. Rasterio: geospatial raster I/O for Python programmers. <https://github.com/mapbox/rasterio>.
- Gislason, P.O., Benediktsson, J.A., Sveinsson, J.R., 2006. Random forests for land cover classification, in: *Pattern Recognition Letters*. North-Holland, pp. 294–300. <https://doi.org/10.1016/j.patrec.2005.08.011>
- Gorelick, N., Hancher, M., Dixon, M., Ilyushchenko, S., Thau, D., Moore, R., 2017. Google Earth Engine: Planetary-scale geospatial analysis for everyone. *Remote Sens. Environ.* 202, 18–27. <https://doi.org/10.1016/j.rse.2017.06.031>
- Government of Mongolia, 2018. Mongolia’s Forest Reference Level submission to the United Nations Framework Convention on Climate Change. Ulaanbaatar.
- Hansen, M.C., Potapov, P. V., Moore, R., Hancher, M., Turubanova, S.A., Tyukavina, A., Thau, D., Stehman, S. V., Goetz, S.J., Loveland, T.R., Kommareddy, A., Egorov, A., Chini, L., Justice, C.O., Townshend, J.R.G., 2013. High-resolution global maps of 21st-century forest cover change. *Science* (80-.). 342, 850–853. <https://doi.org/10.1126/science.1244693>
- Hansen, M.C., Stehman, S. V., Potapov, P. V., 2010. Quantification of global gross forest cover loss. *Proc. Natl. Acad. Sci. U. S. A.* 107, 8650–8655. <https://doi.org/10.1073/pnas.0912668107>
- Haralick, R.M., Dinstein, I., Shanmugam, K., 1973. Textural Features for Image Classification. *IEEE Trans. Syst. Man Cybern.* SMC-3, 610–621. <https://doi.org/10.1109/TSMC.1973.4309314>
- Heiner, M., Nyamsuren, B., Davaa, G., Yunden, B., Dash, Z., Dorjgotov, A., Evans, J., von Wehrden, H., Kiesecker, J., 2015. Towards a National GIS Model to Map Terrestrial Ecosystems in Mongolia: A Pilot Study in the Gobi Desert Region, in: Fernandez-Gimenez, M.E., Baival, B., Fassnacht, S.R., Wilson, D. (Eds.), *Building Resilience of Mongolian Rangelands: A Trans-disciplinary Research Conference*. Nutag Action and

Research Institute, Ulaanbaatar, pp. 24–34.

- Huang, H., Chen, Y., Clinton, N., Wang, J., Wang, X., Liu, C., Gong, P., Yang, J., Bai, Y., Zheng, Y., Zhu, Z., 2017. Mapping major land cover dynamics in Beijing using all Landsat images in Google Earth Engine. *Remote Sens. Environ.* 202, 166–176. <https://doi.org/10.1016/j.rse.2017.02.021>
- Huang, Z., Zhang, X., Zheng, G., Gutterman, Y., 2003. Influence of light, temperature, salinity and storage on seed germination of *Haloxylon ammodendron*. *J. Arid Environ.* 55, 453–464. [https://doi.org/10.1016/S0140-1963\(02\)00294-X](https://doi.org/10.1016/S0140-1963(02)00294-X)
- Hunt, E.R., Cavigelli, M., Daughtry, C.S.T., McMurtrey, J.E., Walthall, C.L., 2005. Evaluation of digital photography from model aircraft for remote sensing of crop biomass and nitrogen status. *Precis. Agric.* 6, 359–378. <https://doi.org/10.1007/s11119-005-2324-5>
- Iversen, M., Brathen, K.A., Yoccoz, N.G., Ims, R.A., 2009. Predictors of plant phenology in a diverse high-latitude alpine landscape: Growth forms and topography. *J. Veg. Sci.* 20, 903–915. <https://doi.org/10.1111/j.1654-1103.2009.01088.x>
- Jacquemoud, S., Baret, F., 1990. PROSPECT: A model of leaf optical properties spectra. *Remote Sens. Environ.* 34, 75–91. [https://doi.org/10.1016/0034-4257\(90\)90100-Z](https://doi.org/10.1016/0034-4257(90)90100-Z)
- Ji, B., Chang, C.-I., Jensen, J.L., Jensen, J.O., 2005. Weighted least squares error approaches to abundance-constrained linear spectral mixture analysis, in: *Algorithms and Technologies for Multispectral, Hyperspectral, and Ultraspectral Imagery XI*. SPIE, p. 691. <https://doi.org/10.1117/12.604102>
- Ji, C., Li, X., Wei, H., Li, S., 2020. Comparison of Different Multispectral Sensors for Photosynthetic and Non-Photosynthetic Vegetation-Fraction Retrieval. *Remote Sens.* 12, 115. <https://doi.org/10.3390/rs12010115>
- Jin, Z., Azzari, G., You, C., Di Tommaso, S., Aston, S., Burke, M., Lobell, D.B., 2019. Smallholder maize area and yield mapping at national scales with Google Earth Engine. *Remote Sens. Environ.* 228, 115–128. <https://doi.org/10.1016/j.rse.2019.04.016>
- Jordahl, K., Van den Bossche, J., Fleischmann, M., Wasserman, J., McBride, J., Gerard, J., Tratner, J., Perry, M., Garcia Badaracco, A., Farmer, C., Hjelle, G.A., Snow, A.D., Cochran, M., Gillies, S., Culbertson, L., Bartos, M., Eubank, N., Bilogur, A., Rey, S., Ren, C., Arribas-Bel, D., Wasser, L., Wolf, L.J., Journois, M., Wilson, J., Greenhall, A.,

- Leblanc, F., 2014. GeoPandas: Python tools for geographic data. <https://doi.org/10.5281/zenodo.3946761>.
- Joshi, N., Baumann, M., Ehammer, A., Fensholt, R., Grogan, K., Hostert, P., Jepsen, M.R., Kuemmerle, T., Meyfroidt, P., Mitchard, E.T.A., Reiche, J., Ryan, C.M., Waske, B., 2016. A review of the application of optical and radar remote sensing data fusion to land use mapping and monitoring. *Remote Sens.* 8, 70. <https://doi.org/10.3390/rs8010070>
- Kacic, P., Hirner, A., Da Ponte, E., 2021. Fusing sentinel-1 and-2 to model gedi-derived vegetation structure characteristics in gee for the paraguayan chaco. *Remote Sens.* 13, 5105. <https://doi.org/10.3390/rs13245105>
- Kaczensky, P., Burnik Šturm, M., Sablin, M. V., Voigt, C.C., Smith, S., Ganbaatar, O., Balint, B., Walzer, C., Spasskaya, N.N., 2017. Stable isotopes reveal diet shift from pre-extinction to reintroduced Przewalski's horses. *Sci. Rep.* 7. <https://doi.org/10.1038/s41598-017-05329-6>
- Kaczensky, P., Enkhsaikhan, N., Ganbaatar, O., Walzer, C., 2008. The great gobi b strictly protected area in mongolia - refuge or sink for wolves cards lupus in the Gobi? *Wildlife Biol.* 14, 444–456. <https://doi.org/10.2981/0909-6396-14.4.444>
- Kaczensky, P., Kuehn, R., Lhagvasuren, B., Pietsch, S., Yang, W., Walzer, C., 2011. Connectivity of the Asiatic wild ass population in the Mongolian Gobi. *Biol. Conserv.* 144, 920–929. <https://doi.org/10.1016/j.biocon.2010.12.013>
- Kazantseva, T.I., Slemnev, N.N., Gunin, P.D., Tsooj, S., 2012. Structure and Productivity of Haloxylon ammodendron Communities in the Mongolian Gobi. *Erforsch. Biol. Ressourcen der Mongolei* 12, 405–414.
- Khatant Forest LLC, 2020. Khovd aimag Üyench soum 2020 [in Mongolian].
- Khaulenbek, A., Ihanbai, K., Batkhoo, N., 2018. Saxaul Forest in Mongolia: Ecosystem, resources, values. Ulan Baatar.
- LeCun, Y., Bengio, Y., 1995. Convolutional networks for images, speech, and time-series, in: *The Handbook of Brain Theory and Neural Networks*. MIT Press, Cambridge, MA.
- Lee, C.K.F., Nicholson, E., Duncan, C., Murray, N.J., 2021. Estimating changes and trends in ecosystem extent with dense time-series satellite remote sensing. *Conserv. Biol.* 35, 325–335. <https://doi.org/10.1111/cobi.13520>

- Lee, J. Sen, 1999. Polarimetric SAR speckle filtering and its implication for classification. *IEEE Trans. Geosci. Remote Sens.* 37, 2363–2373. <https://doi.org/10.1109/36.789635>
- Li, M., Zang, S., Zhang, B., Li, S., Wu, C., 2014. A review of remote sensing image classification techniques: The role of Spatio-contextual information. *Eur. J. Remote Sens.* 47, 389–411. <https://doi.org/10.5721/EuJRS20144723>
- Li, P., Wang, Q., 2013. Retrieval of chlorophyll for assimilating branches of a typical desert plant through inversed radiative transfer models. *Int. J. Remote Sens.* 34, 2402–2416. <https://doi.org/10.1080/01431161.2012.744859>
- Lillesand, T.M., Kiefer, R.W., Chipman, J.W., 2015. Remote sensing and image interpretation, Seventh ed. ed. John Wiley & Sons, Ltd, Hoboken, NJ.
- Lippitt, C.L., Stow, D.A., Roberts, D.A., Coulter, L.L., 2018. Multidate MESMA for monitoring vegetation growth forms in southern California shrublands. *Int. J. Remote Sens.* 39, 655–683. <https://doi.org/10.1080/01431161.2017.1388936>
- Loew, A., Mauser, W., 2007. Generation of geometrically and radiometrically terrain corrected SAR image products. *Remote Sens. Environ.* 106, 337–349. <https://doi.org/10.1016/j.rse.2006.09.002>
- Louis, J., Debaecker, V., Pflug, B., Main-Knorn, M., Bieniarz, J., Mueller-Wilm, U., Cadau, E., Gascon, F., 2016. Sentinel-2 SEN2COR: L2A processor for users, in: Ouwehand, L. (Ed.), *Proceedings Living Planet Symposium 2016*. Prague, pp. 1–8.
- Lu, B., Proctor, C., He, Y., 2021. Investigating different versions of PROSPECT and PROSAIL for estimating spectral and biophysical properties of photosynthetic and non-photosynthetic vegetation in mixed grasslands. *GIScience Remote Sens.* 58, 354–371. <https://doi.org/10.1080/15481603.2021.1877435>
- Luor, D.C., 2015. A comparative assessment of data standardization on support vector machine for classification problems. *Intell. Data Anal.* 19, 529–546. <https://doi.org/10.3233/IDA-150730>
- Mandal, D., Kumar, V., Ratha, D., Dey, S., Bhattacharya, A., Lopez-Sanchez, J.M., McNairn, H., Rao, Y.S., 2020. Dual polarimetric radar vegetation index for crop growth monitoring using sentinel-1 SAR data. *Remote Sens. Environ.* 247, 111954. <https://doi.org/10.1016/j.rse.2020.111954>

- Markert, K.N., Markert, A.M., Mayer, T., Nauman, C., Haag, A., Poortinga, A., Bhandari, B., Thwal, N.S., Kunlamai, T., Chishtie, F., Kwant, M., Phongsapan, K., Clinton, N., Towashiraporn, P., Saah, D., 2020. Comparing Sentinel-1 surface water mapping algorithms and radiometric terrain correction processing in southeast Asia utilizing Google Earth Engine. *Remote Sens.* 12, 2469. <https://doi.org/10.3390/RS12152469>
- Mateo-García, G., Gómez-Chova, L., Amorós-López, J., Muñoz-Marí, J., Camps-Valls, G., 2018. Multitemporal cloud masking in the Google Earth Engine. *Remote Sens.* 10, 1079. <https://doi.org/10.3390/rs10071079>
- MathWorks, 2021. MATLAB 2021a. https://ch.mathworks.com/de/products/new_products/release2021a.html.
- Meng, X., Gao, X., Li, Sen, Li, Shengyu, Lei, J., 2021. Monitoring desertification in Mongolia based on Landsat images and Google Earth Engine from 1990 to 2020. *Ecol. Indic.* 129, 1470–160. <https://doi.org/10.1016/j.ecolind.2021.107908>
- Michler, L.M., Kaczensky, P., Ploechl, J.F., Batsukh, D., Baumgartner, S.A., Battogtokh, B., Treydte, A.C., 2022. Moving Toward the Greener Side: Environmental Aspects Guiding Pastoral Mobility and Impacting Vegetation in the Dzungarian Gobi, Mongolia. *Rangel. Ecol. Manag.* 83, 149–160. <https://doi.org/10.1016/J.RAMA.2022.03.006>
- Moran, P.A.P., 1948. The Interpretation of Statistical Maps. *J. R. Stat. Soc. Ser. B* 10, 243–251. <https://doi.org/10.1111/j.2517-6161.1948.tb00012.x>
- Morissette, J.T., Richardson, A.D., Knapp, A.K., Fisher, J.I., Graham, E.A., Abatzoglou, J., Wilson, B.E., Breshears, D.D., Henebry, G.M., Hanes, J.M., Liang, L., 2009. Tracking the rhythm of the seasons in the face of global change: Phenological research in the 21 st century. *Front. Ecol. Environ.* 7, 253–260. <https://doi.org/10.1890/070217>
- Moser, G., Serpico, S.B., Benediktsson, J.A., 2013. Land-cover mapping by markov modeling of spatial-contextual information in very-high-resolution remote sensing images. *Proc. IEEE* 101, 631–651. <https://doi.org/10.1109/JPROC.2012.2211551>
- Müller-Wilm, U., 2017. S2 MPC Sen2Cor Configuration and User Manual Ref. S2-PDGS-MPC-L2A-SUM-V2.4.
- Mullissa, A., Vollrath, A., Odongo-Braun, C., Slagter, B., Balling, J., Gou, Y., Gorelick, N., Reiche, J., 2021. Sentinel-1 SAR Backscatter Analysis Ready Data Preparation in Google

- Earth Engine. Remote Sens. 13, 1954. <https://doi.org/10.3390/rs13101954>
- Munkh Nagoon Joodoo LLC, 2020. Khovd aimag Altai soum 2020 [in Mongolian].
- Nascimento, J.M.P., Dias, J.M.B., 2005. Vertex component analysis: A fast algorithm to unmix hyperspectral data. IEEE Trans. Geosci. Remote Sens. 43, 898–910. <https://doi.org/10.1109/TGRS.2005.844293>
- Nguyen, M.D., Baez-Villanueva, O.M., Bui, D.D., Nguyen, P.T., Ribbe, L., 2020. Harmonization of landsat and sentinel 2 for crop monitoring in drought prone areas: Case studies of Ninh Thuan (Vietnam) and Bekaa (Lebanon). Remote Sens. 12, 281. <https://doi.org/10.3390/rs12020281>
- Nyamsuren, B., Nasahara, K.N., Kubota, T., Masaki, T., 2019. Vegetation mapping by using GPM/DPR over the mongolian land. Remote Sens. 11, 2386. <https://doi.org/10.3390/rs11202386>
- Nyongesah, M.J., Wang, Q., Li, P., 2015. Effectiveness of photochemical reflectance index to trace vertical and seasonal chlorophyll a/b ratio in Haloxylon ammodendron. Acta Physiol. Plant. 37, 1–11. <https://doi.org/10.1007/s11738-014-1747-x>
- Ouaadi, N., Jarlan, L., Ezzahar, J., Zribi, M., Khabba, S., Bouras, E., Bousbih, S., Frison, P.L., 2020. Monitoring of wheat crops using the backscattering coefficient and the interferometric coherence derived from Sentinel-1 in semi-arid areas. Remote Sens. Environ. 251, 112050. <https://doi.org/10.1016/j.rse.2020.112050>
- Pandit, S., Tsuyuki, S., Dube, T., 2020. Exploring the inclusion of Sentinel-2 MSI texture metrics in above-ground biomass estimation in the community forest of Nepal. Geocarto Int. 35, 1832–1849. <https://doi.org/10.1080/10106049.2019.1588390>
- Pedregosa, F., Varoquaux, G., Gramfort, A., Michel, V., Thirion, B., Grisel, O., Blondel, M., Prettenhofer, P., Weiss, R., Dubourg, V., Vanderplas, J., Passos, A., Cournapeau, D., Brucher, M., Perrot, M., Duchesnay, É., 2011. Scikit-learn: Machine learning in Python. J. Mach. Learn. Res. 12, 2825–2830. <https://doi.org/10.48550/arxiv.1201.0490>
- Periasamy, S., 2018. Significance of dual polarimetric synthetic aperture radar in biomass retrieval: An attempt on Sentinel-1. Remote Sens. Environ. 217, 537–549. <https://doi.org/10.1016/j.rse.2018.09.003>
- Pipia, L., Amin, E., Belda, S., Salinero-Delgado, M., Verrelst, J., 2021. Green lai mapping and

- cloud gap-filling using gaussian process regression in google earth engine. *Remote Sens.* 13, 403. <https://doi.org/10.3390/rs13030403>
- Planet Labs Inc., 2018a. Planet Surface Reflectance Version 2.0. San Francisco.
- Planet Labs Inc., 2018b. Skysat Imagery Product Specification. San Francisco.
- Ploton, P., Mortier, F., Réjou-Méchain, M., Barbier, N., Picard, N., Rossi, V., Dormann, C., Cornu, G., Viennois, G., Bayol, N., Lyapustin, A., Gourlet-Fleury, S., Péliissier, R., 2020. Spatial validation reveals poor predictive performance of large-scale ecological mapping models. *Nat. Commun.* 2020 111 11, 1–11. <https://doi.org/10.1038/s41467-020-18321-y>
- Poortinga, A., Tenneson, K., Shapiro, A., Nguyen, Q., Aung, K.S., Chishtie, F., Saah, D., 2019. Mapping plantations in Myanmar by fusing Landsat-8, Sentinel-2 and Sentinel-1 data along with systematic error quantification. *Remote Sens.* 11, 831. <https://doi.org/10.3390/rs11070831>
- Potin, P., Rosich, B., Miranda, N., Grimont, P., Shurmer, I., O'Connell, A., Krassenburg, M., Gratadour, J.B., 2019. Copernicus Sentinel-1 Constellation Mission Operations Status, in: *International Geoscience and Remote Sensing Symposium (IGARSS)*. Institute of Electrical and Electronics Engineers Inc., pp. 5385–5388. <https://doi.org/10.1109/IGARSS.2019.8898949>
- Praticò, S., Solano, F., Di Fazio, S., Modica, G., 2021. Machine learning classification of mediterranean forest habitats in google earth engine based on seasonal sentinel-2 time-series and input image composition optimisation. *Remote Sens.* 13, 1–28. <https://doi.org/10.3390/rs13040586>
- Pullanagari, R.R., Dehghan-Shoar, M., Yule, I.J., Bhatia, N., 2021. Field spectroscopy of canopy nitrogen concentration in temperate grasslands using a convolutional neural network. *Remote Sens. Environ.* <https://doi.org/10.1016/j.rse.2021.112353>
- Pyankov, V.I., Black, C.C., Artyusheva, E.G., Voznesenskaya, E. V, Ku, M.S.B., Edwards, G.E., 1999. Features of photosynthesis in Haloxylon species of Chenopodiaceae that are dominant plants in Central Asian deserts. *Plant Cell Physiol.* 40, 125–134. <https://doi.org/10.1093/oxfordjournals.pcp.a029519>
- QGIS Development Team, 2021. QGIS Geographic Information System. www.qgis.org.
- Quegan, S., Yu, J.J., 2001. Filtering of multichannel SAR images. *IEEE Trans. Geosci. Remote*

- Sens. 39, 2373–2379. <https://doi.org/10.1109/36.964973>
- Raksuntorn, N., Du, Q., 2010. Nonlinear spectral mixture analysis for hyperspectral imagery in an unknown environment. *IEEE Geosci. Remote Sens. Lett.* 7, 836–840. <https://doi.org/10.1109/LGRS.2010.2049334>
- Ramadan, T., 1998. Ecophysiology of salt excretion in the xero-halophyte *Reaumuria hirtella*. *New Phytol.* 139, 273–281. <https://doi.org/10.1046/j.1469-8137.1998.00159.x>
- Randolph, T.W., 2006. Scale-based normalization of spectral data. *Cancer Biomarkers* 2, 135–144. <https://doi.org/10.3233/CBM-2006-23-405>
- Ray, T.W., Murray, B.C., 1996. Nonlinear spectral mixing in desert vegetation. *Remote Sens. Environ.* 55, 59–64. [https://doi.org/10.1016/0034-4257\(95\)00171-9](https://doi.org/10.1016/0034-4257(95)00171-9)
- Richter, R., Schläpfer, D., 2017. Atmospheric / Topographic Correction for Satellite Imagery (ATCOR - 2/3 User Guide). ATCOR-2/3 User Guid. Version 9.1.2 1–71.
- Rüetschi, M., Weber, D., Koch, T.L., Waser, L.T., Small, D., Ginzler, C., 2021. Countrywide mapping of shrub forest using multi-sensor data and bias correction techniques. *Int. J. Appl. Earth Obs. Geoinf.* 105, 102613. <https://doi.org/10.1016/j.jag.2021.102613>
- Sanchez, A.H., Picoli, M.C.A., Camara, G., Andrade, P.R., Chaves, M.E.D., Lechler, S., Soares, A.R., Marujo, R.F.B., Simões, R.E.O., Ferreira, K.R., Queiroz, G.R., 2020. Comparison of cloud cover detection algorithms on sentinel-2 images of the Amazon tropical forest. *Remote Sens.* 12, 1284. <https://doi.org/10.3390/RS12081284>
- Sarzynski, T., Giam, X., Carrasco, L., Huay Lee, J.S., 2020. Combining radar and optical imagery to map oil palm plantations in Sumatra, Indonesia, using the Google Earth Engine. *Remote Sens.* 12. <https://doi.org/10.3390/rs12071220>
- Schaepman-Strub, G., Schaepman, M.E., Painter, T.H., Dangel, S., Martonchik, J. V., 2006. Reflectance quantities in optical remote sensing-definitions and case studies. *Remote Sens. Environ.* 103, 27–42. <https://doi.org/10.1016/j.rse.2006.03.002>
- Schiefer, F., Schmidlein, S., Kattenborn, T., 2021. The retrieval of plant functional traits from canopy spectra through RTM-inversions and statistical models are both critically affected by plant phenology. *Ecol. Indic.* 121, 107062. <https://doi.org/10.1016/j.ecolind.2020.107062>

- Shi, T., Xu, H., 2019. Derivation of Tasseled Cap Transformation Coefficients for Sentinel-2 MSI At-Sensor Reflectance Data. *IEEE J. Sel. Top. Appl. Earth Obs. Remote Sens.* 12, 4038–4048. <https://doi.org/10.1109/JSTARS.2019.2938388>
- Shukherdorj, B., Oyuntsetseg, B., Oyundari, C., Oyundelger, K., Urgamal, M., Darikhand, D., Soninkhishig, N., Nyambayar, D., Khaliunaa, K., Tsegmed, Z., Kechaykin, A.A., Shmakov, A.I., Erst, A.S., Friesen, N., Ritz, C.M., Wesche, K., Choi, H.J., 2021. The vascular plant diversity of dzungarian gobi in western Mongolia, with an annotated checklist. *Phytotaxa* 501, 1–55. <https://doi.org/10.11646/phytotaxa.501.1.1>
- Small, C., 2001. Estimation of urban vegetation abundance by spectral mixture analysis. *Int. J. Remote Sens.* 22, 1305–1334.
- Small, D., 2011. Flattening gamma: Radiometric terrain correction for SAR imagery. *IEEE Trans. Geosci. Remote Sens.* 49, 3081–3093. <https://doi.org/10.1109/TGRS.2011.2120616>
- Somers, B., Asner, G.P., Tits, L., Coppin, P., 2011. Endmember variability in Spectral Mixture Analysis: A review. *Remote Sens. Environ.* 115, 1603–1616. <https://doi.org/10.1016/j.rse.2011.03.003>
- Song, J., Gao, S., Zhu, Y., Ma, C., 2019. A survey of remote sensing image classification based on CNNs. *Big Earth Data* 3, 232–254. <https://doi.org/10.1080/20964471.2019.1657720>
- Soudani, K., Delpierre, N., Berveiller, D., Hmimina, G., Vincent, G., Morfin, A., Dufrêne, É., 2021. Potential of C-band Synthetic Aperture Radar Sentinel-1 time-series for the monitoring of phenological cycles in a deciduous forest. *Int. J. Appl. Earth Obs. Geoinf.* 104, 102505. <https://doi.org/10.1016/j.jag.2021.102505>
- Su, P.-X., An, L.-Z., Ma, R.-J., Liu, X.-M., 2005. Kranz Anatomy and C4 Photosynthetic Characteristics of Two Desert Plants, *Haloxylon ammodendron* and *Calligonum mongolicum*. *Chinese J. Plant Ecol.* 29, 1–7. <https://doi.org/10.17521/cjpe.2005.0001>
- Suvdantsetseg, B., Fukui, H., Tsolmon, R., 2008. Saxaul forest area determination by remote sensing in Mongolia's gobi region. *Int. Arch. Photogramm. Remote Sens. Spat. Inf. Sci.* 1081–1086.
- Tamiminia, H., Salehi, B., Mahdianpari, M., Quackenbush, L., Adeli, S., Brisco, B., 2020. Google Earth Engine for geo-big data applications: A meta-analysis and systematic

review. ISPRS J. Photogramm. Remote Sens. <https://doi.org/10.1016/j.isprsjprs.2020.04.001>

Tang, L., He, M., Li, X., 2020. Verification of fractional vegetation coverage and NDVI of desert vegetation via UAVRS technology. *Remote Sens.* 12, 1742. <https://doi.org/10.3390/rs12111742>

TensorFlow Developers, 2022. TensorFlow. <https://doi.org/10.5281/zenodo.4724125>

Tobler, W.R., 1970. A Computer Movie Simulating Urban Growth in the Detroit Region. *Econ. Geogr.* 46, 234. <https://doi.org/10.2307/143141>

Torres, R., Snoeij, P., Geudtner, D., Bibby, D., Davidson, M., Attema, E., Potin, P., Rommen, B.Ö., Floury, N., Brown, M., Traver, I.N., Deghaye, P., Duesmann, B., Rosich, B., Miranda, N., Bruno, C., L'Abbate, M., Croci, R., Pietropaolo, A., Huchler, M., Rostan, F., 2012. GMES Sentinel-1 mission. *Remote Sens. Environ.* 120, 9–24. <https://doi.org/10.1016/j.rse.2011.05.028>

Townshend, J.R.G., Gurney, C., McManus, J., Justice, C.O., 1992. The Impact of Misregistration on Change Detection. *IEEE Trans. Geosci. Remote Sens.* 30, 1054–1060. <https://doi.org/10.1109/36.175340>

Truckenbrodt, J., Freemantle, T., Williams, C., Jones, T., Small, D., Dubois, C., Thiel, C., Rossi, C., Syriou, A., Giuliani, G., 2019. Towards sentinel-1 SAR analysis-ready data: A best practices assessment on preparing backscatter data for the cube. *Data* 4, 93. <https://doi.org/10.3390/data4030093>

Ullmann, T., Sauerbrey, J., Hoffmeister, D., May, S.M., Baumhauer, R., Bubenzer, O., 2019. Assessing spatiotemporal variations of sentinel-1 InSAR coherence at different time scales over the atacama desert (Chile) between 2015 and 2018. *Remote Sens.* 11, 2960. <https://doi.org/10.3390/rs11242960>

Verde, N., Kokkoris, I.P., Georgiadis, C., Kaimaris, D., Dimopoulos, P., Mitsopoulos, I., Mallinis, G., 2020. National scale land cover classification for ecosystem services mapping and assessment, using multitemporal copernicus EO data and google earth engine. *Remote Sens.* 12, 1–24. <https://doi.org/10.3390/rs12203303>

Verhelst, K., Gou, Y., Herold, M., Reiche, J., 2021. Improving forest baseline maps in tropical wetlands using gedi-based forest height information and sentinel-1. *Forests* 12, 1374.

<https://doi.org/10.3390/f12101374>

- Verrelst, J., Alonso, L., Rivera Caicedo, J.P., Moreno, J., Camps-Valls, G., 2013. Gaussian process retrieval of chlorophyll content from imaging spectroscopy data. *IEEE J. Sel. Top. Appl. Earth Obs. Remote Sens.* 6, 867–874. <https://doi.org/10.1109/JSTARS.2012.2222356>
- Verrelst, J., Rivera Caicedo, J.P., Muñoz-Marí, J., Camps-Valls, G., Moreno, J., 2017. SCOPE-based emulators for fast generation of synthetic canopy reflectance and sun-induced fluorescence Spectra. *Remote Sens.* 9, 927. <https://doi.org/10.3390/rs9090927>
- Verrelst, J., Rivera, J.P., Veroustraete, F., Muñoz-Marí, J., Clevers, J.G.P.W., Camps-Valls, G., Moreno, J., 2015. Experimental Sentinel-2 LAI estimation using parametric, non-parametric and physical retrieval methods - A comparison. *ISPRS J. Photogramm. Remote Sens.* 108, 260–272. <https://doi.org/10.1016/j.isprsjprs.2015.04.013>
- Verrelst, J., Romijn, E., Kooistra, L., 2012. Mapping vegetation density in a heterogeneous river floodplain ecosystem using pointable CHRIS/PROBA data. *Remote Sens.* 4, 2866–2889. <https://doi.org/10.3390/rs4092866>
- Verrelst, J., Sabater, N., Rivera, J.P., Muñoz-Marí, J., Vicent, J., Camps-Valls, G., Moreno, J., 2016. Emulation of Leaf, Canopy and Atmosphere Radiative Transfer Models for Fast Global Sensitivity Analysis. *Remote Sens.* 2016, Vol. 8, Page 673 8, 673. <https://doi.org/10.3390/RS8080673>
- Verrelst, J., Schaepman, M.E., Koetz, B., Kneubühler, M., 2008. Angular sensitivity analysis of vegetation indices derived from CHRIS/PROBA data. *Remote Sens. Environ.* 112, 2341–2353. <https://doi.org/10.1016/j.rse.2007.11.001>
- Verrelst, J., Vicent, J., Rivera-Caicedo, J.P., Lumbierres, M., Morcillo-Pallarés, P., Moreno, J., 2019. Global sensitivity analysis of leaf-canopy-atmosphere RTMs: Implications for biophysical variables retrieval from top-of-atmosphere radiance data. *Remote Sens.* 11, 1923. <https://doi.org/10.3390/rs11161923>
- Vollrath, A., Mullissa, A., Reiche, J., 2020. Angular-based radiometric slope correction for Sentinel-1 on google earth engine. *Remote Sens.* 12, 1867. <https://doi.org/10.3390/rs12111867>
- von Wehrden, H., Gungalag, R., 2003. Final Report for the „Creation of a vegetation Map of

- the Great Gobi National park „B“. Marburg; Ulaan Bataar.
- von Wehrden, H., Wesche, K., Miede, G., 2009. Plant communities of the southern Mongolian Gobi. *Phytocoenologia* 39, 331–376. <https://doi.org/10.1127/0340-269X/2009/0039-0331>
- von Wehrden, H., Wesche, K., Tungalag, R., 2006. Plant communities of the Great Gobi B Strictly Protected Area, Mongolia. *Mong. J. Biol. Sci.* 4, 3–17.
- Vreugdenhil, M., Wagner, W., Bauer-Marschallinger, B., Pfeil, I., Teubner, I., Rüdiger, C., Strauss, P., 2018. Sensitivity of Sentinel-1 backscatter to vegetation dynamics: An Austrian case study. *Remote Sens.* 10, 1396. <https://doi.org/10.3390/rs10091396>
- Wagner, W., Bauer-Marschallinger, B., Navacchi, C., Reuß, F., Cao, S., Reimer, C., Schramm, M., Briese, C., 2021. A sentinel-1 backscatter datacube for global land monitoring applications. *Remote Sens.* 13, 4622. <https://doi.org/10.3390/rs13224622>
- Wang, H., Harrison, S., Prentice, I.C., Yang, Y., Bai, F., Furstenau Togashi, H., Wang, M., Zhou, S., Ni, J., 2017. The China Plant Trait Database. <https://doi.org/https://doi.org/10.1594/PANGAEA.871819>
- Waser, L.T., Rüetschi, M., Psomas, A., Small, D., Rehush, N., 2021. Mapping dominant leaf type based on combined Sentinel-1/-2 data – Challenges for mountainous countries. *ISPRS J. Photogramm. Remote Sens.* 180, 209–226. <https://doi.org/10.1016/j.isprsjprs.2021.08.017>
- Waskom, M., 2021. seaborn: statistical data visualization. *J. Open Source Softw.* 6, 3021. <https://doi.org/10.21105/joss.03021>
- Weber, D., Rüetschi, M., Small, D., Ginzler, C., 2020. Large-scale classification of shrub forest with remote sensing data. *Schweizerische Zeitschrift für Forstwes.* 171, 51–59. <https://doi.org/10.3188/szf.2020.0051>
- Winter, M.E., 2004. A proof of the N-FINDR algorithm for the automated detection of endmembers in a hyperspectral image, in: *Algorithms and Technologies for Multispectral, Hyperspectral, and Ultraspectral Imagery X*. p. 31. <https://doi.org/10.1117/12.542854>
- Wu, X., Zheng, X.J., Li, Y., Xu, G.Q., 2019. Varying responses of two *Haloxylon* species to extreme drought and groundwater depth. *Environ. Exp. Bot.* 158, 63–72. <https://doi.org/10.1016/J.ENVEXPBOT.2018.11.014>

- Xu, H., Li, Y., 2006. Water-use strategy of three central Asian desert shrubs and their responses to rain pulse events. *Plant Soil* 285, 5–17. <https://doi.org/10.1007/s11104-005-5108-9>
- Xue, J., Su, B., 2017. Significant remote sensing vegetation indices: A review of developments and applications. *J. Sensors*. <https://doi.org/10.1155/2017/1353691>
- Yommy, A.S., Liu, R., Wu, A.S., 2015. SAR image despeckling using refined lee filter, in: *Proceedings - 2015 7th International Conference on Intelligent Human-Machine Systems and Cybernetics, IHMSC 2015*. Institute of Electrical and Electronics Engineers Inc., pp. 260–265. <https://doi.org/10.1109/IHMSC.2015.236>
- You, N., Dong, J., 2020. Examining earliest identifiable timing of crops using all available Sentinel 1/2 imagery and Google Earth Engine. *ISPRS J. Photogramm. Remote Sens.* 161, 109–123. <https://doi.org/10.1016/j.isprsjprs.2020.01.001>
- Yuan, Q., Shen, H., Li, T., Li, Z., Li, S., Jiang, Y., Xu, H., Tan, W., Yang, Q., Wang, J., Gao, J., Zhang, L., 2020. Deep learning in environmental remote sensing: Achievements and challenges. *Remote Sens. Environ.* 241, 111716. <https://doi.org/10.1016/j.rse.2020.111716>
- Zafari, A., Zurita-Milla, R., Izquierdo-Verdiguier, E., 2019. Evaluating the performance of a Random Forest Kernel for land cover classification. *Remote Sens.* 11, 575. <https://doi.org/10.3390/rs11050575>
- Zaluu Tugul LLC, 2020. *Khovd aimag Bulgan soum 2020* [in Mongolian].
- Zanaga, D., Van De Kerchove, R., De Keersmaecker, W., Souverijns, N., Brockmann, C., Quast, R., Wevers, J., Grosu, A., Paccini, A., Vergnaud, S., Cartus, O., Santoro, M., Fritz, S., Georgieva, I., Lesiv, M., Carter, S., Herold, M., Li, L., Tsendbazar, N.-E., Ramoino, F., Arino, O., 2021. *ESA WorldCover 10 m 2020 v100*. <https://doi.org/10.5281/ZENODO.5571936>
- Zheng, C., Wang, Q., 2014. Water-use response to climate factors at whole tree and branch scale for a dominant desert species in central Asia: *Haloxylon ammodendron*. *Ecohydrology* 7, 56–63. <https://doi.org/10.1002/eco.1321>
- Zheng, H., Du, P., Chen, J., Xia, J., Li, E., Xu, Z., Li, X., Yokoya, N., 2017. Performance evaluation of downscaling sentinel-2 imagery for Land Use and Land Cover classification by spectral-spatial features. *Remote Sens.* 9, 1274. <https://doi.org/10.3390/rs9121274>

Zou, T., Li, Y., Xu, H., Xu, G.Q., 2010. Responses to precipitation treatment for *Haloxylon ammodendron* growing on contrasting textured soils. *Ecol. Res.* 25, 185–194.
<https://doi.org/10.1007/s11284-009-0642-1>

Zupanc, A., 2017. Improving Cloud Detection with Machine Learning [WWW Document].
URL <https://medium.com/sentinel-hub/improving-cloud-detection-with-machine-learning-c09dc5d7cf13> (accessed 9.28.21).

Personal declaration

I hereby declare that the submitted thesis is the result of my own, independent work. All external sources are explicitly acknowledged in the thesis.

Date

24.06.2022

Signature

A handwritten signature in black ink, consisting of a stylized 'J' followed by 'S' and a period.

Jan Schweizer
